

Data analysis techniques useful for the detection of B-mode polarisation of the Cosmic Microwave Background.

A THESIS SUBMITTED TO THE UNIVERSITY OF MANCHESTER
FOR THE DEGREE OF DOCTOR OF PHILOSOPHY
IN THE FACULTY OF ENGINEERING AND PHYSICAL SCIENCES

2015

By
Christopher Wallis
School of Physics and Astronomy

Contents

Abstract	12
Declaration	13
Copyright	14
Acknowledgements	15
The Author	17
Supporting Publications	19
1 Introduction	21
1.1 Λ CDM	21
1.2 Inflationary Cosmology	23
1.2.1 Simple scalar field theory of inflation	24
1.2.2 Primordial perturbations	26
1.3 Using the CMB as a test for inflation	27
1.3.1 Temperature fluctuations	28
1.3.2 Polarization of the CMB	30
1.3.3 Current CMB polarisation measurements	36
1.4 Systematic effects in CMB polarisation experiments	39
1.4.1 Theoretical predictions of error on the recovered B -mode power spectrum	40

CONTENTS

1.4.2	Current techniques to remove systematic effects	42
1.4.3	Work in this thesis	44
2	Waveguides	45
2.1	Allowed modes in a cylindrical waveguide	45
2.2	Calculating beams	47
2.2.1	Finding the far-field radiation pattern	49
2.2.2	Calculating a beam given a mode	53
2.3	Calculating the electric field at the aperture of a horn	55
2.3.1	Frequency dependence of a mode	55
2.3.2	Excitation of modes	56
2.4	Application to multi-moded horns	56
2.4.1	Combining the effect of two modes to the beam	57
2.4.2	Normalising the different modes contributions	58
2.4.3	LSPE and multi-moded horns	60
3	Removing beam asymmetry bias in CMB experiments	61
3.1	Introduction	62
3.2	Basic definitions and preliminaries	63
3.3	Beam asymmetry correction within the pseudo- C_ℓ framework	67
3.3.1	Definition of the pseudo- C_ℓ spectra	67
3.3.2	Calculating the coupling operator	68
3.3.3	Recovering the true CMB spectra	70
3.3.4	Including noise	71
3.4	Impact of beam asymmetries on CMB polarization experiments	72
3.5	Beam asymmetry correction during map-making	74
3.5.1	Extracting the temperature and polarisation of a pixel	75
3.5.2	Removing the leakage from temperature to polarisation	77
3.6	Evaluating the parameter k_{\max} for a temperature only experiment	78
3.6.1	Beam decompositions for some representative cases	79

3.6.2	Using the noise power to set k_{\max} in a temperature only experiment	80
3.7	Testing the pseudo- C_ℓ on Simulations	82
3.7.1	Balloon-like test	84
3.7.2	Satellite-like experiment	87
3.8	Testing the map-making algorithm on Simulations	90
3.8.1	Removing the asymmetry bias on the temperature power spectrum	90
3.8.2	Removing the asymmetry bias on the temperature and polarisation maps	92
3.9	Discussion	94
4	A new map-making algorithm for CMB polarisation experiments	99
4.1	Introduction	100
4.2	Map-making algorithms	101
4.2.1	Map-making algorithm with extensive ψ_t coverage	105
4.2.2	Map-making algorithm with limited ψ_t coverage	106
4.3	Test on Simulations	109
4.3.1	Extensive ψ_t coverage algorithm with a satellite-like experiment	111
4.3.2	Limited ψ_t coverage algorithm with a balloon-like experiment	117
4.4	Identifying Systematic Effects	120
4.5	Discussion	124
5	Optimal scan strategies for the next generation of CMB polarisation satellite experiments	127
5.1	Introduction	128
5.2	Impact of systematics on the B -mode power spectrum	130
5.2.1	Leakage in the differenced timestream	131
5.2.2	Temperature leakage to the polarisation map	134
5.2.3	Temperature leakage to the B -mode power spectrum	136

CONTENTS

5.3	Temperature leakage Simulations	139
5.4	Scan Strategy Parameter Space	143
5.4.1	Scan strategy parameters	143
5.4.2	Practical constraints on scan strategies	147
5.4.3	Error on the B -mode polarisation power spectrum	150
5.5	Discussion and Conclusions	154
6	Conclusions and Future Work	159
6.1	Pseudo- C_ℓ estimator	160
6.2	Map-making algorithms	160
6.3	Scan strategy investigation	162
A	Pseudo-C_ℓ estimator	165
A.1	Relationship between our pseudo- C_ℓ and the standard pseudo- C_ℓ	165
A.2	Product of two coupling kernels	167
A.3	Symmetries in $M_{k_1 k_1' k_2 k_3}^{\ell_1 \ell_2}$	169
A.4	Explicit form of the coupling operator	171
A.5	Relations between $C_\ell^{ss'}$ and C_ℓ^{XY}	171
B	Pseudo-C_ℓ approach to calculating the temperature leakage	173
B.1	Error on the B -mode polarisation power spectrum	173
B.2	Product of two coupling kernels	177
	References	179

List of Tables

5.1	Description of the variables used in the scan strategy analysis (see Sections 5.2 & 5.3 in the main text) and the values adopted for the simulations.	139
5.2	Observational parameters used to generate the scan strategies for the simulations described in Section 5.3. See Figure 5.5 for a diagram describing the parameters.	140

LIST OF TABLES

List of Figures

1.1	Measurements of the CMB temperature power spectrum by the <i>Planck</i> experiment.	30
1.2	Q and U Stokes parameters used to represent polarisation.	31
1.3	Diagram representing how the CMB becomes polarised	32
1.4	Diagram to visualise the polarisation generated from scalar perturbations	33
1.5	Diagram to visualise the polarisation generated from tensor perturbations	34
1.6	CMB temperature and polarisation power spectra due to scalar and tensor perturbations	35
1.7	Current measurements of the TE and EE cross and power spectra by <i>Planck</i>	37
1.8	Current measurements of the low ℓ B -mode power spectrum by <i>Planck</i> and BICEP2	38
1.9	Current measurements of the B -mode power spectrum	40
1.10	An illustration of the dipole, quadrupole and monopole effects; Q parameter only is depicted.	42
2.1	First few Bessel functions	48
2.2	Diagram to define a loop from which the boundary conditions of a perfect conductor can be derived from.	50
2.3	Schematic of the equivalence principle	50
2.4	Defining variables used to show the far-field radiation pattern	51
2.5	The electric field and beam patterns of the first few waveguide modes .	54

LIST OF FIGURES

2.6	The beam patterns of a number of multi-moded horns	59
3.1	Multimoded horn planned to be on board the balloon borne experiment LSPE	78
3.2	The spherical harmonic decomposition of an elliptical Gaussian beam	81
3.3	An example temperature map, the hit map, p_2 quality and weighting function for the balloon-like test of the pseudo- C_ℓ estimator	85
3.4	The recovered temperature power spectrum using my pseudo- C_ℓ esti- mator on the balloon-like experiment	86
3.5	The hit map, p_2 quality and weighting function for the satellite-like test of the pseudo- C_ℓ estimator	88
3.6	The recovered temperature power spectrum using my pseudo- C_ℓ esti- mator on the satellite-like experiment	89
3.7	The recovered temperature power spectrum using my first map-making algorithm on the satellite-like experiment	91
3.8	The recovered temperature map using my first map-making algorithm on the satellite-like experiment	93
3.9	The recovered polarisation power spectrum using my first map-making algorithm on the satellite-like experiment	94
4.1	Demonstration of using Legendre polynomials to reconstruct a system- atic effect	108
4.2	Hit maps and angle coverage of the EPIC and LSPE scan strategies . .	110
4.3	Recovered B -mode power spectrum when the new map making algo- rithm is applied and a simple binned map is made for satellite simula- tion 1 and 2	114
4.4	Recovered B -mode power spectrum when the new map making algo- rithm is applied and a simple binned map is made for satellite simula- tion 3 and 4	115

4.5 Recovered B -mode power spectrum when the new map making algorithm is applied and a simple binned map is made for the balloon simulation 119

4.6 Recovered systematic error maps from satellite simulation 3 122

4.7 Systematic error map cross-correlation with the temperature map . . . 123

5.1 Schematic diagram to define the parameters used to define the differential pointing of a detector pair. 133

5.2 Hit maps and h -values for the EPIC, WMAP and *Planck* scan strategies 141

5.3 The recovered B -mode power spectrum from simulations including differential gain and pointing when using the *Planck*, WMAP and EPIC scan strategies 143

5.4 The recovered B -mode power spectrum from simulations including differential ellipticity when using the *Planck*, WMAP and EPIC scan strategies 144

5.5 Schematic diagram to define the parameters used to define the scan strategies. 145

5.6 Fuel and data rate requirements for the scan strategies investigated . . 148

5.7 $\langle |\tilde{h}_n|^2 \rangle$ values for the scan strategies considered 152

5.8 The fractional error on the recovered B -mode polarisation power spectrum, averaged over the range two ℓ ranges, as a function of the scan strategy parameters. 154

B.1 The simulated temperature to B -mode leakage and predictions using both the approximate form and the pseudo- C_ℓ form. 177

The University of Manchester

ABSTRACT OF THESIS submitted by Christopher Wallis

for the Degree of Doctor of Philosophy and entitled

“Data analysis techniques useful for the detection of B-mode polarisation of the Cosmic Microwave Background.”, September 2015.

Asymmetric beams can create significant bias in estimates of the power spectra from cosmic microwave background (CMB) experiments. With the temperature power spectrum many orders of magnitude stronger than the B-mode power spectrum any systematic error that couples the two must be carefully controlled and/or removed.

In this thesis, I derive unbiased estimators for the CMB temperature and polarisation power spectra taking into account general beams and scan strategies. I test my correction algorithm on simulations of two temperature-only experiments and demonstrate that it is unbiased. I also develop a map-making algorithm that removes beam asymmetry bias at the map level. I demonstrate its implementation using simulations.

I present two new map-making algorithms that create polarisation maps clean of temperature-to-polarisation leakage systematics due to differential gain and pointing between a detector pair. Where a half wave plate is used, I show that the spin-2 systematic due to differential ellipticity can also be removed using my algorithms. The first algorithm is designed to work with scan strategies that have a good range of crossing angles for each map pixel and the second for scan strategies that have a limited range of crossing angles. I demonstrate both algorithms by using simulations of time ordered data with realistic scan strategies and instrumental noise.

I investigate the role that a scan strategy can have in mitigating certain common systematics by averaging systematic errors down with many crossing angles. I present approximate analytic forms for the error on the recovered B-mode power spectrum that would result from these systematic errors. I use these analytic predictions to search the parameter space of common satellite scan strategies to identify the features of a scan strategy that have most impact in mitigating systematic effects.

Declaration

No portion of the work referred to in this thesis has been submitted in support of an application for another degree or qualification of this or any other university or other institution of learning.

Copyright

The author of this thesis (including any appendices and/or schedules to this thesis) owns certain copyright or related rights in it (the “Copyright”) and he has given The University of Manchester certain rights to use such Copyright, including for administrative purposes. Copies of this thesis, either in full or in extracts and whether in hard or electronic copy, may be made only in accordance with the Copyright, Designs and Patents Act 1988 (as amended) and regulations issued under it or, where appropriate, in accordance with licensing agreements which the University has from time to time. This page must form part of any such copies made. The ownership of certain Copyright, patents, designs, trade marks and other intellectual property (the “Intellectual Property”) and any reproductions of copyright works in the thesis, for example graphs and tables (“Reproductions”), which may be described in this thesis, may not be owned by the author and may be owned by third parties. Such Intellectual Property and Reproductions cannot and must not be made available for use without the prior written permission of the owner(s) of the relevant Intellectual Property and/or Reproductions. Further information on the conditions under which disclosure, publication and commercialisation of this thesis, the Copyright and any Intellectual Property and/or Reproductions described in it may take place is available in the University IP Policy (see <http://www.campus.manchester.ac.uk/medialibrary/policies/intellectual-property.pdf>), in any relevant Thesis restriction declarations deposited in the University Library, The University Library’s regulations (see <http://www.manchester.ac.uk/library/aboutus/regulations>) and in The University’s policy on presentation of Theses.

Acknowledgements

First and for most I would like to thank my supervisors Michael Brown and Richard Battye. They have given me exceptional guidance and support in my education as a graduate student.

I would also like to thank other all the members of JBCA which I have worked with, and have helped me over the years. However, special mention must go to those who I have worked with directly; Clive Dickinson, Patrick Leahy, Anna Bonaldi, Rafal Szebietowski and Stefano Camera. My work would have been impossible if not for the assistance from Anthony Holloway and Robert Dickson.

The social side of JBCA has been a pleasure to be part of. Trips to the pub and alike have made my time in Manchester some of the best years of my life. Special mention should be made to; Ian, Jonny, Jack, Niall, Joe, Melis, David and Steph and of course my house mates through out the years; Indy, Sam, Simon, Ed, Sara and Sophie.

This PhD is the culmination of decades of education. I would like to thank Neil Hampton and Marco Pereira from Rugby School whose support and education was part of the reason I chose study for a Physics degree. I then went on to study at Lincoln College, Oxford where I had many inspiring lectures and tutors, in particular Nick Jelley. His interest in physics and friendly attitude allowed me to fully develop a love for physics.

My family, and in particular my parents Barbara and Peter, have supported me and encouraged me throughout my education. They have been invaluable in all aspects of my life.

Finally, I have had an immeasurable amount of help and love from Josephine. She

has proof read my work, calmed me down in times of need and generally been a great support and for that I am truly thankful.

The Author

The author was born in October 1989. He graduated from the University of Oxford in 2012 with a Undergraduate Masters in Physics. After which he started his PhD at Jodrell Bank Centre for Astrophysics in Manchester. Following this he will start a post doctorate position at the Mullard Space Science Laboratory, University College London.

*Einstein developed a theory about space
and it was about time too.*

Supporting Publications

Removing beam asymmetry bias in precision CMB temperature and polarisation experiments

Christopher G. R. Wallis, Michael L. Brown, Richard A. Battye, Giampaolo Pisano and Luca Lamagna, 2014, MNRAS, 442, 1963 (Chapter 3)

A new map-making algorithm for CMB polarisation experiments

Christopher G. R. Wallis, A. Bonaldi, Michael L. Brown, Richard A. Battye, 2014, MNRAS, 453, 2058 (Chapter 4)

Chapter 1

Introduction

Modern day cosmology requires a theoretical model of inflation to reconcile major fundamental flaws in the current theory of a hot Big Bang. Therefore experimental cosmologists all over the globe are attempting to provide valuable constraints on the wealth of inflationary models. This work is a step in that direction. I present techniques for making accurate measurements of the Cosmic Microwave Background (CMB) and I analyse the potential of a future experiments ability to make those measurements. In the introduction I will explain the requirement for inflation and guide the reader through a simple model of inflation. I will then explain how, with observations of the CMB, cosmologists hope to constrain inflation theories. However, first we must understand the very odd position cosmologists have found themselves in, where the universe is described by Λ Cold Dark Matter (Λ CDM).

1.1 Λ CDM

The cosmological principle states that on large scales the universe is homogeneous and statistically isotropic. If we assume general relativity is a sufficient description of gravity in our Universe, the cosmological principle allows us to solve the Einstein field

1: INTRODUCTION

equations and describe the universe with a Friedmann-Robertson-Walker metric,

$$ds^2 = c^2 dt^2 - a(t)^2 \left(\frac{dr^2}{1 - kr^2} + r^2(d\theta^2 + \sin^2 \theta d\phi^2) \right), \quad (1.1)$$

where a is a time dependant scale factor, ds is an infinitesimal interval, t is the time coordinate, r, θ and ϕ are the position coordinates in spherical coordinates. k describes the curvature of the universe, $k = 0$ corresponds to a flat Universe; $k > 0$ corresponds to a closed universe where the universe will ultimately collapse to a singularity and $k < 0$ corresponds to an open universe.

Under the constraints of the cosmological principle the equations of general relativity simplify to the Friedmann and Raychauduri equations,

$$H^2 = \frac{\rho}{3M_{\text{pl}}^2} - \frac{k}{a^2} \quad (1.2)$$

$$\frac{\ddot{a}}{a} = -\frac{\rho + 3p}{6M_{\text{pl}}^2}, \quad (1.3)$$

where $H = \dot{a}/a$, over dots represent derivatives with respect to time of the variable and we have set $c = 1$. M_{pl} is the Planck mass. The energy density and the pressure of the universe are denoted by ρ and p respectively. The conservation of energy-momentum in an isotropic and homogeneous universe gives us,

$$\dot{\rho} + 3H(\rho + p) = 0. \quad (1.4)$$

It turns out that these three equations are not independent: you can derive one from the other two. Therefore, we have two equations and three unknowns. To be able to solve these equations we must understand the properties of the contents of the universe, specifically how the pressure varies as a function of the density. We define the equation of state for each component of the universe,

$$p = w\rho, \quad (1.5)$$

where w is a parameter that is different for each component of the universe. Now we can start to understand the very simple but strange universe that we live in. We have 4 components to the universe. Firstly, baryonic matter when the temperature is low has $w = 0$, radiation has $w = 1/3$, then two dark components of the universe. Dark matter is used to explain a contribution to the mass of the universe that does not appear to interact using any force, other than gravity, therefore, $w = 0$. Then a dark energy component where $w = -1$.

Dark energy is used to explain late time expansion of the universe and it is sufficient to consider it as a vacuum energy density. By having a negative equation of state (w) the pressure it exerts is negative. By looking at equation (1.2) we can see that this would lead to a constant expansion rate. This model is effective to explain the observations, however, the result is not based on a solid theoretical base. There is a wide range of experimental and theoretical work that is ongoing to try to find a satisfactory explanation for the acceleration of the universe.

The early universe must also contain perturbations on this constant background density we have considered thus far. Regions of space must have been overdense relative to the average. These overdense regions collapsed due to gravity creating the structure that we see today. The source of these overdense regions comes from fluctuations in the inflaton during inflation, the topic we turn to next.

1.2 Inflationary Cosmology

Inflation theory is invoked to solve three major problems with a simple view of the Big Bang theory (Baumann et al. 2009).

1. Grand Unified theories predict that in the hot temperatures of the Big Bang, some objects will have been created that we do not see today. These include magnetic monopoles and other topological defects.
2. We measure the universe to be flat. Therefore the current density of the universe

1: INTRODUCTION

exactly balances the expansion rate, see equation (1.2). This suggests very fine tuning of the density of the universe.

3. Without inflation, the horizon¹ at the time of last scattering, subtends $\sim 1^\circ$. This suggests there should be no correlation in the CMB, on scales larger than $\sim 1^\circ$. However, the CMB is found to be the same temperature all over the sky, to 1 part in 10^4 . The isotropy of the CMB is the greatest evidence for the cosmological principle discussed in Section 1.1.

Inflation solves these problems with a rapid expansion of the universe by a factor of $\sim 10^{26}$ in less than $\sim 10^{-34}$ s (Baumann et al. 2009). The first two problems are solved intuitively by this. The monopoles and other defects are separated by such large distances that they are no longer observable and any curvature in the universe has been flattened as a result of the expansion.

The horizon problem is solved by considering a small region of the universe before inflation. If this region is small enough it will be causally linked and thermally smoothed as a result. This small region is then expanded to at least the horizon scale today by inflation. This requires an exponential increase in the scale parameter a . This is the basis of many different inflation theories.

1.2.1 Simple scalar field theory of inflation

We consider the simplest theory of inflation to demonstrate the concepts as they do in Liddle (1999). Consider a scalar field with the Lagrangian,

$$\mathcal{L}_{\text{eff}}(\phi) = \frac{1}{2} \partial_\mu \phi \partial^\mu \phi - V(\phi). \quad (1.6)$$

We apply the cosmological principle to the beginning and end of inflation. Therefore, we can use the Friedmann-Robertson-Walker (FRW) metric to describe the universe,

¹The distance over which the universe is causally linked.

see equation (1.1). The equations of motion, as before, are the Friedman and Raychaudhuri equations, see equations (1.2) and (1.3), where the energy density and pressure are governed by the inflaton. The third equation of motion is found by considering the Lagrangian in equation (1.6). The equations of motion are therefore,

$$H^2 \equiv \left(\frac{\dot{a}}{a}\right)^2 = \frac{1}{3M_{\text{pl}}^2} \left(\frac{1}{2}\dot{\phi}^2 + V(\phi)\right), \quad (1.7)$$

$$\frac{\ddot{a}}{a} = -\frac{1}{3M_{\text{pl}}^2} \left(\frac{1}{2}\dot{\phi}^2 - V(\phi)\right), \quad (1.8)$$

$$\ddot{\phi} + 3H\dot{\phi} + V'(\phi) = 0, \quad (1.9)$$

where $V' \equiv \partial V/\partial\phi$, and we have ignored the curvature term. To ensure the scalar field creates the desired exponential expansion we say that $\dot{\phi}^2 \ll V(\phi)$, and that the potential varies only a small amount. From equation (1.7) we have that $a(t) = a(0)e^{Ht}$, where $H \approx \text{constant}$. This is the required condition on inflation to solve the problems outlined at the beginning of the section. To ensure that the condition $\dot{\phi}^2 \ll V(\phi)$ holds for the period of inflation the so called slow-roll parameters must be small. The slow-roll parameters are defined to be (Liddle 1999),

$$\epsilon \equiv -\frac{\dot{H}}{H^2} \approx \frac{M_{\text{pl}}^2}{2} \left(\frac{V'}{V}\right)^2 \quad (1.10)$$

$$|\eta| \approx M_{\text{pl}}^2 \left|\frac{V''}{V}\right|. \quad (1.11)$$

Inflation is said to come to an end when $\epsilon \rightarrow 1$. After inflation the scalar field must decay into the matter we see today (Liddle 1999). This process is known as reheating, the exact nature of reheating is not very well understood. It involves physics out of reach of current particle accelerators, as does inflation.

1.2.2 Primordial perturbations

I have described a theory which can solve the problems outlined at the beginning of this section. We now look at the structure in the universe. The required property of the inflation theory, was to expand the universe by at least 26 orders of magnitude (Baumann et al. 2009), in order to explain the exceptionally homogeneous CMB temperature.

As with any field the scalar field in our inflation theory will be perturbed due to quantum fluctuations (Baumann et al. 2009). These fluctuations will show themselves as perturbations to the FRW metric $g_{\mu\nu}$ (Baumann et al. 2009). We write

$$g_{ij} = a^2[\delta_{ij}(1 + \zeta) + h_{ij}], \quad (1.12)$$

where $||h_{ij}||, \zeta \ll 1$ and $\partial_j h_{ij} = h_i^i = 0$. In the rapid expansion the spatial dimension of a perturbation can become larger than the horizon scale. When this happens the fluctuations are frozen into the metric. After inflation we are left with Gaussian randomly distributed perturbations. The scalar perturbations represent primordial density fluctuations and the tensor perturbations are gravitational waves.

We take the Fourier transform of the perturbations, written as $\zeta_{\mathbf{k}}$ and $h_{\mathbf{k}}$, and define their power spectra,

$$\langle \zeta_{\mathbf{k}} \zeta_{\mathbf{k}'} \rangle = (2\pi)^3 \delta(\mathbf{k} + \mathbf{k}') \frac{2\pi^2}{k^3} P_s(k), \quad (1.13)$$

$$\langle h_{\mathbf{k}} h_{\mathbf{k}'} \rangle = (2\pi)^3 \delta(\mathbf{k} + \mathbf{k}') \frac{2\pi^2}{k^3} P_t(k). \quad (1.14)$$

As the expansion causes the perturbations to “freeze out” and the potential $V(\phi)$ drives the expansion, see equation (1.7), the power spectra of the perturbations are set by $V(\phi)$. As we are in the slow-roll regime these power spectra will therefore, be close to flat (Baumann et al. 2009). We define,

$$P_s(k) = A_s \left(\frac{k}{k_*} \right)^{n_s - 1}, \quad (1.15)$$

$$P_t(k) = A_t \left(\frac{k}{k_*} \right)^{n_t}, \quad (1.16)$$

where $n_s - 1$ and n_t are close to zero. Characterising n_s is vital to distinguish between inflation theories as it tells us about $V(\phi)$. The other important quantity, to determine from experiment, is the tensor to scalar ratio,

$$r_{k_*} \equiv \frac{P_t(k)}{P_s(k)} \Big|_{k=k_*}. \quad (1.17)$$

$$(1.18)$$

It can be shown that $n_s - 1 \approx 2\eta - 6\epsilon$ and that $r = 16\epsilon$ (Liddle et al. 1994), therefore by constraining the amplitudes and shapes of the primordial power spectra we are constraining the inflation models.

1.3 Using the CMB as a test for inflation

Determining the value of the scalar to tensor ratio r and the slope of the scalar power spectrum $n_s - 1$ is the focus of much research. The main proposed method to do this is to make extremely precise measurements of the anisotropies of CMB. The sources of these anisotropies is thought to be a result of the primordial perturbations imprinted in the universe after inflation.

Once inflation has ended and reheating is over the universe is very hot and has an extremely uniform density with fluctuations as I have described above. This high temperature means that electrons are dissociated from protons. This plasma scatters photons causing the universe to be opaque. As the universe expands, it cools. When the universe is cool enough, such that the electrons are captured by the protons and hydrogen is formed, it then becomes transparent. This leaves the previously constantly

scattering photons free to propagate through the universe. This primordial light we call the CMB. The conditions in the Universe at the time these photons receive their last scattering defines what we measure today in the CMB. Last scattering happened 400,000 yrs after the Big Bang, ≈ 13 Billion yrs ago, the CMB is therefore often referred to as a “baby picture” of the universe.

1.3.1 Temperature fluctuations

The originally flat (or close to flat) power spectrum of density perturbations evolves over time between the end of inflation and the surface of last scattering. The evolution of these perturbations between the end of inflation and last scattering is different for different scales. For scales $k \ll 1/t_* r_s$, where t_* is the time of last scattering and r_s is the sound speed of the primordial plasma, the only evolution is a growth in the size of fluctuations due to gravity. On smaller scales photon pressure causes the photon baryon fluid to evolve differently. For small scales the higher density causes higher photon pressure which reverses the infall. This causes rarifications, which then can collapse due to the negative pressure. This cycle of sound waves collapsing and expanding can be seen in the CMB. The smaller the scale the faster this cycle of collapse and expansion. This imprints the so-called Baryon Acoustic Oscillations (BAO) on the CMB. To be able to see this signal we must measure the angular power spectra of the CMB. We decompose the temperature fluctuations ΔT of the CMB into spherical harmonics, $a_{\ell m}^T$. Then the power spectrum, C_ℓ^T , is the 2-point correlation function. Explicitly,

$$a_{\ell m}^T = \int d\mathbf{u} \Delta T(\mathbf{u}) Y_{\ell m}^*(\mathbf{u}) \quad (1.19)$$

$$C_\ell^T = \langle a_{\ell m}^T a_{\ell m}^{T*} \rangle \quad (1.20)$$

where the brackets denote average over many realisations of the CMB and $\mathbf{u} = [\theta, \phi]$ are coordinates that define the sphere. The power spectrum at a particular ℓ is the variance of the $a_{\ell m}^T$ for that ℓ . It is therefore the size of the fluctuations of the CMB

temperature at different angular scales $\theta \sim \pi/\ell$. An estimate of the CMB temperature power spectrum can be made from the observed CMB by calculating,

$$\hat{C}_\ell^T = \frac{1}{2\ell + 1} \sum_m |a_{\ell m}^T|^2. \quad (1.21)$$

The temperature fluctuations have been measured to an extremely high accuracy, see Figure 1.1 for the latest results by the *Planck* experiment (Planck Collaboration et al. 2015a). We can see peaks in the spectrum at scales which correspond to where an integer number of cycles has occurred. The odd peaks correspond to over densities due to gravitational collapse, the even peaks are rarifications.

A second main feature of the CMB power spectrum is an exponential decay of the power on small scales. As recombination is taking place the mean free path of the photons starts to increase, until ultimately it becomes infinite and the CMB is released. During this process the photons scatter off the electrons of the plasma smoothing the small scale structure due to the large mean free path.

The temperature power spectrum is heavily dependent on the fractional energy densities of the constituents of the Universe. The cosmological parameters are constrained by finding the most likely set of cosmological parameters that recreate the observed power spectra. Due to the high precision of the measurements of the temperature fluctuations the fractional densities are highly constrained and fully consistent with a Λ CDM cosmology (Planck Collaboration et al. 2015a).

The parameters that are most important for inflation, n_s and r , however are not well constrained by temperature power spectra alone. The large range of scales measured by *Planck* does constrain the tilt of the scalar perturbations, n_s . However, the tensor to scalar ratio is not constrained well. The polarization of the CMB can place much tighter constraints on r , a topic covered in the next Section.

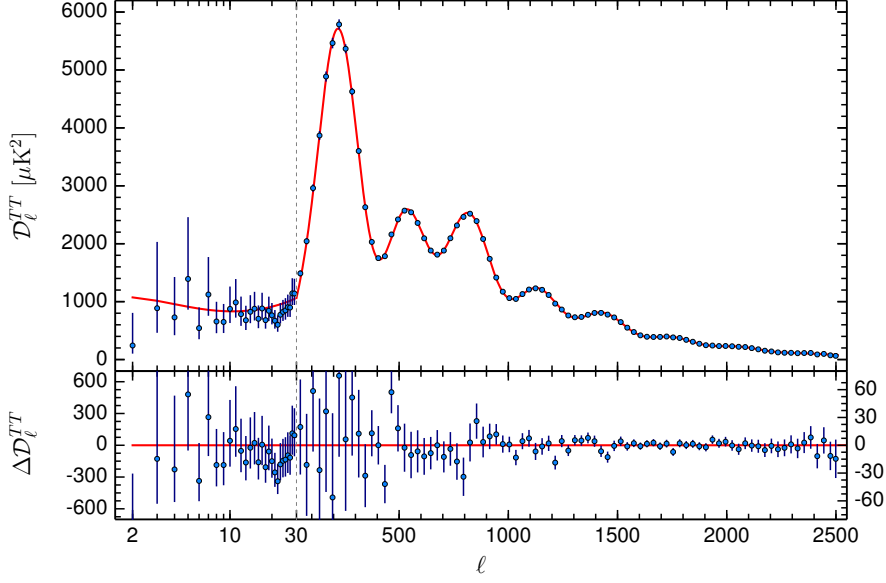


Figure 1.1: Measurements of the temperature fluctuation power spectrum from the *Planck* experiment, with the best fit Λ CDM cosmology. On the vertical axis $D_\ell = \ell(\ell + 1)C_\ell/2\pi$. The figure is taken from (Planck Collaboration et al. 2015a)

1.3.2 Polarization of the CMB

To understand how the polarization can help us measure r we must first understand how the CMB becomes polarized. Before doing this though we define the decomposition of the polarization. Polarization is a spin-2 quantity, in that rotating it through 180° takes it back on to itself. It is described by the Stokes parameters Q and U . Q measures the polarisation along the x - and y -directions by being negative and positive respectively. U describes polarisation similar to Q but rotated by 45° . This is demonstrated by Figure 1.2. As polarisation is spin-2 we decompose polarization into spin-2 spherical harmonics,

$$(Q \pm iU)(\mathbf{u}) = \sum_{\ell m} (a_{\ell m}^E \mp i a_{\ell m}^B)_{\mp 2} Y_{\ell m}(\mathbf{u}), \quad (1.22)$$

where $a_{\ell m}^E$ and $a_{\ell m}^B$ are the expansion of the E -mode and B -mode polarisation. E -mode polarisation has the property that for a particular Fourier mode \mathbf{k} the direction of the polarisation is parallel or perpendicular to \mathbf{k} . By contrast, B -mode polarisation

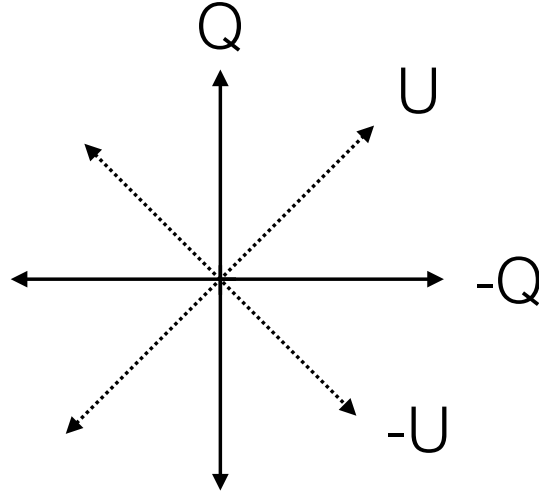


Figure 1.2: A diagram to show the Stokes parameters Q and U , used to represent polarisation.

would have a polarisation angle 45° to \mathbf{k} . We also define the power spectra C_ℓ^{XY} ,

$$C_\ell^{XY} = \frac{1}{2\ell + 1} \sum_m a_{\ell m}^X a_{\ell m}^{Y*}, \quad (1.23)$$

where $X, Y = \{T, E, B\}$.

The CMB will become polarized at recombination when the photons start to become decoupled from the baryons. The Thomson scattering cross section depends on the polarization of the incident photon \mathbf{n} and the polarization of the scattered photon \mathbf{n}' as (Chandrasekhar 1960),

$$\frac{d\sigma_T}{d\Omega} \propto |\mathbf{n} \cdot \mathbf{n}'|^2. \quad (1.24)$$

So the outgoing radiation preferentially travels orthogonal to the incoming polarization and with a polarization parallel to the incoming polarization. Let us apply this to the last scattering of the photons that make up the CMB. The incoming radiation will not be polarized (Hu & White 1997), so a polarization can only occur by differential

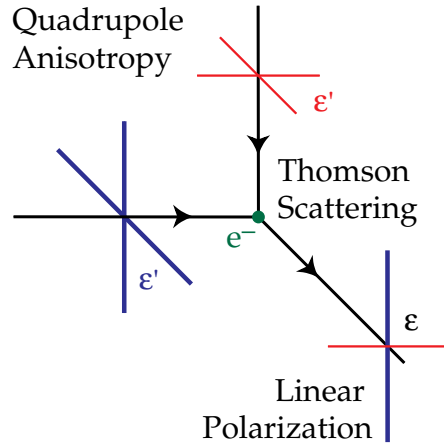


Figure 1.3: Thomson scattering of radiation with a quadrupole anisotropy generates linear polarization. Blue colors (thick lines) represent hot and red colors (thin lines) cold radiation. Figure and caption taken from (Hu & White 1997).

illumination of a region. For a graphical explanation see Figure 1.3.

As the polarization will be due to quadrupolar illumination, it is then logical to look at how such an illumination can come about. There are 2 main ways in which this type of illumination can occur. One due to regions of the universe being hotter than others, which will be a result of the scalar perturbations already discussed. The other way is from the tensor perturbations.

Scalar perturbations

We consider a plane wave of an effective temperature fluctuation, where we define the effective temperature $(\Delta T/T)_{eff} = (\Delta T/T) + \Psi$ to eliminate the effect of gravitational red-shifting. This means that hotter effective temperature regions always radiate more than colder effective temperature (Hu & White 1997). We place the origin at a trough of this plane wave which oscillates in the z direction, see Figure 1.4. The differential intensity of the light goes as $Y_{20} \propto 3 \cos^2 \theta - 1$. This incoming radiation is then scattered and this scattered radiation is polarized (Hu & White 1997) as,

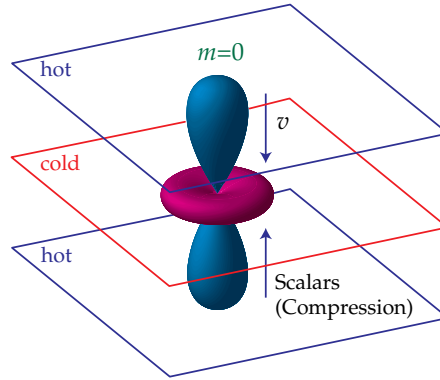


Figure 1.4: The scalar quadrupole moment ($\ell = 2, m = 0$). Flows from hot (blue) regions into cold (red), $\mathbf{v} \parallel \mathbf{k}$, produce the azimuthally symmetric pattern Y_{20} depicted here. Figure and caption taken from (Hu & White 1997).

$$Q = \sin^2 \theta, \quad U = 0. \quad (1.25)$$

Tensor perturbations

We consider a similar process for plane gravitational waves. We set the wave up to travel in the z direction. The stretching and contraction of space will red- and blue-shift the received photons at the origin. This will create a differential illumination like that shown in Figure 1.5. The functional form of the differential illumination is $Y_{2\pm 2} \propto \sin^2 \theta e^{\pm 2i\phi}$, giving us a polarization of (Hu & White 1997)

$$Q = (1 + \cos^2 \theta) e^{2i\phi}, \quad U = -2i \cos \theta e^{2i\phi}. \quad (1.26)$$

Relating the local polarization to polarization on the sky

We have seen the polarization due to simple plane waves of scalar and tensor perturbations, described in a coordinate system centered on the scattering. We now look at the result from a coordinate system centred on the observer. As the we place the emitting

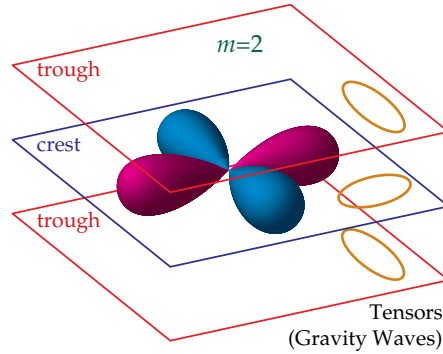


Figure 1.5: The tensor quadrupole moment ($m = 2$). Since gravity waves distort space in the plane of the perturbation, changing a circle of test particles into an ellipse, the radiation acquires an $m = 2$ quadrupole moment. Figure and caption taken from (Hu & White 1997).

point at last scattering then move it round the sky we can see the effect is simply to have a polarization on the sky of the same form as the emission.

Now we consider the modulation and how the scalar and tensor polarizations contribute to the decomposition in equation 1.22. We go to the flat sky limit to be able to visualize the result.

In the flat sky limit, looking in the $\theta = \pi/4$ and $\phi = 0$ region of the sky, the polarization decomposition looks like,

$$(Q \pm iU)(\mathbf{x}) = \sum_{\mathbf{l}} (a_{\mathbf{l}}^E \mp ia_{\mathbf{l}}^B) e^{\mp 2\phi_1} e^{i\mathbf{x} \cdot \mathbf{l}}, \quad (1.27)$$

where $\mathbf{l} = \ell[\cos \phi_1, \sin \phi_1]$. We align our \mathbf{e}_y axis with \mathbf{e}_θ . We consider the scalar plane wave again, so $(\Delta T/T)_{eff} \propto \cos(y)$. Therefore, the polarization as a result will now go as $Q \propto \cos(y)$, $U = 0$. One can easily see that the decomposition will only contain $a_{\mathbf{l}}^E$ which is non-vanishing. Alternatively we can see that as the polarisation direction is in the same direction or perpendicular to the Fourier mode it is an E -mode. This is a general result: scalar perturbations only create E -mode polarization.

We now consider the plane gravitational wave causing the CMB to be polarized in the patch of the sky, $\theta = \pi/4$ and $\phi = 0$. Again the modulation of the gravitational wave is the the direction of \mathbf{e}_y so $Q = 3\alpha \cos(y)/2$ and $U = \sqrt{2}\alpha \sin(y)$, where α is

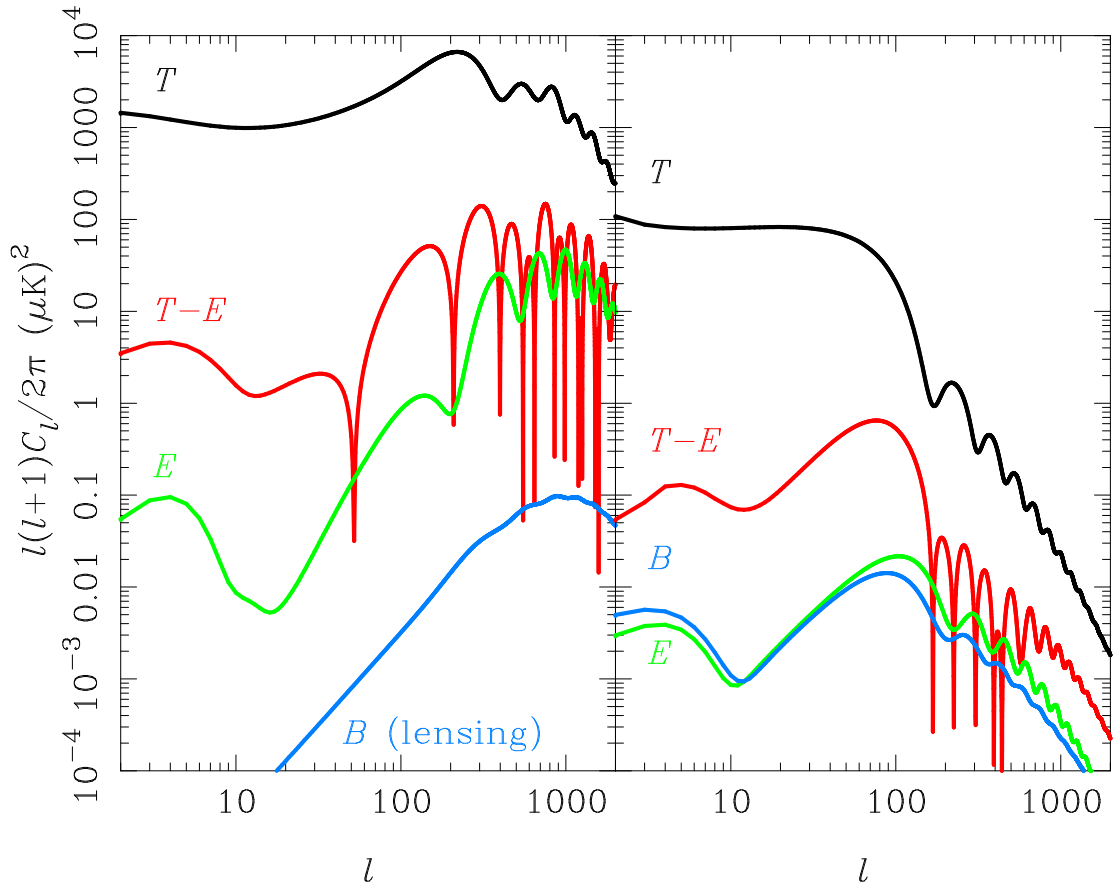


Figure 1.6: Temperature (black), E-mode (green), B-mode (blue) and T-E cross-correlation (red) CMB power spectra from scalar perturbations (left) and tensor perturbations (gravitational waves; right). The amplitude of the tensor perturbations (r) is 0.22. The B-mode spectrum induced by weak gravitational lensing is also shown in the left-hand panel (blue). Figure and caption taken from Challinor & Peiris (2009).

a constant. Now as we have Q and U polarization the decomposition will contain both E - and B -modes, as the polarisation direction has contributions along and at 45° to the direction of the mode.

This leads us to an exciting result. The B -mode polarization of the CMB will be a result of gravitational waves only. Other effects of primordial tensor perturbations are washed out by the scalar perturbation due to the small value of r (Challinor & Peiris 2009). See Figure 1.6 for the predicted power-spectra due to scalar and tensor perturbation for $r = 0.22$. The effect of the value of r on the power spectra due to gravitational waves is to raise or lower the amplitude of the power spectra.

1: INTRODUCTION

There is B -mode polarization due to the scalar perturbations in Figure 1.6. This is due to gravitational lensing of the CMB since last scattering, an effect we have not considered so far. Weak lensing deflects the CMB photons but does not change the polarisation direction. This distortion of the E -mode pattern creates B -mode polarisation. The B -mode polarization from scalar perturbations is at much higher values of ℓ than the tensor perturbation B -modes leaving us a clean window in the B -mode polarization at $\ell \lesssim 200$ to measure the gravitational waves from inflation, assuming the value of r is high enough. A measurement of this kind would be an incredible achievement for science, one would have not only directly detected gravitational waves but also measured the energy scale of inflation, current upper bounds place the energy scale $< 4.39 \times 10^{14}$ GeV at 95% confidence (Planck Collaboration et al. 2015d). This will allow us to probe into particle physics at energies much higher than particle accelerators can reach.

1.3.3 Current CMB polarisation measurements

Great progress has been made in the field of CMB polarisation in recent years. The culmination of years of work has led the *Planck* satellite to make the deepest measurements of the large scale E -mode power spectrum (Planck Collaboration et al. 2015e), see Figure 1.7. The E -polarisation power spectra are yet another confirmation of the Λ CDM paradigm. Due to certain not fully understood systematic effects the B -mode power spectra and the E -mode power spectra for $\ell < 30$ are not fully public at the time of writing. As a result the best measurements and upper bounds on the B -mode power spectrum has come from ground based experiments.

BICEP2 have made the deepest polarisation maps of the 150 GHz sky, this led to very intriguing result where large scale B -mode power spectrum consistent with a tensor-to-scalar ratio of 0.2 was detected (BICEP2 and Keck Array Collaborations et al. 2015). Unfortunately, the B -mode polarization was later shown to be as a result of polarized dust emission from within our galaxy (BICEP2/Keck and Planck Collabora-

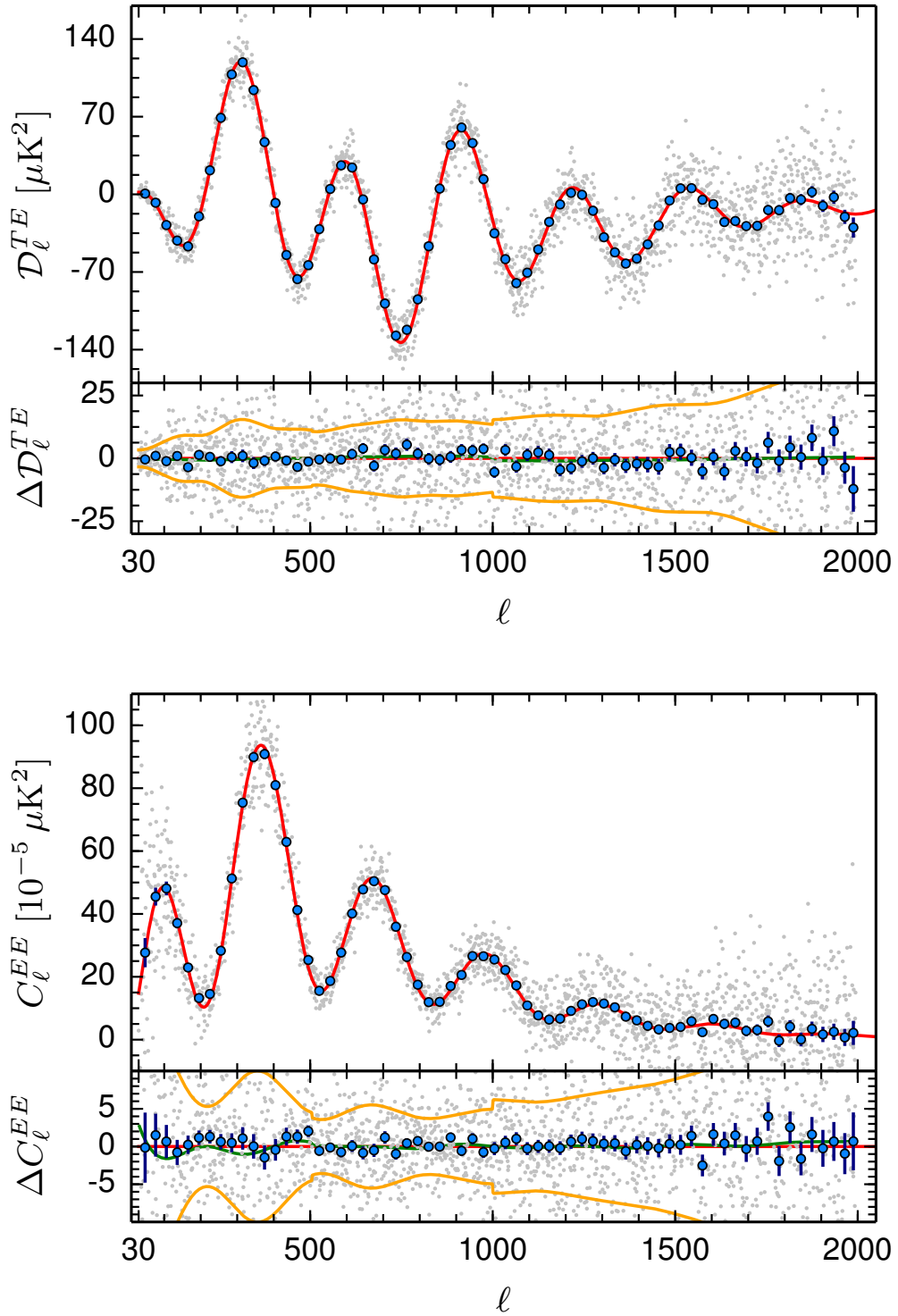


Figure 1.7: The TE and EE cross and power spectra measured by *Planck*. The blue points are for bins of $\Delta\ell = 30$, while the grey points are unbinned. The lower panels show the residuals with respect to the best fit ΛCDM model. The yellow lines show the 68% unbinned error bars. Figure and caption adapted from Planck Collaboration et al. (2015e)

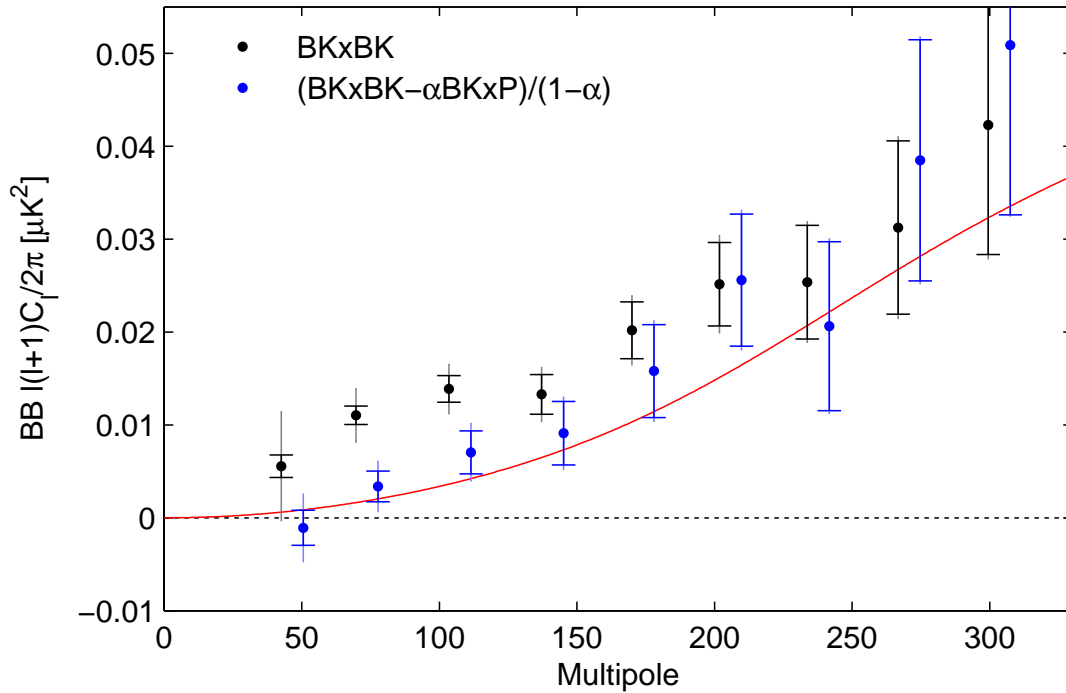


Figure 1.8: BB spectrum of the BICEP2/Keck maps before and after subtraction of the dust contribution, estimated from the cross-spectrum with *Planck* 353 GHz. The error bars are the standard deviations of simulations, which, in the latter case, have been scaled and combined in the same way. The inner error bars are from lensed- Λ CDM+noise simulations as in the previous plots, while the outer error bars are from the lensed- Λ CDM+noise+dust simulations. The red curve shows the lensed- Λ CDM expectation. Figure and caption taken from BICEP2/Keck and Planck Collaborations et al. (2015)

tions et al. 2015). Figure 1.8 shows the B -mode power spectrum in the BICEP2 field, the black points are the power spectrum of the BICEP maps and the blue points are the BICEP power spectra with a scaled BICEP-*Planck* 353 GHz map cross spectra subtracted. The 353 GHz *Planck* map is considered to be primarily a detection of polarised dust. The low ℓ bump visible in the BICEP power spectra, which previously was considered to be to primordial gravitational waves, is therefore shown to be a result of polarized dust in our Galaxy.

As deeper maps of the CMB are made in an attempt to measure the large scale B -mode polarisation of the CMB, foreground emission will become ever increasingly problematic. Until recently CMB experiments have been able to observe the CMB

directly and avoid regions where the foreground emission was strong. However, in order to make the deep CMB polarization maps required to detect primordial B -mode polarisation it is becoming apparent that foreground removal will be required.

The POLARBEAR and SPT collaborations in the few last years have made the first detections of the lensed B -mode power spectrum on small scales (The Polarbear Collaboration: P. A. R. Ade et al. (2014), Keisler et al. (2015)). On these angular scales the problems that effected BICEP are less problematic as dust polarization of the power spectrum that falls at high ℓ . Figure 1.9 shows the current status of detections of the lensed B -mode power spectrum.

This proves to be an exciting time for the CMB and wider cosmology communities. The measurements of small scale B -mode power spectrum will allow for accurate measurements of the large scale structure between us and surface of last scattering. But also measurements of the large scale B -mode power spectrum are reaching sensitivities where inflation models can be ruled out, or even more excitingly, confirmed.

1.4 Systematic effects in CMB polarisation experiments

The E -mode power spectrum is approximately two orders of magnitude fainter than the temperature power spectrum while the B -mode power spectrum is expected to be at least 2 orders of magnitude fainter still (Challinor 2013). This means that in any experiment aimed at detecting B -modes, systematic effects that could potentially couple the temperature or E -mode signal to the B -mode power spectrum must be strictly controlled. One source of potential error is an asymmetric optical response function (i.e. the experimental beam). During the data analysis for CMB experiments, one often assumes that the beam is axisymmetric so that its effect is to simply isotropically smooth the sky. This assumption can result in a bias in subsequent power spectrum estimates if, as is often the case in reality, the beam is not perfectly axisymmetric. In this thesis we consider asymmetric beam shapes and present a number of techniques to remove any bias that they introduce.

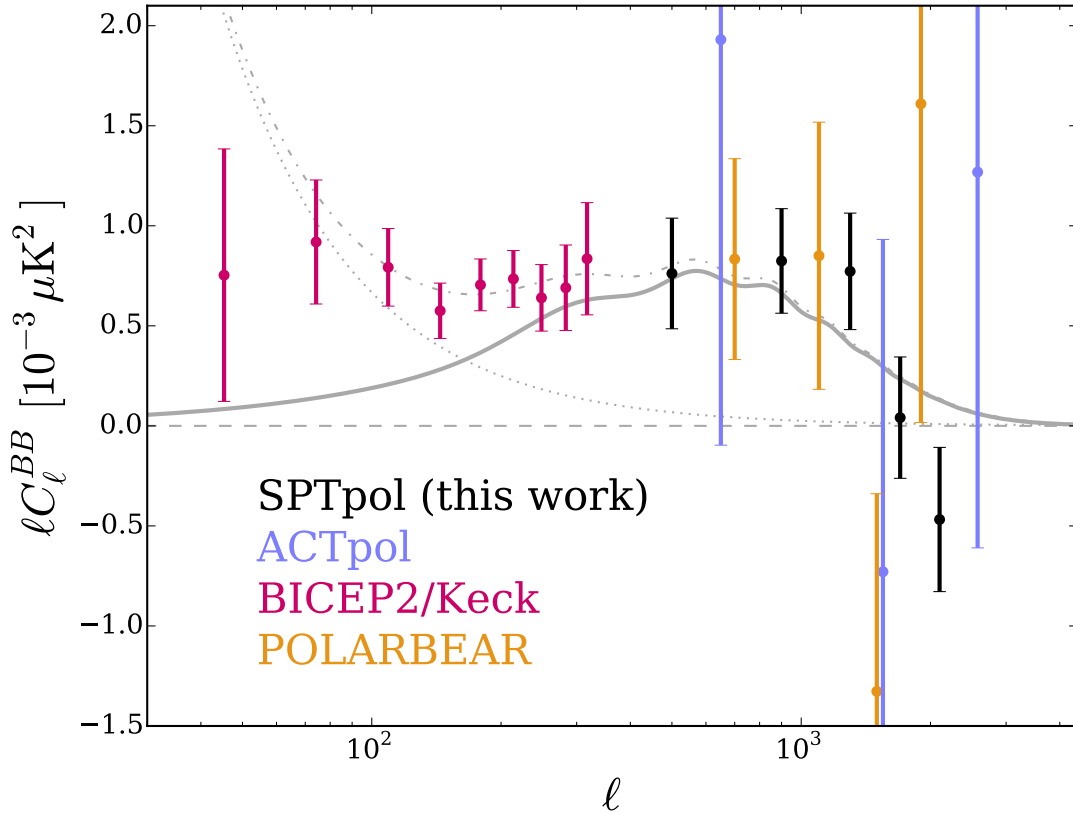


Figure 1.9: BB power spectrum measurements from SPTpol (Keisler et al. 2015), ACTpol (Naess et al. 2014), BICEP2/Keck (BICEP2 and Keck Array Collaborations et al. 2015), and POLARBEAR (The Polarbear Collaboration: P. A. R. Ade et al. 2014). The highest multipole bin of the ACTpol data is not shown. The solid gray line shows the expected lensed BB spectrum from the Planck+lensing+WP+highL best-fit model in Table 5 of Planck Collaboration et al. (2015c). The dotted line shows the nominal 150 GHz BB power spectrum of Galactic dust emission used in this work. This model is derived from an analysis of polarized dust emission in the BICEP2/Keck field using Planck data (Planck Collaboration et al. 2014a). The dash-dotted line shows the sum of the lensed BB power and dust BB power. Figure and caption taken from Keisler et al. (2015).

1.4.1 Theoretical predictions of error on the recovered B -mode power spectrum

A number of pieces of work have looked into predicting the systematic error on the recovered B -mode power spectrum. Hu, Hedman & Zaldarriaga (2003) looked at errors in experiments which vary in a Gaussian fashion. This work while very useful was

limited when considering beam imperfections that are often constant over the course of an experiment. Due to the incoherence of the model of the systematic effects that Hu et al. (2003) considered, the error on the B -mode power spectrum had a similar shape as a noise bias for scales smaller than the beam scale.

O’Dea, Challinor & Johnson (2007) and Shimon et al. (2008) looked at imperfections in an experiment that are constant with time. As the temperature power spectrum is at least 4 orders of magnitude higher than the B -mode power spectrum any leakage between T and B is problematic. As most modern CMB experiments are differencing experiments, the systematic effects that the authors’ consider are typical of a differencing experiment. A differencing experiment uses two detectors sensitive to orthogonal polarisation directions, sensitive to the same region of sky. The responses from the two detectors are then summed and differenced to obtain an estimate of the temperature and polarisation of the sky. Any differences between the temperature response of the two detectors will therefore leak temperature fluctuations to polarisation.

Three types of systematic effects, that leak temperature to polarisation, that I consider are distinguished by how they transform under rotations of the telescope. Fig. 1.10 shows the leakage to Stokes Q for the three types of leakage; dipole, quadrupole and monopole leakage. As one rotates the telescope, keeping it pointed at the same point the polarisation signal will rotate in a spin-2 fashion.

Monopole, spin-0, leakage can be sourced from isotropic differences in the two temperature beams of the detector pair. This can be either a constant mis-calibration or a difference in the width of the beam. Dipole, spin-1, leakage is most easily created by a mis-alignment of the two temperature beams. Finally quadrupole, spin-2, leakage is created by a difference in the ellipticity of the temperature beams.

The functional form of the systematic effects under rotation is crucial when considering their impact on science. For the systematic effects that rotate with a different spin to polarisation the leakage can be mitigated by observing a pixel at many orientations of the telescope. This will have the effect of averaging the leakage to a much lower value. For the quadrupole, spin-2, leakage however, this is not the case. As both the

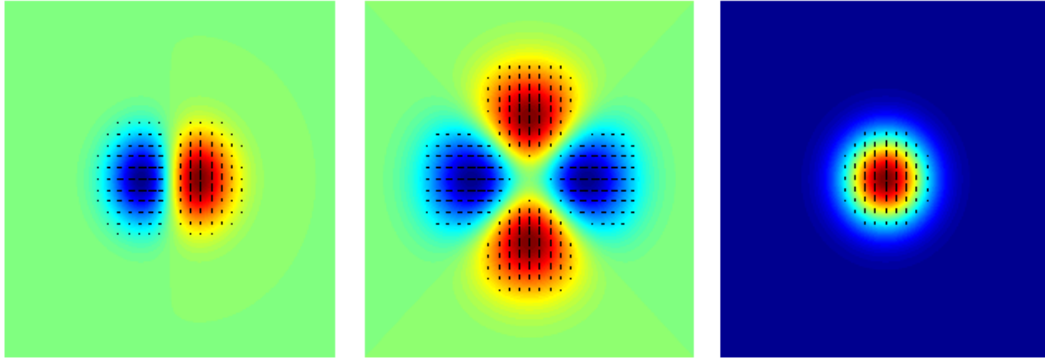


Figure 1.10: An illustration of the dipole, quadrupole and monopole effects; Q parameter only is depicted. Figure and caption adapted from Shimon et al. (2008).

systematic error and polarisation signal transform in the same way this leakage cannot be averaged down by many orientations.

1.4.2 Current techniques to remove systematic effects

Currently there are number of approaches in the literature that attempt to deal with systematic effects related to beam systematics. The first is simply to quantify the systematic error on the cosmological parameters caused by the experiment's imperfections and be satisfied that they are below the statistical uncertainty. This can be done by simulating an experiment's full beam response (Mitra et al. 2011) and propagating the error (Planck Collaboration et al. 2014d). This approach is effective as the error in the maps can be estimated. In the *Planck* experiment the asymmetry bias was shown to have little to no effect on the science (Planck Collaboration et al. 2014b). Other experiments such as the POLARBEAR collaboration perform detailed simulations of the instrumental set up and use knowledge of the temperature sky to simulate the effects of any imperfections on the recovered B -mode power spectrum. This was done very successfully by the POLARBEAR collaboration in their detection of the lensing B -modes (The Polarbear Collaboration: P. A. R. Ade et al. 2014) where they showed the temperature to polarisation leakage was much lower than their detected signal.

While effective, this method does not remove the systematic effect, rather it simply quantifies it. The second method investigated attempts a full deconvolution of the Time Ordered Data (TOD) from a CMB experiment to remove the effect of beam asymmetry bias completely (Wandelt & Górski 2001; Challinor et al. 2000; Keihänen & Reinecke 2012). The results of this method are encouraging but it is not able to deal with certain unavoidable real-world complications. In particular when noise is added to the TOD the deconvolution no longer works for high multipoles. In addition, the deconvolution only works if the experiment observes the entire sky as the convolution attempts to fit for all the spherical harmonics. This is not a significant problem for satellite-based experiments but for ground- or balloon-based experiments this will obviously not be the case.

A third approach is to calculate, and subsequently correct for, the asymmetry bias on the measured pseudo- C_ℓ in an experiment (Ramamonjisoa et al. 2013; Souradeep et al. 2006). As presently formulated this is unable to deal with a cut sky without apodising the azimuthal dependence of the mask. This in turn results in a reduction of the cosmological information content of the TOD which is something that we would like to avoid. In addition, these authors assume that each sky pixel is seen in a single orientation only, whereas, in general, experiments will observe each sky pixel in a number of different orientations. The *Planck* collaboration use an isotropic beam profile in their analysis that best represents the full asymmetric beam. This is based on work that calculates the full effect of the asymmetric beam by Hanson et al. (2010).

The final category deals with removing temperature to polarisation leakage. This involves calculating the coupling by fitting the parameters describing imperfections in the experiment, and then subtracting this coupling using CMB temperature measurements. This technique was shown to be effective in the analysis of BICEP2 (BICEP2 Collaboration et al. 2014, see their figure 5). However, there is a question as to whether this de-projection technique would work as effectively with a more complex scan strategy. In addition, the fitting procedure employed also removes some polarisation signal. This results in a leakage of E -modes to B -modes which must be simulated and

removed in the power spectrum estimation (BICEP2 Collaboration et al. 2015).

1.4.3 Work in this thesis

This thesis attempts to expand this body of work. Firstly in Chapter 2 I look at the physics of multi-moded horns. Due to their increased sensitivity there is some interest in using multi-moded horns to detect B -mode polarisation (LSPE Collaboration et al. 2012). This chapter looks at the physics that allows one to predict the beam shape resulting from a multi-moded horn in an attempt to identify any features that could be beneficial in systematic effect removal.

In Chapter 3 I then go on to describe and demonstrate the effectiveness of a new pseudo- C_ℓ estimator capable of recovering the temperature and polarisation power spectra when a general beam is used. This is an extension of Hanson et al. (2010) where the authors write down a pseudo- C_ℓ estimator suitable for a temperature experiment. Chapter 3 also presents a new map making algorithm capable of creating temperature and polarisation maps free of beam asymmetry bias.

I then go on to develop a new map making algorithm that can remove temperature to polarisation leakage in Chapter 4. This is based on separating the spin systematic effects and that of polarisation. I show that it is capable of removing temperature leakage from experimental imperfections that affected BICEP2 (BICEP2 Collaboration et al. 2014).

Finally in Chapter 5 I examine the role that scan strategies can have on mitigating systematic effects. By exploring satellite scan strategy parameter space I identify the most important parameters that allow multiple crossing angles of the scans, therefore averaging the systematic error down.

Chapter 2

Waveguides

In this chapter I review the physics of multi-moded horns. Due to their increased sensitivity there is some interest in using multi-moded horns to detect B -mode polarisation (LSPE Collaboration et al. 2012). This chapter looks at the physics that allows one to predict the beam shape resulting from a multi-moded horn in an attempt to identify any features that could be beneficial in systematic effect removal. Starting from Maxwell's equations I show the possible modes present in a cylindrical waveguide. Then I examine the beam patterns that arise from these modes. I describe how to calculate a beam given an electric field at the aperture. The determination of the electric field at an aperture is then briefly discussed. This part of the work is heavily guided by Oliver et al. (1994). Once we have understood the basis modes and their beams, then I apply that knowledge to multi-moded horns, to create a formalism that allows prediction of the beam pattern.

2.1 Allowed modes in a cylindrical waveguide

I begin by looking at the electric field in a circular wave guide of radius a . For an oscillating electric field, $\mathbf{E} = \mathbf{E}_0 e^{i\omega t}$, the Ampère and Faraday laws, in the presence of

2: WAVEGUIDES

no charges, can be written as

$$\nabla \times \mathbf{E} - \frac{i\omega}{c} \mathbf{B} = 0, \quad (2.1)$$

$$\nabla \times \mathbf{B} + \frac{i\omega}{c} \mathbf{E} = 0. \quad (2.2)$$

By taking the curl of equation (2.1) and then substituting in (2.2) a wave equation can be found for \mathbf{E} (noticing that $\nabla \cdot \mathbf{E} = 0$ as we assume no charges are present). The reverse process can be done to find a wave equation for \mathbf{B} giving us,

$$\left(\nabla^2 + \frac{\omega^2}{c^2} \right) \begin{pmatrix} \mathbf{E} \\ \mathbf{B} \end{pmatrix} = 0. \quad (2.3)$$

We require solutions of the form $\mathbf{E} = \mathbf{E}(r, \phi)e^{i(\gamma z - \omega t)}$, so the mode propagates along the waveguide¹. Substituting this into our wave equation and considering only the z -component of the field, gives us,

$$(\nabla_t^2 + K^2) \begin{pmatrix} E_z \\ B_z \end{pmatrix} = 0, \quad (2.4)$$

where $K^2 = (\omega/c)^2 - \gamma^2$ and ∇_t^2 is the Laplacian operator only concerned with the components perpendicular to the direction of propagation. These partial differential equations are solved with the boundary conditions that $E_z = 0$ and $\partial_r B_z = 0$ at the surface of the cylinder to give us,

$$E_z = A_{2nm} J_n(K_{2nm} r/a) e^{in\phi}, \quad (2.5)$$

$$B_z = A_{1nm} J_n(K_{1nm} r/a) e^{in\phi}, \quad (2.6)$$

where $J_n(x)$ are the Bessel functions of the first kind, K_{2nm} is the m^{th} root of $J_n(x)$ and K_{1nm} is the m^{th} root of $\frac{dJ_n}{dx}(x)$. The modes where E_z is null are often called

¹Modes can exist in a waveguide that do not propagate, in this definition these modes are associated with a imaginary value of γ , and therefore the amplitude decays exponentially down the waveguide

TE_{*nm*} modes and the modes of null B_z are called TM_{*nm*}. Here I, simply denote the electric field of a particular mode by \mathbf{E}_{inm} with $i = 1$ and $i = 2$ referring to the TE and TM modes respectively. Figure 2.1 shows the the first five Bessel functions. Where a Bessel function crosses the x -axis $x = K_{inm}$ for a TM mode, where there is a stationary point $x = K_{inm}$ for a TE mode.

By substituting are required solution into (2.1) and (2.2) it can also be shown that the transverse fields are simply functions of E_z and B_z and are,

$$\mathbf{E}_{inm} = -\frac{\gamma}{K_{inm}} \nabla_t E_{inm}^z + \frac{i\omega}{K_{inm}} \hat{\mathbf{z}} \times \nabla_t B_{inm}^z, \quad (2.7)$$

$$\mathbf{B}_{inm} = -\frac{\gamma}{K_{inm}} \nabla_t B_{inm}^z + \frac{i\omega}{c^2 K_{inm}} \hat{\mathbf{z}} \times \nabla_t E_{inm}^z. \quad (2.8)$$

These modes are orthogonal and form a complete basis, that is, to-say any electric field in a cylinder can be described by a linear combination of these modes.

2.2 Calculating beams

By the theory of reciprocity, the beam profile of a horn when used as a detector is the same as that if the horn was used to emit radiation. The latter is calculated as it is conceptually easier and the theory is applied in order to understand how the horn will respond when used to detect the sky.

When detecting the polarization of the sky the coupling of the horn to radiation polarised in different directions is obviously of great importance. We can calculate this when we calculate the radiated beam. All we have to do is assign a polarisation direction to our field in the aperture. This is usually assigned to the direction where most of the field is polarised. For example see Figure 2.5, the electric field at the aperture of the TE11 mode has an obvious polarisation in the x direction. When the beam this field creates is calculated, we define radiation that is polarised parallel and perpendicular to this direction as the co-polarisation and cross-polarisation, respectively. This

2: WAVEGUIDES

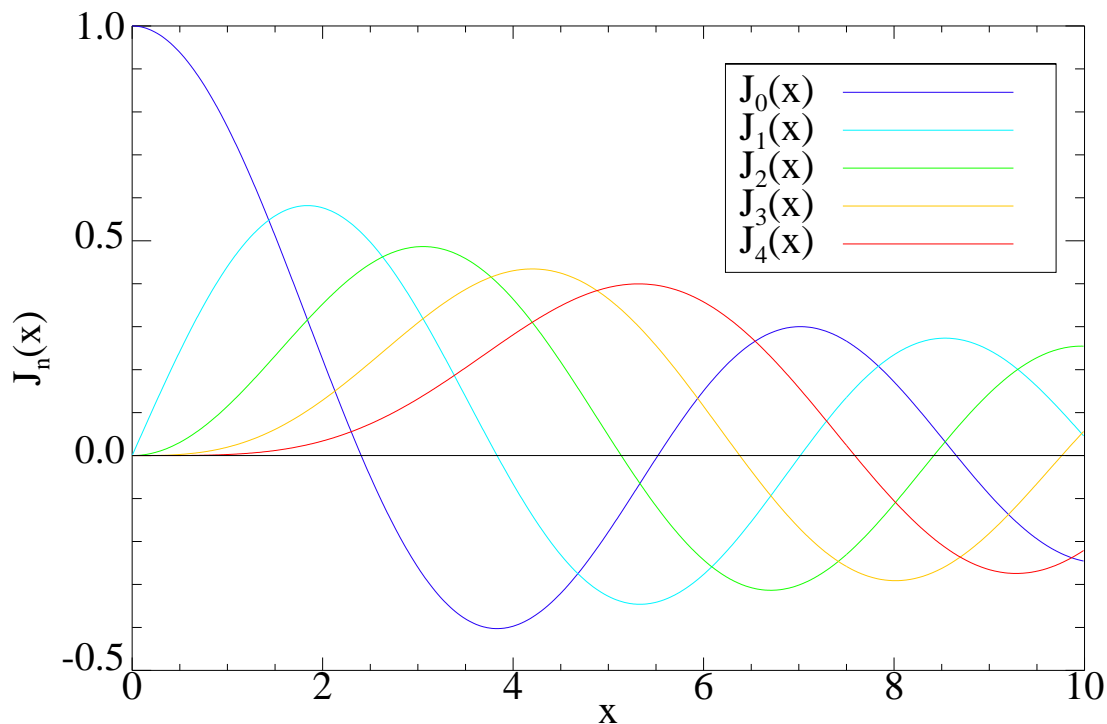


Figure 2.1: The plot shows the first five Bessel functions. Where a Bessel function crosses the x -axis $x = K_{2nm}$ for a TM mode, where there is a stationary point $x = K_{1nm}$ for a TE mode.

statement is only true in the small angle approximation: there are many definitions of co- and cross-polarisation. For more information see Ludwig (1973). For the other modes shown in Figure 2.5 the polarisation has a less obvious general direction. This results in a stronger cross-polarisation response.

We can now define electric field far from the horn to be

$$\mathbf{E}_{\text{far}} = \begin{pmatrix} E_{\text{co}} \\ E_{\text{cross}} \end{pmatrix}. \quad (2.9)$$

A strong the cross polarisation response is problematic for polarisation experiments, therefore, a large amount of work is spent in designing and building a telescope to minimise this cross polar response.

2.2.1 Finding the far-field radiation pattern

To find the far-field radiation pattern of a horn one applies a field equivalence relation. One relation that is often chosen states that: if we define our aperture to be at $z = 0$, then the field at $z > 0$, is the same whether we have the source fields in the region $z < 0$, or we have a set up of electric and magnetic currents, in a perfect conductor, on the plane $z = 0$. The electric (\mathbf{J}_s) and magnetic (\mathbf{J}_m) current surface densities are given by

$$\mathbf{J}_s = -\epsilon_0 c^2 \hat{\mathbf{z}} \times \mathbf{B}(z = 0), \quad (2.10)$$

$$\mathbf{J}_m = -\hat{\mathbf{z}} \times \mathbf{E}(z = 0), \quad (2.11)$$

These current surface densities are motivated by Maxwell's third and fourth equations where we have included a magnetic current. These can be deduced by considering a rectangular loop, with one side outside the conductor and one inside the conductor, then by applying Maxwell's third and fourth equations (with a magnetic current modification),

$$\oint_L \mathbf{E} \cdot d\mathbf{l} = \int_S \mathbf{j}_m \cdot d\mathbf{S} - \frac{\partial}{\partial t} \int_S \mathbf{B} \cdot d\mathbf{S}, \quad (2.12)$$

$$c^2 \oint_L \mathbf{B} \cdot d\mathbf{l} = \frac{1}{\epsilon_0} \int_S \mathbf{j}_s \cdot d\mathbf{S} - \epsilon_0 c^2 \frac{\partial}{\partial t} \int_S \mathbf{E} \cdot d\mathbf{S}. \quad (2.13)$$

where $\mathbf{j}_m = \mathbf{J}_m \delta(z)$ and $\mathbf{j}_s = \mathbf{J}_s \delta(z)$ are current densities and their relation to the current surface densities in equations (2.10,2.11). This equivalence principle and modification to Maxwell's equations reproduce standard Maxwell's equations completely. By considering the perfect conductor simply allows us to place a boundary on our calculations at the aperture, these currents and condition allow us to separate the in horn and far-field calculations.

Figure 2.2 shows the loop over which we perform the line integral in equation

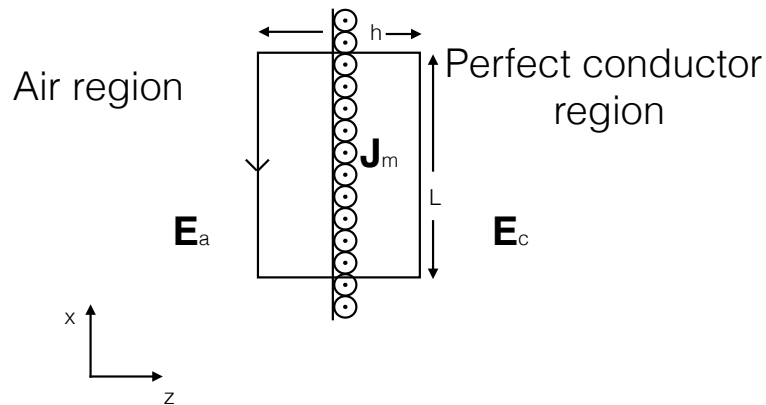


Figure 2.2: Diagram to define the loop and variables applied to equation (2.12). The box represents the loop for the integration with the arrow showing the direction of the line integral. There is a surface magnetic current density in the y -direction in the conductor denoted by \mathbf{J}_m and the electric fields inside and outside the conductor are denoted by \mathbf{E}_c and \mathbf{E}_a respectively.

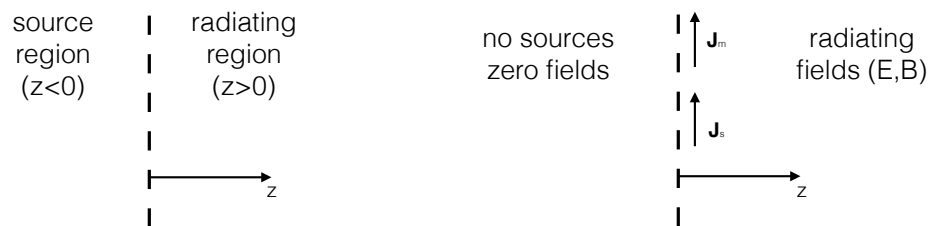


Figure 2.3: Schematic diagram of the equivalence principle used. The field in the region $z > 0$ is the same whether sourced by currents at $z = 0$ or source fields in the region $z < 0$. from this we can see that only the electric and magnetic fields at the aperture needs to be considered. The figure is adapted from Oliver et al. (1994).

(2.12) and defines our variables. Considering a loop where $h \ll L$ equation (2.12) this gives us,

$$\mathbf{E}_a \cdot (-L\hat{x}) + \mathbf{E}_c \cdot (L\hat{x}) = \mathbf{J}_m \cdot (L\hat{y}), \quad (2.14)$$

we have ignored the second term of the RHS of equation (2.12) as the result is pro-

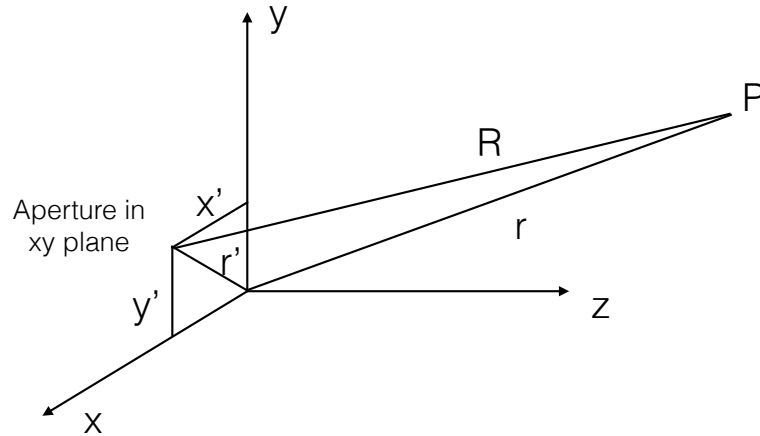


Figure 2.4: Defining variables used to show the far-field radiation pattern is related to the Fourier transform of the electric field at the aperture of the horn. Figure is adapted from Oliver et al. (1994).

portional to h and we consider it to be infinitesimally small. In the perfect conductor limit there is a current density that is only at the surface, leading to the RHS of equation (2.14). In the perfect conductor limit $\mathbf{E}_c \rightarrow 0$ and our result is consistent with equation (2.11). By rotating the loop one can show that in general equation (2.11) is correct and with a similar loop one can also show that equation (2.10) is correct. The current surface densities \mathbf{J}_s and \mathbf{J}_m have no physical meaning but both currents are simply mathematical constructs to allow us to continue. Figure 2.3 shows a schematic diagram of this. Having replaced the fields with current surface densities we can now write down the field potentials at a point P , defined in Figure 2.4, as,

$$\mathbf{A}_s = \int_s \mathbf{J}_s \frac{e^{-ikR}}{4\pi R} ds, \quad (2.15)$$

$$\mathbf{A}_m = \int_s \mathbf{J}_m \frac{e^{-ikR}}{4\pi R} ds, \quad (2.16)$$

where $k = \omega/c$, the surface s is the circle on the plane $z = 0$ of radius a to cover the aperture of the horn.

We can then find the fields using the definitions of the electric and magnetic potentials,

$$\mathbf{E} = \partial_t(\mathbf{A}_s + \mathbf{A}_m \times \hat{\mathbf{r}}/(\epsilon_0 c)) \quad (2.17)$$

$$= -i\omega(\mathbf{A}_s + \mathbf{A}_m \times \hat{\mathbf{r}}/(\epsilon_0 c)). \quad (2.18)$$

From here it is common to make one of many assumptions. All recreate the same fields in the small angle approximation and the choice between the approximations is not obvious given a horn. The most common is to set $\mathbf{J}_s = 0$ and $\mathbf{J}_m = -2\mathbf{z} \times \mathbf{E}(z = 0)$. Under this assumption and by combining equations (2.11,2.16,2.18), we can see that the radiated electric field is related to the Fourier transform of the electric field at the aperture. This leads to us defining \mathbf{f} to be,

$$\mathbf{f}(\theta, \phi) = \int_0^a \int_0^{2\pi} dr' d\phi' \mathbf{E}(r', \phi') e^{ikr' \sin \theta \cos(\phi - \phi')}, \quad (2.19)$$

where a is the size of the aperture. In cases related to astrophysics, horns are placed at the focal plane of a lens or parabolic mirror. This has the effect, assuming the lens or mirror is infinite in size and perfect in shape, of simply making the beam pattern smaller on the sky. This means we can usually take a small angle approximation and find $\mathbf{E}_{\text{far}} = \alpha \mathbf{f}$, where α is a constant.

This approximation is correct to first order in θ , which corresponds to being accurate to $\sim(-80)\text{dB}$ if $\theta \sim 2^\circ$. The complete expression is $\mathbf{E}_{\text{far}}(\theta, \phi) = \mathbf{M}\mathbf{f}(\theta, \phi)$, where

$$\mathbf{M} = \alpha \cos^2(\theta/2) \begin{pmatrix} 1 + t^2 \cos(2\phi) & t^2 \sin(2\phi) \\ t^2 \sin(2\phi) & 1 - t^2 \cos(2\phi) \end{pmatrix},$$

where $t = \tan(\theta/2)$ and we have used Ludwig's third definition of polarisation (Ludwig 1973).

2.2.2 Calculating a beam given a mode

Calculating a beam pattern, in principle, is a simple process. All we have to do is find the electric field at the aperture and Fourier transform the result. The electric field at an aperture located at $z = 0$ is simply

$$\mathbf{E}(r, \phi) = \sum_{i,n,m} a_{inm} \mathbf{E}_{inm}(r, \phi, z = 0), \quad (2.20)$$

where a_{inm} is a complex number describing the phase and amplitude of a mode. The complication occurs in the initial phase of the mode as it couples to the detector is hard to define.

It should be mentioned at this point that while the electric field modes are a complete orthonormal basis within the aperture, they cannot make a general beam pattern, even if we had complete control over the values of a_{inm} . This is easy to see if one considers the required electric field to produce a general beam. A general beam will be created by an electric field which is its Fourier transform. This electric field will, in general, have components which are non-zero outside of the aperture, which is impossible and hence, a general beam is impossible.

As an example of different beams I show the beam patterns generated by the TE₁₁, TM₀₁, TE₂₁, TE₀₁ and TM₁₁, waveguide modes in Figure 2.5 and their electric field at the aperture. I show this combination, in this order, as they are the lowest order modes in order. The beam pattern was calculated numerically by discretising the Fourier transform then using the FFT function in IDL.

2: WAVEGUIDES

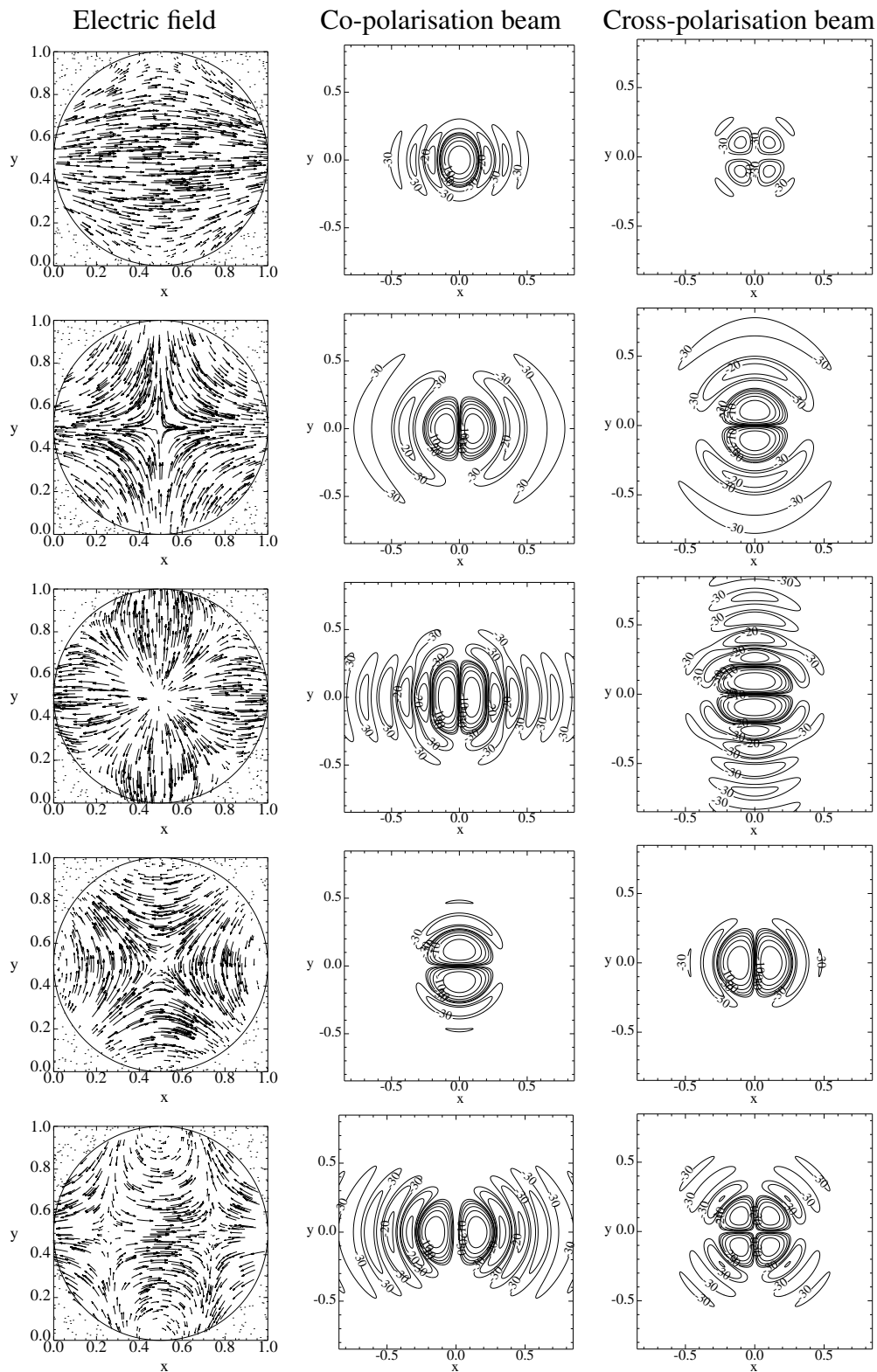


Figure 2.5: The electric field, Co- and Cross-polarisation beam patterns are shown for a range of different waveguide modes. Each row corresponds to a different mode, starting from the top they are: TE₁₁, TM₀₁, TE₂₁, TE₀₁ and TM₁₁. These were chosen as they are the lowest order modes. The axis units are arbitrary.

2.3 Calculating the electric field at the aperture of a horn

We saw in Section 2.2, that considering a horn as an emitter, is an essential step on finding the detection properties of the horn. In this section I review how the electric field at the aperture can be found when using a horn to emit. Modes are set up at the base, then propagated through the horn to the aperture. The amplitude and phase of each of the modes have at the base of the horn depends on the type of detector. In many experiments a bolometer is used: this is essentially a thermometer in thermal equilibrium with the fields in the cavity it exists in. This means the modes present in this cavity couple independently to the detector. As a result there is a time varying phase relationship between two different modes.

2.3.1 Frequency dependence of a mode

In Section 2.2.1 we defined the parameter γ that would act as the wavenumber for the propagation of our mode down the waveguide. For a given mode

$$\gamma_{inm}^2 = \left(\frac{\omega}{c}\right)^2 - K_{inm}^2. \quad (2.21)$$

Therefore, the modes down a waveguide will propagate with different wavenumbers. For a mode where $(\omega/c) < K_{inm}$, γ becomes imaginary and the amplitude decreases exponentially down the waveguide. This causes modes to “switch on” as the frequency increases, i.e. when γ becomes real for a particular mode that mode can then propagate. This “switching on” is a result of the exponential decay with z and the fact that in most horns $\gamma z \gg 1$. A horn’s radius generally increases from the cavity where the bolometer is housed to the opening. Considering the horn to be in emission, we can see that the modes that are allowed to propagate in the cavity will be the only modes that couple the detector to the sky. This limits the number of modes given the

cavity size and the wavelength of the radiation.

2.3.2 Excitation of modes

When a propagating mode reaches a change in the horn shape new modes can be excited. At the junction the electric and magnetic fields must be the same. This leads to new modes being excited across the junction. This process can be described as by scattering matrix, where the vectors are the input and output mode amplitudes of the junction. Two scattering matrices can be combined, however the result is not simply the multiplication. By this method any horn can be modelled and the excited modes evaluated. The modes that are excited are in a fixed phase relationship with the original mode.

Exciting further modes can be used to alter the resulting beam pattern. The primary mode excited in horns are the TE₁₁ mode, the beam pattern of which is shown in Figure 2.5. The TE₁₁ and the TM₁₁, also shown in Figure 2.5 have characteristic four lobed cross-polarisation pattern. By exciting the TM₁₁ mode in a lower amplitude and out of phase with the TE₁₁ mode one can minimise the cross-polar response of the horn.

2.4 Application to multi-moded horns

We can now piece together our knowledge to understand the beam pattern of a multi-moded horn. As shown in equation (2.19) the beam pattern of a horn is related to the Fourier transform of the field at the the aperture. This field can be found using equation (2.20). Due to the linearity of the Fourier transform, in the small angle approximation, we can then say

$$\mathbf{E}_{\text{far}} = \alpha \sum_{i,n,m} a_{inm} \tilde{\mathbf{E}}_{inm}(r, \phi, z = 0), \quad (2.22)$$

where $\tilde{\mathbf{E}}_{inm}$ denotes the Fourier transform of \mathbf{E}_{inm} . This equation looks deceptively simple. The complication, as mentioned before, is related to evaluating the amplitudes a_{inm} . In Section 2.3.1 we discussed the coupling of the modes to a detector. If a bolometer is used then 2 modes will have a time dependent phase relationship. We will now look at the effect this has on the beam pattern.

2.4.1 Combining the effect of two modes to the beam

Consider 2 modes coupling to a bolometer in a horn, \mathbf{E}_1 and $\mathbf{E}_2 e^{i\varphi(t)}$, where $\varphi(t)$ is the time dependent phase difference. Each mode will propagate through the horn and may excite other modes due to the shape of the horn. As discussed in Section 2.3.2 these excited modes have a fixed phase relationship to the original mode. Let us denote the propagated fields as \mathbf{E}'_1 and $\mathbf{E}'_2 e^{i\varphi'(t)}$. These two fields are the result of two different modes coupled to the bolometer in the cavity. They have propagated independently and therefore the phase relationship between two modes is still independent of each other as it was when they were in the cavity. Therefore we can write the far-field has

$$\mathbf{E}_{\text{far}} = \alpha \left(\tilde{\mathbf{E}}'_1 + \tilde{\mathbf{E}}'_2 e^{i\varphi'(t)} \right). \quad (2.23)$$

The intensity, \mathbf{I} , of the beam is therefore,

$$\mathbf{I} = \begin{pmatrix} I_{\text{co}} \\ I_{\text{cross}} \end{pmatrix}, \quad (2.24)$$

$$= (\Re(\mathbf{E}_{\text{far}}))^2. \quad (2.25)$$

The telescope will be point at a particular direction for a time scale t_{int} and $\varphi(t)$ will vary on a time scale $\sim 1/\omega$. For any CMB experiment $t_{\text{int}} \gg 1/\omega$, so the time averaged intensity is sufficient. This causes the cross term to vanish leaving

$$\langle \mathbf{I} \rangle = \langle (\Re(\tilde{\mathbf{E}}'_1))^2 \rangle + \langle (\Re(\tilde{\mathbf{E}}'_2))^2 \rangle. \quad (2.26)$$

This tells us that to calculate the full beam, we must sum the time averaged intensity of each beam pattern of each mode that is coupled to the bolometer.

2.4.2 Normalising the different modes contributions

When summing the intensity of each mode we must understand the amount of total power that each mode transfers. Formally we must know the quantity

$$P_{inm}^{co/cross} = \int_0^\pi \sin \theta d\theta \int_0^{2\pi} d\phi I_{inm}^{co/cross}, \quad (2.27)$$

here the time average is implicit. The total power a mode then transfers is then $P_{tot} = P_{co} + P_{cross}$. It is desirable for P_t to be the same for each mode as it will represent the maximal coupling between the detector and the sky. For that reason when combining the modes we must normalise the mode to have the same total power transfer as every other mode.

We now apply this to knowledge to make a very naive prediction for the beam of a multi-moded horn. We calculate the beam shapes for all modes that can propagate in a cavity with radius $a = \alpha\lambda$, where $\alpha = 0.5, 1.0, 1.5, 2.0$, examples of these modes and their beam shapes in Figure 2.6. We then sum them in quadrature each beam pattern such that each mode couples the same amount of power to the bolometer. I show the co- and cross polarisation responses in Figure 2.6. As the number of modes increases the size of the beam pattern increases, this is due to the small scale structure in the higher order modes electric field pattern. The cross-polarisation also increases as the higher modes are included. For many of the modes the cross-polarisation beam has the same total power as the co-polarisation beam.

2.4: APPLICATION TO MULTI-MODED HORNS

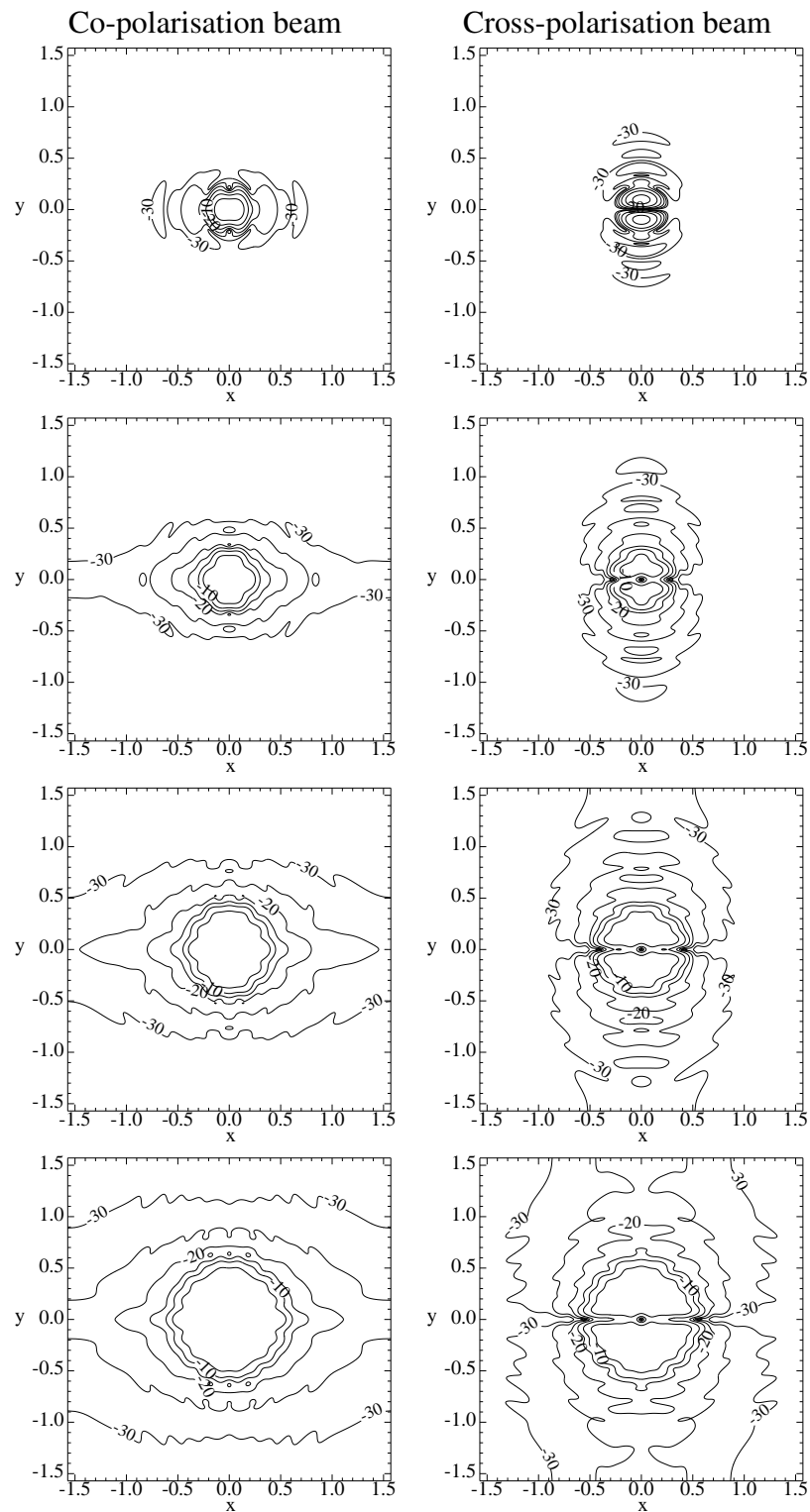


Figure 2.6: The co- and cross-polarisation beam patterns are shown for a range of multi-moded horn beams. Each row corresponds to a different number of modes, 3, 10, 24 and 42 modes respectively. These are the number of modes that would exist if the cavity had a radius of $a = \alpha\lambda$, where $\alpha = 0.5, 1.0, 1.5, 2.0$.

2.4.3 LSPE and multi-moded horns

The Large Scale Polarisation Explorer (LSPE) (LSPE Collaboration et al. 2012) is a future balloon borne CMB B -mode polarisation experiment that will use multi-moded horns. The increased number of waveguide modes coupled to the bolometer will increase the sensitivity of the experiment. However, as shown the shape of the beam may create unwanted systematic errors in the polarisation maps.

The beams shown in Figure 2.6 while they aid our understanding of multi-moded horns do not represent the beam patterns expected for LSPE. The shape of the Winston horn planned to be used will create a much sharper fall off in the beam response. Also a polarising filter will be placed in front of the focal planes, this will, in principle, remove all of the cross-polarisation response. However, with the temperature power spectrum 4 orders of magnitude above the B -mode polarisation power spectrum, any coupling between the two must be controlled and/or removed to a very high degree of accuracy. The next two chapters describe work I have done in an attempt to create algorithms capable of removing these systematic errors.

Chapter 3

Removing beam asymmetry bias in precision CMB temperature and polarisation experiments

Asymmetric beams can create significant bias in estimates of the power spectra from CMB experiments. With the temperature power spectrum many orders of magnitude stronger than the B-mode power spectrum any systematic error that couples the two must be carefully controlled and/or removed. In this chapter, I derive unbiased estimators for the CMB temperature and polarisation power spectra taking into account general beams and general scan strategies. A simple consequence of asymmetric beams is that, even with an ideal scan strategy where every sky pixel is seen at every orientation, there will be residual coupling from temperature power to B-mode power if the orientation of the beam asymmetry is not aligned with the orientation of the co-polarisation. I test my correction algorithm on simulations of two temperature-only experiments and demonstrate that it is unbiased. The simulated experiments use realistic scan strategies, noise levels and highly asymmetric beams. I also develop a map-making algorithm that is capable of removing beam asymmetry bias at the map level. I demonstrate its implementation using simulations and show that it is capable of accurately correcting both

temperature and polarisation maps for all of the effects of beam asymmetry including the effects of temperature to polarisation leakage.

3.1 Introduction

In this chapter, I present two methods to remove the effect of asymmetry bias. The first is an algorithm to recover the CMB power spectra using the pseudo- C_ℓ approach. I make no assumptions about the beam or the scan strategy in developing unbiased estimators for the underlying CMB temperature and polarisation power spectra. I also show that noise can be easily accommodated. The pseudo- C_ℓ estimator that I propose is based on a calculation similar to one presented in Hanson et al. (2010). Here, I extend the analysis to polarisation and demonstrate its implementation on simulated temperature-only experiments. Since the estimator works directly on the time ordered data (TOD), it is sub-optimal for polarization experiments that do not directly measure both Q and U Stokes parameters in the timeline (e.g. via detector differencing). For such experiments, the estimator will perform the decomposition into Q and U at the level of the power spectrum which will contribute to the statistical error. However, this estimator is well suited to an experiment such as *Planck* which has both instrument- Q and instrument- U detector pairs in its focal plane.

In addition to the pseudo- C_ℓ approach, I present a new map-making algorithm that is capable of making temperature and polarisation maps cleaned of asymmetry bias. The map-making algorithm produces maps containing the sky signal smoothed with just the axisymmetric components of the beam and noise. Note that this map-making scheme requires a suitable scan strategy, in general, the more complex the beam asymmetry is, the more redundancy (in terms of polarization angle coverage) is required in the scan strategy. For the asymmetric beams that I have investigated in this chapter, the scan strategy requirements are fully met by scanning modes proposed for future CMB satellite experiments such as those described in Bock et al. (2009).

Removing the asymmetry at the map level has two main benefits. Firstly, in con-

trast to the case of the pseudo- C_ℓ approach, the polarisation power spectrum estimator error bars are not affected by the sample variance of the temperature power spectrum. Secondly, the resulting bias-free temperature and polarisation maps can also be used for science other than power spectrum estimation. Foregrounds can be removed after the map-making has been performed meaning that current component separation techniques can be applied.

The chapter is organized as follows. I begin in Section 3.2 where I present some basic definitions and develop the mathematical formalism on which my algorithms are based. In Section 3.3, I present the pseudo- C_ℓ based approach to correcting for beam asymmetry. Section 3.4 discusses the potential impact of beam asymmetries on CMB polarization experiments, if they are left uncorrected. In Section 3.5, I present a technique to correct for the effects of beam asymmetry in the map domain. Section 3.6 discusses some details of the decomposition of the beam which is required for both of our approaches. I demonstrate my techniques on simulations in Sections 3.7 & 3.8 and my conclusions are presented in Section 3.9.

3.2 Basic definitions and preliminaries

My objective is to construct estimators for the temperature and polarisation fluctuation power spectra given a TOD. I assume that any non-astrophysical signals in the TOD have been flagged and, for the pseudo- C_ℓ approach, that foregrounds have been removed and/or masked. I consider an asymmetric beam and a general scan strategy. I begin by defining some relevant quantities.

The CMB temperature and polarisation fluctuations, $\Delta T(\theta, \phi)$, $Q(\theta, \phi)$ and $U(\theta, \phi)$, can be decomposed into spin-weighted spherical harmonics

$$a_{0\ell m} = \int d\Omega {}_0Y_{\ell m}^*(\Omega) \Delta T(\Omega) \quad \text{and} \quad (3.1)$$

$$a_{\pm 2\ell m} = \int d\Omega {}_{\pm 2}Y_{\ell m}^*(\Omega) [Q(\Omega) \mp iU(\Omega)], \quad (3.2)$$

3: REMOVING BEAM ASYMMETRY BIAS IN CMB EXPERIMENTS

where ${}_sY_{\ell m}$ are the spin weighted spherical harmonics. The temperature, E -mode and B -mode harmonic coefficients are related to these by

$$a_{\ell m}^T = a_{0\ell m}, \quad (3.3)$$

$$a_{\ell m}^E = -\frac{1}{2}(a_{2\ell m} + a_{-2\ell m}), \quad (3.4)$$

$$a_{\ell m}^B = -\frac{1}{2i}(a_{2\ell m} - a_{-2\ell m}). \quad (3.5)$$

I am interested in obtaining unbiased estimates for the power- and cross-spectra of the CMB defined as

$$C_\ell^{XY} = \frac{1}{2\ell + 1} \sum_{m=-\ell}^{\ell} a_{\ell m}^X a_{\ell m}^{Y*}, \quad (3.6)$$

where $X, Y = \{T, E, B\}$.

The response of a telescope to the Stokes parameters on the sky (T, Q, U) can be described by some response (beam) functions $(\tilde{T}, \tilde{Q}, \tilde{U})$. The total detected power is

$$W \propto \int (T\tilde{T} + Q\tilde{Q} + U\tilde{U}) d\Omega. \quad (3.7)$$

For details of how polarised detectors respond to the CMB see Challinor et al. (2000). One element of the TOD is then this power W integrated over the time interval between two samples. I define the spin weighted spherical harmonic transforms of the beam to be

$$b_{0\ell k} = \int d\Omega {}_0Y_{\ell k}^*(\Omega) \tilde{T}(\Omega) \quad \text{and} \quad (3.8)$$

$$b_{\pm 2\ell k} = \int d\Omega {}_{\pm 2}Y_{\ell k}^*(\Omega) [\tilde{Q}(\Omega) \mp i\tilde{U}(\Omega)], \quad (3.9)$$

when the beam is pointing in the z -direction in a fiducial orientation such that the co-polarisation is aligned with the y -direction. Note that this formalism can describe all aspects of a detector's response function. For example, one can include both the

asymmetry of the beam and any cross-polarisation response. This will allow them to remove any bias that these beam imperfections would impart on the estimated power spectra.

I truncate the expansion of both the beam and the sky at some maximum multipole, ℓ_{\max} . I also cap the expansion of the beam in k at some maximum value, k_{\max} . This is a reasonable approximation to make as beam response functions are typically close to axisymmetric. In Section 3.6 I will examine this assumption for some specific cases. The beam is then rotated around the sky in a scan to measure the CMB. I describe this rotation using Euler angles $\omega = [\theta, \phi, \psi]$. This is really three active rotations. They are active as the beam moves with respect to the coordinate system. The following series of steps describe how to rotate the beam from the fiducial orientation to the orientation described by ω , all rotations being performed anticlockwise when looking down the axis by which they are defined.

1. The beam is rotated around the z axis by ψ .
2. The beam is rotated by θ around the y axis.
3. The beam is rotated around the z axis again by ϕ .

The Wigner D-matrix, $D_{mk}^{\ell}(\omega)$, performs the required rotations on the spherical harmonic decomposition of a function. Therefore, I can write one element of the TOD (t_j) as

$$t_j = \sum_{s\ell mk} D_{mk}^{\ell*}(\omega_j) b_{s\ell k}^* a_{s\ell m}. \quad (3.10)$$

For simplicity, in this chapter, I only write the index that is being summed over and not the ranges. For the rest of this chapter one should assume ℓ ranges from 0 to ℓ_{\max} , m from $-\ell$ to ℓ and $s=0, \pm 2$. The index k ranges from $-k_{\max}$ to k_{\max} , unless $\ell < k_{\max}$, in which case the range is the same as for m .

Before we can go further we must define some more mathematical constructs. The first is the ‘‘hit cube’’, $W(\omega) \equiv \sum_j \delta(\omega - \omega_j)$, which describes which sky positions the

3: REMOVING BEAM ASYMMETRY BIAS IN CMB EXPERIMENTS

experiment has observed, and in which orientations. $W(\omega)$ is defined on the space running from 0 to π in θ and from 0 to 2π in both ϕ and ψ . The infinitesimal volume element of this space $d^3\omega = \sin\theta d\theta d\phi d\psi$.

The convolution of the sky with the beam $t(\omega)$ is a continuous function which one will only have limited knowledge of. The knowledge one has is dictated by the scan strategy, or in this formalism the hit cube. Formally we have

$$t(\omega) = \sum_{s\ell mk} D_{mk}^{\ell*}(\omega) b_{s\ell k}^* a_{s\ell m}, \quad (3.11)$$

$$\tilde{t}(\omega) = W(\omega)t(\omega). \quad (3.12)$$

$\tilde{t}(\omega)$ is a function which contains all of the astrophysical information present in the experiment. It is simply a rewriting of the TOD, where each element is described by a δ -function at the relevant orientation ω .

The Wigner D-matrices provide a complete orthogonal basis for this space, so we use them to decompose both the TOD and the hit cube as

$$T_{mk}^{\ell*} = \int d^3\omega D_{mk}^{\ell}(\omega) \tilde{t}(\omega) n(\omega) \quad \text{and} \quad (3.13)$$

$$w_{mk}^{\ell} = \frac{2\ell + 1}{8\pi^2} \int d^3\omega D_{mk}^{\ell*}(\omega) W(\omega) n(\omega). \quad (3.14)$$

Here, I have introduced the weighting function $n(\omega)$, which ranges from 0 to 1. I use this function to down-weight noisy pixels, apply a foreground mask and/or apodise the hit cube so that it can be described well within our expansion. I use the prefactor in equation (3.14) to correctly normalise the coefficients so that I can write

$$W(\omega)n(\omega) = \sum_{\ell mk} w_{mk}^{\ell} D_{mk}^{\ell}(\omega). \quad (3.15)$$

For this reconstruction of the hit cube to be exact, one would require k to range from $-\ell$ to ℓ , not as I have here from $-k_{\max}$ to k_{\max} . This is not a problem for our proposed techniques since, as we shall see later, we only need to capture the features in the ψ

direction with Fourier modes up to some k_{\max} , the value of which is determined by the complexity of the beam asymmetry. This is analogous to the axisymmetric case, where to recover the temperature fluctuation power spectrum the analysis uses the hit map, which is just the $k=0$ Fourier mode of the hit cube. So while we cannot fully recover the complete hit cube I do recover its important features.

3.3 Beam asymmetry correction within the pseudo- C_ℓ framework

In this section, I develop a technique to correct for the effects of beam asymmetry within the framework of pseudo- C_ℓ power spectrum estimators (Hivon et al. 2002; Brown et al. 2005). As described earlier, this approach to correcting for beam asymmetries is well suited to experiments that can measure the Q and U Stokes parameters simultaneously in the timestream (e.g. differencing experiments). In Appendix A.1 I show that for such an experiment the pseudo- C_ℓ presented here is similar to that of the standard pseudo- C_ℓ approach (Brown et al. 2005).

3.3.1 Definition of the pseudo- C_ℓ spectra

I wish to define a two-point statistic that contains the relevant information from the TOD and which can also be related to the power spectra defined in equation (3.6) via a coupling matrix. As the quantity T_{mk}^ℓ contains all of the information present in the TOD, it must therefore contain all of the information required to recover the CMB spectra. I define the pseudo- C_ℓ spectra as

$$\tilde{C}_\ell^{kk'} \equiv \sum_m T_{mk}^{\ell*} T_{mk'}^\ell, \quad (3.16)$$

which can be computed directly from the TOD. The appropriateness of this choice becomes clear when we write the Wigner D-matrices in terms of the spin weighted spherical harmonics (Goldberg et al. 1967):

$$D_{mk}^\ell(\theta, \phi, \psi) = \sqrt{\frac{4\pi}{2\ell + 1}} e^{ik\psi} {}_{-k}Y_{\ell m}(\theta, \phi). \quad (3.17)$$

We see that T_{m0}^ℓ will be similar to the $a_{0\ell m}$ coefficients of a binned map made from the TOD while $T_{m,\pm 2}^\ell$ will be similar to the $a_{\pm 2\ell m}$ coefficients. This is due to the fact that the Wigner D-matrices are decomposing the 3D space, ω , with basis functions over the θ and ϕ dimensions which are the spin weighted spherical harmonics.

3.3.2 Calculating the coupling operator

Here I aim to find an analytic expression for the $\tilde{C}_\ell^{kk'}$ defined in equation (3.16) in terms of the true sky spectra and a coupling matrix that depends only on the scan strategy and the beam. I begin by re-writing the decomposition of the TOD using equation (3.10) and the definition of the window function. I do this to replace the sum over j with an integral,

$$\begin{aligned} T_{m_1 k_1}^{\ell_1*} &= \sum_j D_{m_1 k_1}^{\ell_1}(\omega_j) t_j n(\omega_j) \\ &= \int d^3\omega D_{m_1 k_1}^{\ell_1}(\omega) t(\omega) n(\omega) W(\omega) \\ &= \sum_{j s_2 \ell_2 m_2 k_2} D_{m_1 k_1}^{\ell_1}(\omega_j) D_{m_2 k_2}^{\ell_2*}(\omega_j) b_{s_2 \ell_2 k_2}^* a_{s_2 \ell_2 m_2} n(\omega_j). \end{aligned}$$

Using the definition of the hit cube $W(\omega) = \sum_j \delta(\omega - \omega_j)$ I deduce that

$$T_{m_1 k_1}^{\ell_1*} = \sum_{s_2 \ell_2 m_2 k_2} b_{s_2 \ell_2 k_2}^* a_{s_2 \ell_2 m_2} K_{m_1 k_1 m_2 k_2}^{\ell_1 \ell_2}, \quad (3.18)$$

3.3: BEAM ASYMMETRY CORRECTION WITHIN THE PSEUDO- C_ℓ FRAMEWORK

where in the last line I have introduced the coupling kernel,

$$K_{m_1 k_1 m_2 k_2}^{\ell_1 \ell_2} \equiv \int d^3\omega D_{m_1 k_1}^{\ell_1}(\omega) D_{m_2 k_2}^{\ell_2*}(\omega) W(\omega) n(\omega). \quad (3.19)$$

I am now in a position to calculate the coupling operator. I start from the definition of $\tilde{C}_\ell^{k_1 k'_1}$,

$$\begin{aligned} \tilde{C}_{\ell_1}^{k_1 k'_1} &\equiv \sum_{m_1} T_{m_1 k_1}^{\ell_1*} T_{m_1 k'_1}^{\ell_1} \\ &= \sum_{\substack{m_1 \\ s_2 \ell_2 m_2 k_2 \\ s_3 \ell_3 m_3 k_3}} b_{s_2 \ell_2 k_2}^* a_{s_2 \ell_2 m_2} K_{m_1 k_1 m_2 k_2}^{\ell_1 \ell_2} b_{s_3 \ell_3 k_3} a_{s_3 \ell_3 m_3}^* K_{m_1 k'_1 m_3 k_3}^{\ell_1 \ell_3*}. \end{aligned} \quad (3.20)$$

If I now assume that the CMB temperature and polarization fluctuations are Gaussian distributed with isotropic variance, then we can write $\langle a_{s\ell m} a_{s'\ell' m'}^* \rangle = C_\ell^{ss'} \delta_{\ell\ell'} \delta_{mm'}$ where I have defined

$$C_\ell^{ss'} = \frac{1}{2\ell + 1} \sum_m a_{s\ell m} a_{s'\ell m}^*. \quad (3.21)$$

This assumption does not produce a bias in my estimator, but simply increases the statistical error. Using this result, equation (3.20) simplifies to

$$\begin{aligned} \langle \tilde{C}_{\ell_1}^{k_1 k'_1} \rangle &= \sum_{\substack{m_1 \\ s_2 \ell_2 m_2 k_2 \\ s_3 \ell_3 k_3}} b_{s_2 \ell_2 k_2}^* K_{m_1 k_1 m_2 k_2}^{\ell_1 \ell_2} b_{s_3 \ell_2 k_3} K_{m_1 k'_1 m_2 k_3}^{\ell_1 \ell_2*} \langle C_{\ell_2}^{s_2 s_3} \rangle \\ &= \sum_{\substack{s_2 \ell_2 k_2 \\ s_3 \ell_3 k_3}} b_{s_2 \ell_2 k_2}^* b_{s_3 \ell_2 k_3} M_{k_1 k'_1 k_2 k_3}^{\ell_1 \ell_2} \langle C_{\ell_2}^{s_2 s_3} \rangle, \end{aligned} \quad (3.22)$$

where, in the second step, I have used the product of two coupling kernels, $M_{k_1 k'_1 k_2 k_3}^{\ell_1 \ell_2}$, derived in Appendix A.2. I can now identify the coupling operator that describes the contribution of each sky spectrum $C_\ell^{s_1 s_2}$ to each of the $\tilde{C}_\ell^{k k'}$, i.e. I can write

$$\langle \tilde{C}_{\ell_1}^{k_1 k'_1} \rangle = \sum_{\ell_2 s_2 s_3} O_{\ell_1 \ell_2}^{k_1 k'_1 s_1 s_2} \langle C_{\ell_2}^{s_2 s_3} \rangle, \quad (3.23)$$

where,

$$O_{\ell_1 \ell_2}^{k_1 k'_1 s_1 s_2} = \sum_{k_2 k_3} b_{s_2 \ell_2 k_2}^* b_{s_3 \ell_2 k_3} M_{k_1 k'_1 k_2 k_3}^{\ell_1 \ell_2}. \quad (3.24)$$

Certain symmetries can be used to reduce the number of M matrices required to evaluate equation (3.24). These symmetries, which are derived in Appendix A.3, are

$$M_{k_1 k'_1 k_2 k_3}^{\ell_1 \ell_2} = M_{k'_1 k_1 k_3 k_2}^{\ell_1 \ell_2*}, \quad (3.25)$$

$$M_{k_1 k'_1 k_2 k_3}^{\ell_1 \ell_2} = (-1)^{k_2 - k_1 + k_3 - k'_1} M_{-k_1 - k'_1 - k_2 - k_3}^{\ell_1 \ell_2*}. \quad (3.26)$$

3.3.3 Recovering the true CMB spectra

I am now in a position to obtain unbiased estimators for the true CMB power spectra C_ℓ^{XY} defined in equation (3.6). I start by defining a large vector made up of the pseudo- C_ℓ spectra, $\tilde{C}_\ell^{kk'}$, and another comprised of the true full-sky spin spectra, $C_\ell^{ss'}$ defined in equation (3.21):

$$\mathbf{C}_i = (C_\ell^{00}, C_\ell^{02}, C_\ell^{0-2}, C_\ell^{22}, C_\ell^{2-2}, C_\ell^{-2-2})^T \quad (3.27)$$

$$\tilde{\mathbf{C}}_i = (\tilde{C}_\ell^{00}, \tilde{C}_\ell^{02}, \tilde{C}_\ell^{0-2}, \tilde{C}_\ell^{22}, \tilde{C}_\ell^{2-2}, \tilde{C}_\ell^{-2-2})^T. \quad (3.28)$$

Each of these are vectors of length $6(\ell_{\max} + 1)$. Using these definitions I can write our overall coupling matrix equation as

$$\tilde{\mathbf{C}}_{i_1} = \sum_{i_2} \mathbf{O}_{i_1 i_2} \mathbf{C}_{i_2}. \quad (3.29)$$

I write the overall coupling operator $\mathbf{O}_{i_1 i_2}$ explicitly in terms of the individual O -matrices of equation (3.24) in Appendix A.4. Once this operator has been calculated, equation (3.29) can be inverted to recover the true spin spectra $C_\ell^{ss'}$, properly deconvolved for both the mask and the asymmetric beam. A further simple transformation, which is explicitly written down in Appendix A.5, yields the final estimates of the six

3.3: BEAM ASYMMETRY CORRECTION WITHIN THE PSEUDO- C_ℓ FRAMEWORK

possible CMB power spectra, C_ℓ^{XY} . Note that, as with normal pseudo- C_ℓ estimators, in the presence of a severe sky cut, the matrix, $O_{i_1 i_2}$ will be singular and must therefore be binned before it can be inverted. This is standard practice with pseudo- C_ℓ power spectrum estimators (Hivon et al. 2002; Brown et al. 2005).

3.3.4 Including noise

Any useful algorithm for removing the effects of beam asymmetry must also be able to deal with instrumental noise. Since my algorithm works within the framework of the standard pseudo- C_ℓ technique, I can use exactly the same approach to remove the noise bias as is adopted in the standard analysis (Hivon et al. 2002). A TOD element including noise can be written as

$$t_j = \sum_{slmk} D_{mk}^{\ell*}(\omega_j) b_{slk}^* a_{slm} + n_j. \quad (3.30)$$

If I assume that the noise is not correlated with the pointing direction of the telescope then

$$(\tilde{C}_\ell^{kk'})^{\text{SN}} = (\tilde{C}_\ell^{kk'})^{\text{S}} + N_\ell^{kk'}, \quad (3.31)$$

where the SN and S superscripts denote the signal-plus-noise and the signal-only pseudo- C_ℓ spectra respectively. An unbiased estimate of the noise power spectra, $N_\ell^{kk'}$, can be obtained by performing a set of simulations containing only instrument noise and calculating $\tilde{C}_\ell^{kk'}$ for each as before using equation (3.16). The noise bias is then estimated as the average over the set of noise realisations, $N_\ell^{kk'} = \langle C_\ell^{kk'} \rangle$. The final estimator for the full-sky, noise-debiased and asymmetry-cleaned spin power spectra can then be written as

$$\mathbf{C}_{i_1} = \sum_{i_2} \mathbf{O}_{i_1 i_2}^{-1} (\tilde{\mathbf{C}}_{i_2} - \langle \mathbf{N}_{i_2} \rangle), \quad (3.32)$$

where $\langle \mathbf{N}_{i_2} \rangle$ is a vector of length $6(\ell_{\max} + 1)$ comprised of all of the individual noise bias spectra, constructed in an analogous fashion to equations (3.27) and (3.28). As before, the six CMB power spectra are then recovered trivially using the relation in Appendix A.5.

3.4 Impact of beam asymmetries on CMB polarization experiments

With the analysis of the previous two sections in place, I can now examine the effect that beam asymmetries will have on the E - and B -mode polarization power spectra. I begin by noting again that the $T_{m\pm 2}^\ell$ of equation (3.13) are closely related to the spin-2 harmonic coefficients $a_{\pm 2\ell m}$ of Q and U maps constructed from the same TOD. In analogy with equations (3.4) and (3.5), I can therefore define the following E -mode-like and B -mode-like linear combinations and two-point correlations of the $T_{m\pm 2}^\ell$:

$$T_{mE}^\ell \equiv -\frac{1}{2} (T_{m2}^\ell + T_{m-2}^\ell) \quad (3.33)$$

$$T_{mB}^\ell \equiv -\frac{1}{2i} (T_{m2}^\ell - T_{m-2}^\ell) \quad \text{and} \quad (3.34)$$

$$\implies \tilde{C}_\ell^{EE} = \frac{1}{4} (\tilde{C}_\ell^{22} + \tilde{C}_\ell^{-2-2} + \tilde{C}_\ell^{-22} + \tilde{C}_\ell^{2-2}) \quad (3.35)$$

$$\implies \tilde{C}_\ell^{BB} = -\frac{1}{4} (\tilde{C}_\ell^{22} + \tilde{C}_\ell^{-2-2} - \tilde{C}_\ell^{-22} - \tilde{C}_\ell^{2-2}) \quad (3.36)$$

In Appendix A.1, I show that the quantities defined in equations (3.33) and (3.34) are similar to the standard pseudo- C_ℓ E - and B -modes defined in Brown et al. (2005). These relations can then be used to investigate the impact of beam asymmetries and/or a non-zero cross-polar beam response function.

Of particular concern is the potential coupling between the temperature power spectrum and the B -mode polarization power spectrum. As the temperature power spectrum is known to be at least four orders of magnitude stronger than the B -mode power, any coupling between the two could be catastrophic if not properly accounted

3.4: IMPACT OF BEAM ASYMMETRIES ON CMB POLARIZATION EXPERIMENTS

for. Here I show how the most prominent asymmetric modes of the beam can potentially create such a coupling.

As described in Section 3.6 (see Figs. 3.1 and 3.2), the $k = \pm 2$ mode is by far the most prominent asymmetric term for the representative beams that I consider later in this paper. To examine the impact of the $k = \pm 2$ asymmetry, I consider a situation where all possible orientations are observed, i.e. where $W(\omega)n(\omega)=1$. In this case, the contribution to $T_{m\pm 2}^{\ell*}$ from the temperature fluctuations is

$$\begin{aligned} T_{m\pm 2}^{\ell*} &= \sum_{\ell' m' k'} b_{0\ell' k'}^* a_{0\ell' m'} \int \mathbf{d}^3\omega D_{m\pm 2}^{\ell}(\omega) D_{m' k'}^{\ell'*}(\omega) \\ &= \frac{8\pi^2}{2\ell + 1} b_{0\ell\pm 2}^* a_{0\ell m}, \end{aligned} \quad (3.37)$$

where I have used the orthogonality of the Wigner D-matrices (Goldberg et al. 1967). Equation (3.37) shows that the asymmetry will couple temperature to polarization even in the case of an ideal scan strategy. This was to be expected, since both the CMB polarisation field and the convolution of the temperature fluctuations with the $k = \pm 2$ term of the beam are spin- ± 2 quantities. From equations (3.33) and (3.34), the effect on the measured the E - and B -mode polarisation is

$$\Delta T_{mE}^{\ell} = -\frac{4\pi^2}{2\ell + 1} (b_{0\ell 2} + b_{0\ell -2}) a_{0\ell m}^* \quad \text{and} \quad (3.38)$$

$$\Delta T_{mB}^{\ell} = -\frac{4\pi^2}{i(2\ell + 1)} (b_{0\ell 2} - b_{0\ell -2}) a_{0\ell m}^*. \quad (3.39)$$

For the coupling from temperature to B -mode polarisation to be non-zero in this case, then $b_{0\ell\pm 2}$ must be complex. This will only be the case if the beam asymmetry is orientated at an angle to the polarization sensitivity direction defined by the co-polar response, which will not be the case in general.

O'Dea et al. (2007) studied the systematic error induced when an elliptical Gaussian beam is used in a B -mode experiment. They considered a specific type of ellipticity: one where the beam is either perturbed along the direction of the polarisation, or

perpendicular to it. This type of perturbation has the unique property of having a decomposition where $b_{0\ell\pm 2}$ is real, and they therefore concluded that such an asymmetry cannot couple temperature fluctuations to B -mode fluctuations, something the authors recognise and note in the paper. I have shown here that, if the beam is perturbed in any other way than this special case, then temperature fluctuations will be coupled to B -mode fluctuations even in the case of an ideal scan strategy. This result is in agreement with the findings of Shimon et al. (2008) who also considered the coupling between temperature and B -mode polarisation due to beam asymmetry effects.

3.5 Beam asymmetry correction during map-making

In some cases, the approach to correcting for beam asymmetry presented in Section 3.3 will be sub-optimal. For example, in the case where one corrects for significant temperature-to-polarization leakage, there will be a contribution to the error-bars on the reconstructed polarization power spectra due to the sample variance associated with the leaked temperature signal. In addition, for polarization experiments that do not measure Q and U simultaneously in the time-stream, the B -mode power spectrum errors will be affected by the sample variance associated with the much larger E -mode polarisation. A technique that corrects for beam asymmetry at the map level will be immune to these issues and is therefore an attractive prospect. Here, I develop such a method to correct for beam asymmetry effects during the map-making step.

I begin by recalling that the convolution of the sky signal with a general beam is given by equation (3.11). In an experiment a telescope will scan the sky, giving us a set of measurements of this function $t(\omega)$. For each pixel on the sky one will therefore have a set of measurements at various orientations.

3.5.1 Extracting the temperature and polarisation of a pixel

This discussion is concerned with estimating the temperature and polarisation signal at the position of a single sky pixel. The detected signal at the position of a pixel S will depend on the instrument orientation at the time of observation ψ due to the polarisation of the sky and the beam asymmetry. If the beam was axisymmetric and had no polarised response then $S(\psi)$ would be constant and equal to the beam-smoothed CMB temperature at the pixel location. This can be seen from equation (3.11) by setting $b_{s\ell k} = b_{0\ell 0} \delta_{k0} \delta_{s0}$ and noticing that the ψ dependence of $t(\omega)$ comes from the Wigner D matrices. For a polarised detector $S(\psi)$ would then contain $k = \pm 2$ Fourier modes, due to the spin-2 nature of polarisation. This property is exploited by map-making algorithms to find the temperature and polarisation of a pixel. In these algorithms the ψ dependence of the detected signal is assumed to be due to the polarisation signal. Here, I relax this assumption and develop a map-making algorithm that provides estimates of the temperature and polarisation of a pixel that are free of systematics of different spins.

I represent the orientations at which a pixel is seen in an experiment by defining a window function $h(\psi) \equiv \frac{1}{n_{\text{hits}}} \sum_j \delta(\psi - \psi_j)$, where n_{hits} is the number of hits on the pixel. $h(\psi)$ will be different for each pixel and will be dependant on the scan strategy. The detected signal $S^d(\psi)$ is therefore

$$S^d(\psi) = h(\psi)S(\psi). \quad (3.40)$$

In Fourier space¹ this multiplication takes the form of a convolution

$$\tilde{S}_k^d = \sum_{k'=-\infty}^{\infty} H_{kk'} \tilde{S}_{k'}, \quad (3.41)$$

where I have defined $H_{kk'} \equiv \tilde{h}_{k-k'}$. Therefore, if one can invert the matrix $H_{kk'}$ then

¹I define the Fourier transform of $f(\psi)$ and the inverse transform to be $\tilde{f}_k = \frac{1}{2\pi} \int_0^{2\pi} d\psi e^{-ik\psi} f(\psi)$ and $f(\psi) = \sum_{k=-\infty}^{\infty} e^{ik\psi} \tilde{f}_k$.

3: REMOVING BEAM ASYMMETRY BIAS IN CMB EXPERIMENTS

one can recover the true \tilde{S}_k . Recovering the spin-0 and spin-2 features of $S(\psi)$ is the main goal of this section since these are the CMB temperature and polarisation of the pixel. Therefore, I would like to obtain estimates for \tilde{S}_0 and $\tilde{S}_{\pm 2}$.

Inverting the matrix $H_{kk'}$ as it is written in equation (3.41) would be impossible: firstly it is infinitely large, and secondly for any realistic $h(\psi)$ the matrix will be singular.² However, if I make the assumption that \tilde{S}_k cuts off at a small value of k_{\max} and if the ψ angle coverage of that pixel is sufficient such that this reduced matrix is invertible then I can use the approximation,

$$\tilde{S}_k = \sum_{k'=-k_{\max}}^{k_{\max}} H_{kk'}^{-1} \tilde{S}_{k'}^d. \quad (3.42)$$

One can choose k_{\max} by measuring the azimuthal dependence of the beam and ensuring that they have include enough k -modes to capture all of the Fourier modes in $S(\psi)$. As in the case of the pseudo- C_ℓ approach (Section 3.3), the k_{\max} should chosen so that the asymmetry of the beam is fully captured. I return to this issue in the following section where I examine the harmonic decomposition of some representative asymmetric beams.

Adopting the HEALPIX³ definition of the Stokes parameters, one can calculate the temperature and polarisation of the pixel from the inverse Fourier transform of the estimated \tilde{S}_k as

$$T = \tilde{S}_0, \quad (3.43)$$

$$Q = 2\Re(\tilde{S}_2), \quad (3.44)$$

$$U = 2\Im(\tilde{S}_2). \quad (3.45)$$

Performing this procedure for all observed pixels, one will then have estimates of the T, Q and U maps which are free of systematics that have a different spin to the desired

²Note that “realistic” in this context explicitly excludes the case of an ideal scan strategy for which $h(\psi)=1$.

³See <http://healpix.sourceforge.net>

quantity.

3.5.2 Removing the leakage from temperature to polarisation

I showed in Section 3.4 that the asymmetry of the beam will leak temperature fluctuations to polarisation regardless of the scan strategy. This is due to the spin-2 dependence of the temperature of the CMB convolved with the $k = \pm 2$ mode of the beam response function. The polarisation maps made using the map-making method described above will still contain this spin-2 leakage from temperature to polarisation. However, since I know that this leakage is from the temperature fluctuations coupling to the $k = \pm 2$ asymmetry in the beam, and since I also now have an unbiased estimate of the temperature map, we can therefore calculate and remove this leakage.

I start from the estimated temperature map. If one has observed only part of the sky it is necessary to apodise the map such that there are no features due to the mask that are smaller than the beam scale. I then take the spherical harmonic transform of this map, $\tilde{T}(\Omega)$

$$\tilde{a}_{0\ell m} = \int d\Omega {}_0Y_{\ell m}^*(\Omega) \tilde{T}(\Omega). \quad (3.46)$$

We can now calculate the polarization leakage using equations (3.38) and (3.39). One can show that the spherical harmonic transform of the temperature leakage is given by

$$\Delta a_{\ell m}^E = 2\Re \left(\frac{b_{0\ell 2}}{b_{0\ell 0}} \right) \tilde{a}_{0\ell m}, \quad (3.47)$$

$$\Delta a_{\ell m}^B = 2i\Im \left(\frac{b_{0\ell 2}}{b_{0\ell 0}} \right) \tilde{a}_{0\ell m}. \quad (3.48)$$

Upon transforming back to real space, these terms can then be removed from the polarisation maps. Note that the regions within a beam-scale of the locations where the temperature map was apodised should be disregarded as the leakage will not have been removed in these regions.

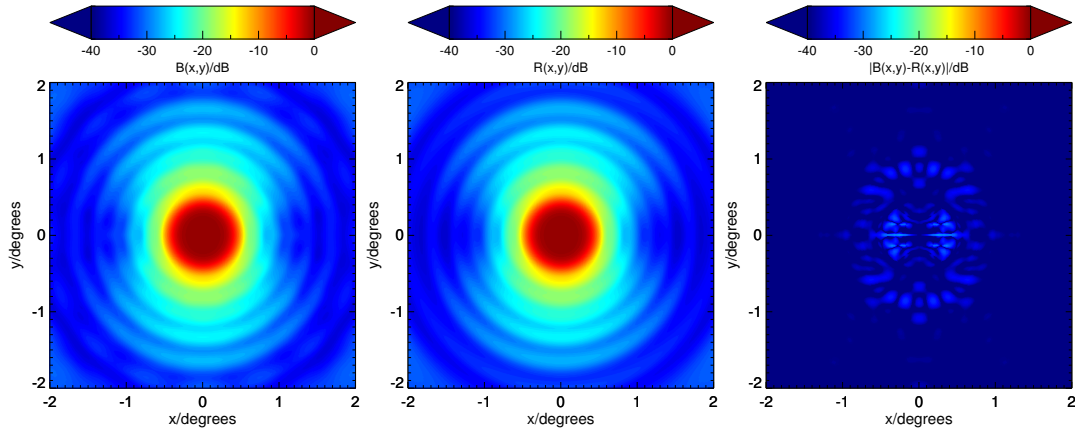


Figure 3.1: *Left panel:* The simulated beam of a 17 moded horn planned to be on board the LSPE balloon experiment. *Centre panel:* the reconstruction of the beam only retaining 2 modes ($k_{\max}=2$). *Right panel:* The absolute error between the simulated beam and the reconstruction.

3.6 Evaluating the parameter k_{\max} for a temperature only experiment

Both the pseudo- C_ℓ technique and the map-making approach for removing beam asymmetries requires a cap on the harmonic expansion of the beam, k_{\max} . I will now look at a realistic set up for a CMB experiment in order to ascertain how large the required k_{\max} is likely to be for real experiments. I make no assumption on the scan strategy. However, beam shapes are generally designed to be as axisymmetric as possible. I expect therefore that the beam expansion can be truncated after only a few terms with minimal loss of accuracy. Note that the pseudo- C_ℓ correction technique can in principle be applied for any k_{\max} that is deemed necessary in order to achieve the required accuracy. This will come with the obvious computational cost of increasing the number of summations required to evaluate equation (3.24). In contrast, for the map-making approach, there will be some maximum value of k_{\max} for which the matrix $H_{kk'}$ of equation (3.42) will be invertible. Also note that increasing k_{\max} will increase the statistical error on the recovered map. It should therefore be chosen to be only as large as is required by the asymmetry in the beam. In practice, whether the map-

making approach will be appropriate for any given experiment will depend on both the complexity of the beam asymmetry and on the polarization angle coverage of the experiment.

3.6.1 Beam decompositions for some representative cases

As a demonstration of how a realistic and asymmetric beam can be represented using just a few k -modes, I consider a numerical simulation of an instrumental beam corresponding to the multi-moded 145 GHz feed horns planned to be flown on-board the balloon-borne Large Scale Polarisation Explorer (LSPE, LSPE Collaboration et al. 2012). By coupling 17 wave-guide modes, the sensitivity of a single LSPE horn + detector module is greatly increased. However, the large number of propagated modes results in a complicated and potentially asymmetric overall beam shape. Note that the numerical simulation used here is of the horn only and a simple scaling of the overall beam size has been applied to roughly approximate the effect of the telescope lens.

Note that the LSPE experiment will also include a half-wave plate (HWP) in front of the optics which will be used to increase the polarization angle coverage of the experiment. However, for the purposes of this demonstration, I consider a temperature-only experiment and I therefore ignore the effect of the HWP.

Upon performing the spin-0 decomposition of the beam, (equation 3.8), I find that only a few azimuthal modes are required to accurately model what might be considered a rather asymmetric beam. Fig. 3.1 shows the original simulated beam alongside a representation of it retaining only the two most significant modes ($k = 0$ and $k = \pm 2$) of the decomposition. The major features of the beam asymmetry are clearly well captured using this heavily truncated expansion. I therefore choose to set $k_{\max}=2$. The beams shown here are invariant when rotated by π , therefore the odd azimuthal terms will be zero. Explicitly the truncated decomposition of the beam can be written as (now writing $b_{0\ell k} = b_{\ell k}$ etc. for clarity)

$$b_{\ell k} = b_{\ell 0}\delta_{k0} + b_{\ell+2}\delta_{k,+2} + b_{\ell-2}\delta_{k,-2}. \quad (3.49)$$

3: REMOVING BEAM ASYMMETRY BIAS IN CMB EXPERIMENTS

In Fig. 3.1 I also show the residuals between the full beam and this representation which is seen to be a good approximation. We can immediately see from equation (3.22) that this will greatly simplify the pseudo- C_ℓ coupling matrix calculation by limiting the sum over k_2 and k_3 to only include the $k_2, k_3=0, \pm 2$ modes.

Also, I examine a general elliptical Gaussian beam described by

$$B(\theta, \phi) = \frac{1}{2\pi q\sigma^2} e^{-\frac{\theta^2}{2\sigma^2}(\cos^2 \phi + q^{-1} \sin^2 \phi)}, \quad (3.50)$$

where q is a parameter that defines the asymmetry of the beam and the full width at half maximum (FWHM) $\theta_{\text{FWHM}} = 2.35\sigma$. If $q=1$ then the beam is axisymmetric. To test the expansion we choose $\theta_{\text{FWHM}}=7$ arcmin and $q=1.5$, which represents a highly elliptical beam, significantly more elliptical than one might expect in a real CMB experiment. This simulated beam therefore provides a stringent test of our correction algorithms. I plot the spin-0 decomposition of this beam in Fig. 3.2. It is encouraging to see that once again, we can describe the beam asymmetry using a relatively small number of terms.

3.6.2 Using the noise power to set k_{max} in a temperature only experiment

From the above demonstration, it appears that only a small number of terms in the harmonic expansion of the beam need to be retained in order to capture the global features of the beam response including the effects of asymmetry.

However, to be truly confident that the truncated expansion is an accurate enough representation of the beam, one would ideally choose the value of k_{max} such that the any residual error from mis-representing the beam is smaller (to some tolerance level) than the statistical error in an experiment. For a particular asymmetric expansion term the leading order contribution to \tilde{C}_ℓ^{00} is $\sim |\tilde{b}_{0\ell k}|^2 C_\ell^{00}$, where $\tilde{b}_{0\ell k} = b_{0\ell k} \sqrt{\frac{4\pi}{2\ell+1}}$. Therefore

3.6: EVALUATING THE PARAMETER k_{\max} FOR A TEMPERATURE ONLY EXPERIMENT

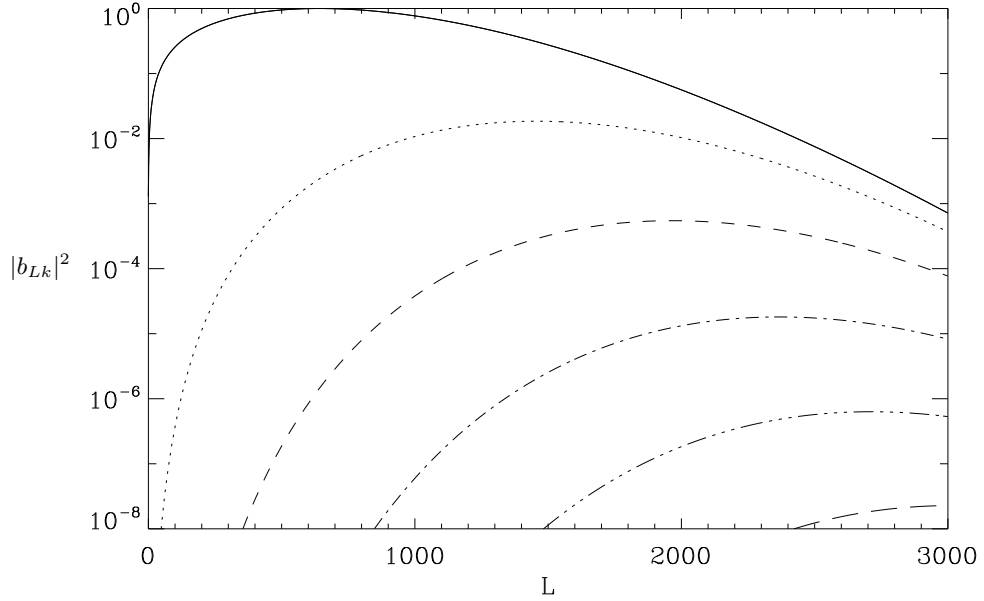


Figure 3.2: The amplitudes of the $k=0, 2, 4, 6, 8, 10$ terms of the beam expansion, $|b_{\ell k}|^2$, as a function of multipole, ℓ for an elliptical Gaussian beam as defined in equation (5.29) with $\sigma=3$ arcmin corresponding to a $\theta_{\text{FWHM}}=7$ arcmin and ellipticity parameter, $q=1.5$.

one can say that the asymmetric term should be included if

$$\langle p_k \rangle_{\text{pix}} |\tilde{b}_{0\ell k}|^2 C_\ell^{00} > f \langle N_\ell^{00} \rangle_\sigma, \quad (3.51)$$

where f is a tolerance level to which we require our systematic errors to be below the statistical error. A reasonable choice may be $f=0.1/\sqrt{\ell_{\text{range}}}$, to ensure that the systematic error is 10% of the noise statistical error, where ℓ_{range} is the range of ℓ the mode is sensitive to. $\langle N_\ell^{00} \rangle_\sigma$ is the standard deviation of the noise power which is the dominating source of statistical error at high ℓ . The term $\langle p_k \rangle_{\text{pix}}$ is the k^{th} mode of the ψ angle coverage quality of the scan strategy defined as

$$\langle p_k \rangle_{\text{pix}} = \left\langle \frac{1}{n_{\text{hits}}^2} \left| \sum_i e^{ik\psi_i} \right|^2 \right\rangle_{\text{pix}}, \quad (3.52)$$

where $\langle \rangle_{\text{pix}}$ denotes an average over all pixels on the sky, n_{hits} is the number of hits a pixel receives and the sum over the index i is over all observations of a particular

pixel. The lower the value of $\langle p_k \rangle_{\text{pix}}$, the better the scan strategy is at removing the bias created by the beam asymmetry due to the k^{th} azimuthal mode.

The rule of thumb in equation (3.51) becomes problematic when the sky coverage is small and in the presence of a highly asymmetric beam due to coupling between asymmetric terms of different k . This coupling is suppressed in the all-sky case because the cross spectra $\mathcal{W}_{k_2 k_3}^\ell$ are small for $k_2 \neq k_3$, which in turn means the coupling matrix $M_{00 k_2 k_3}^{\ell_1 \ell_2}$ is small.

However in the case where the power in the hit cube, see Section 3.2, extends to high ℓ these cross spectra terms can become significant. This results in a significant contribution to the operator by a term of the form $b_{0\ell_2 k_2}^* b_{0\ell_2 k_3} M_{00 k_2 k_3}^{\ell_1 \ell_2}$, where $k_2 \neq k_3$. This additional contribution could potentially be larger than the $k_2 = k_3$ term if $|b_{0\ell k_2}| \gg |b_{0\ell k_3}|$.

3.7 Testing the pseudo- C_ℓ on Simulations

In this section, I demonstrate the implementation of the pseudo- C_ℓ technique developed in Section 3.3 on numerical simulations of two representative types of CMB experiment – a generic balloon-borne experiment and a future satellite mission. Note that I test the performance of the algorithm in the temperature-only case. For a temperature-only analysis, the coupling is reduced to

$$\tilde{C}_{\ell_1}^{00} = \sum_{\ell_2} O_{\ell_1 \ell_2}^{0000} C_{\ell_2}^{00} \quad \text{with,} \quad (3.53)$$

$$O_{\ell_1 \ell_2}^{0000} = \sum_{k_2 k_3} b_{0\ell_2 k_2}^* b_{0\ell_2 k_3} M_{00 k_2 k_3}^{\ell_1 \ell_2} \quad (3.54)$$

The main stages of the simulation pipeline are as follows:

1. I use the HEALPIX package to create simulations of the CMB temperature field based on the theoretical CMB power spectrum for the concordance Λ CDM cosmological model.

2. I then create a TOD by convolving the CMB with the telescope beam in the appropriate orientation given the scan strategy.
3. I then calculate the \tilde{C}_ℓ^{00} using equation (3.16).
4. The coupling operator is calculated using the expression in equation (3.54).
5. With the operator $O_{\ell_1 \ell_2}^{0000}$ calculated, I then invert it to recover an estimate of the full-sky and beam-deconvolved power spectrum.

Note that I use two different convolution codes for the two classes of experiment that we simulate. For the balloon-like test I calculate each element of the TOD using equation (3.10). The HEALPIX ROTATE_ALMS routine operates on the beam multipole coefficients. This function uses the Wigner D-matrices to rotate the beam coefficients by a set of Euler angles given on input. The TOD element can then be calculated using,

$$t_j = \sum_{lm} b_{lm}^{j*} a_{lm}, \quad (3.55)$$

where b_{lm}^{j*} is the multipole expansion of the beam when it has been rotated through the Euler angles ω_j . In this way the whole TOD can be created. While this is accurate and simple it would be impossible to use this approach in the satellite-like experiment as the number of TOD elements and the required ℓ_{\max} would make it computationally infeasible. To create the simulated TOD in the satellite-like case, I use a method similar to the FEBECOP approach (Mitra et al. 2011) except that I do not calculate the effective beams but rather I produce the individual TOD elements. The convolution is simplified by describing the beam in pixel space and we only calculate the value of the beam on a set of neighbouring pixels centred around the pointing centre of the beam. I use pixels within $5\sigma q$ of the centre of the beam (see equation 5.29) to describe the beam over this localised region of sky.

A second technical challenge was to obtain the Wigner D-matrix transforms of the TOD and the window function. I achieved this by implementing equations (3.13)

and (3.14) using the expression for the Wigner D-matrix in terms of spin weighted spherical harmonics (equation 3.17). First, the integral over ψ was performed using a simple Newton-Cotes numerical integration method. The HEALPIX routine MAP2ALM_SPIN was then used to perform the integrals over θ and ϕ .

3.7.1 Balloon-like test

For our first test I use the simulated LSPE beam shown in Fig. 3.1 with a modification. I amplify the size of the asymmetry by a factor of a hundred in order to produce a more stringent test of the asymmetry correction algorithm. The spherical harmonic decomposition of this exaggerated beam is related to the original LSPE decomposition by

$$b_{0\ell,k}^{\text{exagg}} = b_{0\ell,0}^{\text{LSPE}} \delta_{k0} + b_{0\ell,\pm 2}^{\text{LSPE}} \delta_{k\pm 2} \times 100. \quad (3.56)$$

I use the planned scan strategy for LSPE but I stress that I have not included the effects of the half-wave plate (HWP) that LSPE will use. The LSPE experiment will incorporate a HWP in front of the optics which will be used to increase the polarization angle coverage of the experiment. However, for the purposes of this demonstration where I consider a temperature-only experiment, I have ignored the (advantageous) effects of the HWP.

I created a set of TOD following the above procedure including white noise. The LSPE scan strategy covers $\sim 25\%$ of the sky and so provides a test of the algorithm's ability to account for a cut sky in addition to the effects of beam asymmetry. Fig. 3.3 shows an example of a simple binned map created from one of our simulations. This figure also shows the hit map of the scan strategy, the 2nd ψ coverage quality p_2 defined in Section 3.6.2 and the weighting function that we use to apodise the hit map. I include an (unrealistically high) noise level of 1.6 mK-arcmin in our simulations in order to test the removal of noise bias from the recovered power spectrum.

The \tilde{C}_ℓ^{00} for 1000 realisations were computed according to equation (3.53) and the

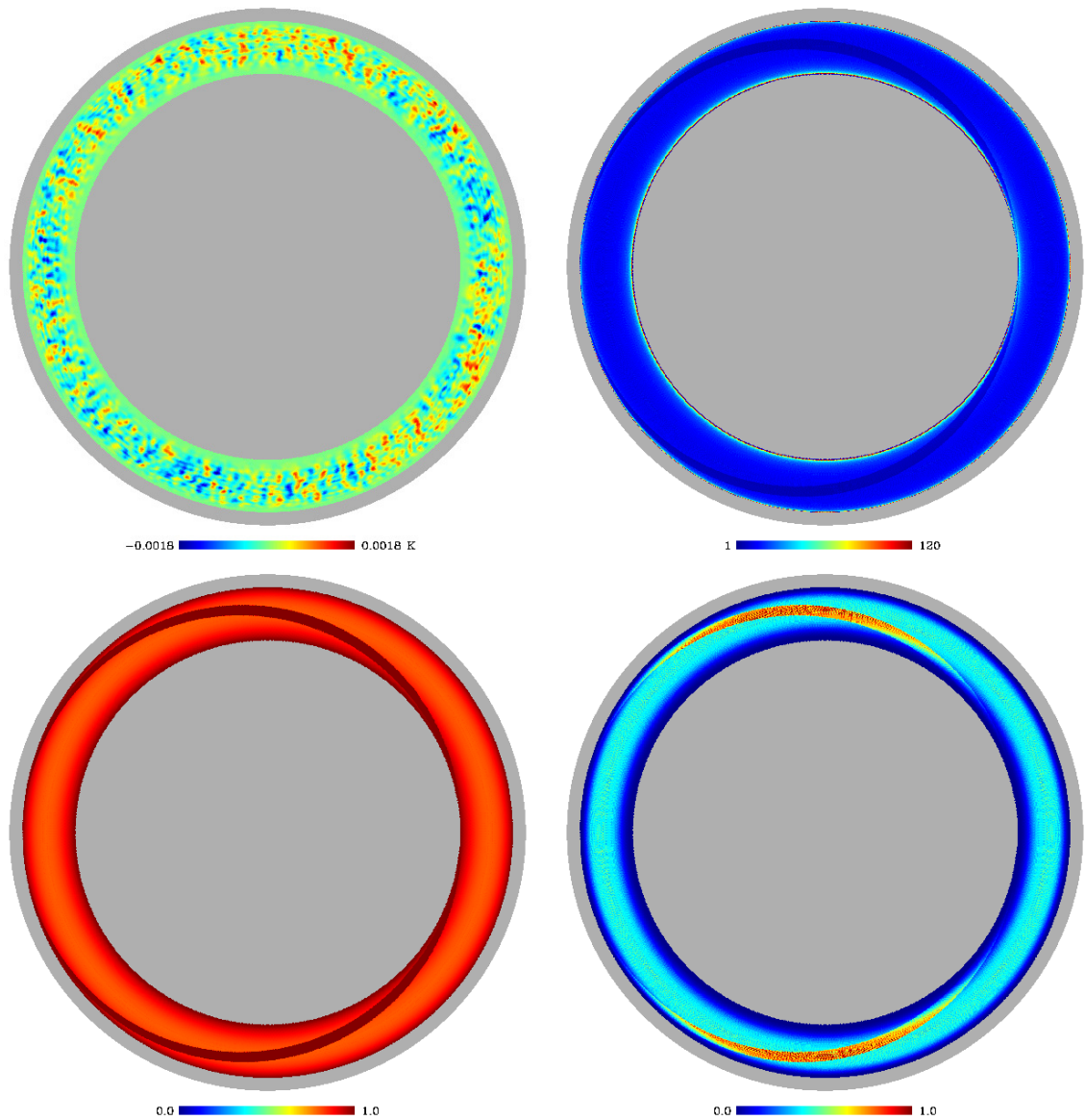


Figure 3.3: *Top left*: An example binned map made in the balloon-like test. The exaggerated beam was used with a spherical harmonic decomposition as described in equation (3.56). The scan strategy implemented is typical of a balloon based experiment. *Top right*: The hit map from one day of observations for the balloon-like experiment. *Bottom left*: The p_2 quality, defined in equation (3.52), of the scan strategy. Note that a HWP was not included which is why the polarization angle coverage is poor for this simulation. *Bottom right*: The weighting function applied to apodise the hit map.

3: REMOVING BEAM ASYMMETRY BIAS IN CMB EXPERIMENTS

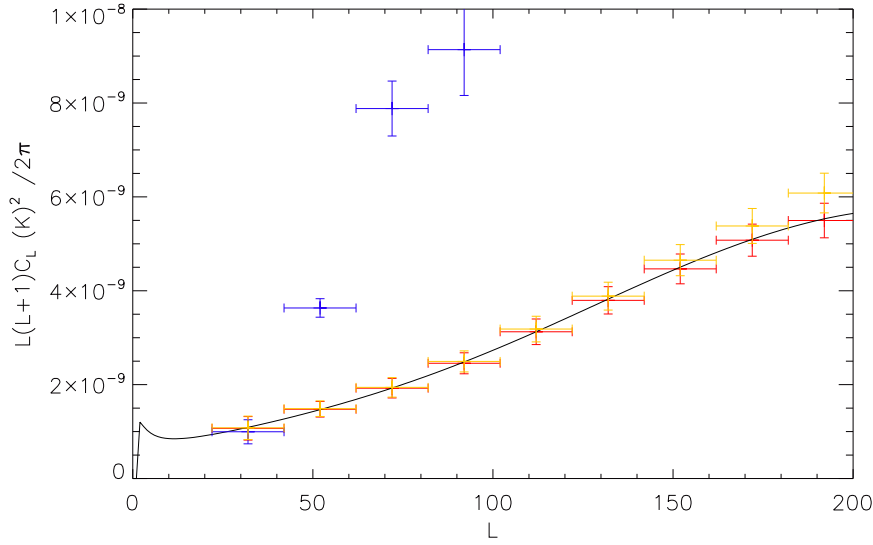


Figure 3.4: Reconstruction of the power spectrum for the balloon-like simulation using the pseudo- C_ℓ method. The input theoretical power spectrum is plotted (black) along with the recovered power spectrum when the exaggerated beam is used (red), averaged over 1000 realisations. I also plot the recovered power spectrum one would recover if the axisymmetric MASTER (Hivon et al. 2002) analysis was used (blue) and if the noise was ignored (yellow). The vertical error bars show the standard deviation of the realisations from the mean.

coupling operator was calculated using equation (3.54). In order to invert the coupling matrix I needed to bin the \tilde{C}_ℓ^{00} and the coupling operator, as in Hivon et al. (2002). This binning ensures that the matrix is invertible and that the resulting data points are uncorrelated. Here we use a bin size of $\Delta\ell=20$. A correction for noise bias was also implemented following the procedure outlined in Section 3.3.4. Fig. 3.4 shows the mean power spectrum recovered from the simulations in comparison to the input spectrum. In this figure, I also plot the mean power spectrum recovered when the beam was assumed to be axisymmetric, by including only the $b_{0\ell 0}$ term on the pseudo- C_ℓ . This figure clearly demonstrates that our algorithm can successfully recover the power spectrum in a situation where the axisymmetric approximation clearly fails. The power spectrum obtained in the case where the noise in the TOD was ignored is also shown demonstrating the ability of our algorithm to successfully correct for noise bias.

3.7.2 Satellite-like experiment

The second test that I perform uses a satellite-like scan strategy. For this test, I use a beam described by equation (5.29) with $\sigma=3$ arcmin corresponding to a FWHM of 7 arcmin and $q=1.5$. The scan strategy used is similar to that proposed for the Experimental Probe of Inflationary Cosmology (EPIC, Bock et al. 2009). In Fig. 3.5 I show the hit map, the p_2 quality (equation 3.52) and the weighting function that I have used to mask the galaxy and extragalactic sources. I use the same mask as was used by the *Planck* collaboration (Planck Collaboration et al. 2014c) for their power spectrum analysis. The weighting function also apodises the hit map. Note that the EPIC scan strategy was designed to improve the 2nd ψ coverage quality defined in Section 3.6.2. This choice of scan strategy will therefore be effective in mitigating beam asymmetries even in the absence of a dedicated correction algorithm. I therefore expect the bias, in the absence of a dedicated correction, to be much smaller than seen in the previous section (although it will still be non-zero). The mean recovered power spectra using $k_{\max}=0, 2$ are shown in the top panel of Fig. 3.6. The lower panel of this figure shows the fractional residual bias in the power spectrum recovery and demonstrates an unbiased result to high- ℓ when $k_{\max}=2$ is used. These simulations included white noise such that the error on the map is equivalent to $8.5 \mu\text{K}\cdot\text{arcmin}$. One can see that even with a scan strategy designed to optimise crossing angles and thereby reduce the asymmetry bias, there remains a bias at the level of $\sim 1-2\sigma$ when the axisymmetric approximation is made.

The importance of this test is two-fold. It demonstrates that the algorithm can deal with a more conventional elliptical Gaussian beam and also that it can be extended to high- ℓ . The coupling operator was calculated in 9 hrs on one 2.26 GHz processor to $\ell_{\max} = 4000$. We calculated the coupling operator to a much higher ℓ than the maximum multipole of interest (2000) to ensure that we did not miss any effects from the aliasing of power from higher multipoles.

3: REMOVING BEAM ASYMMETRY BIAS IN CMB EXPERIMENTS

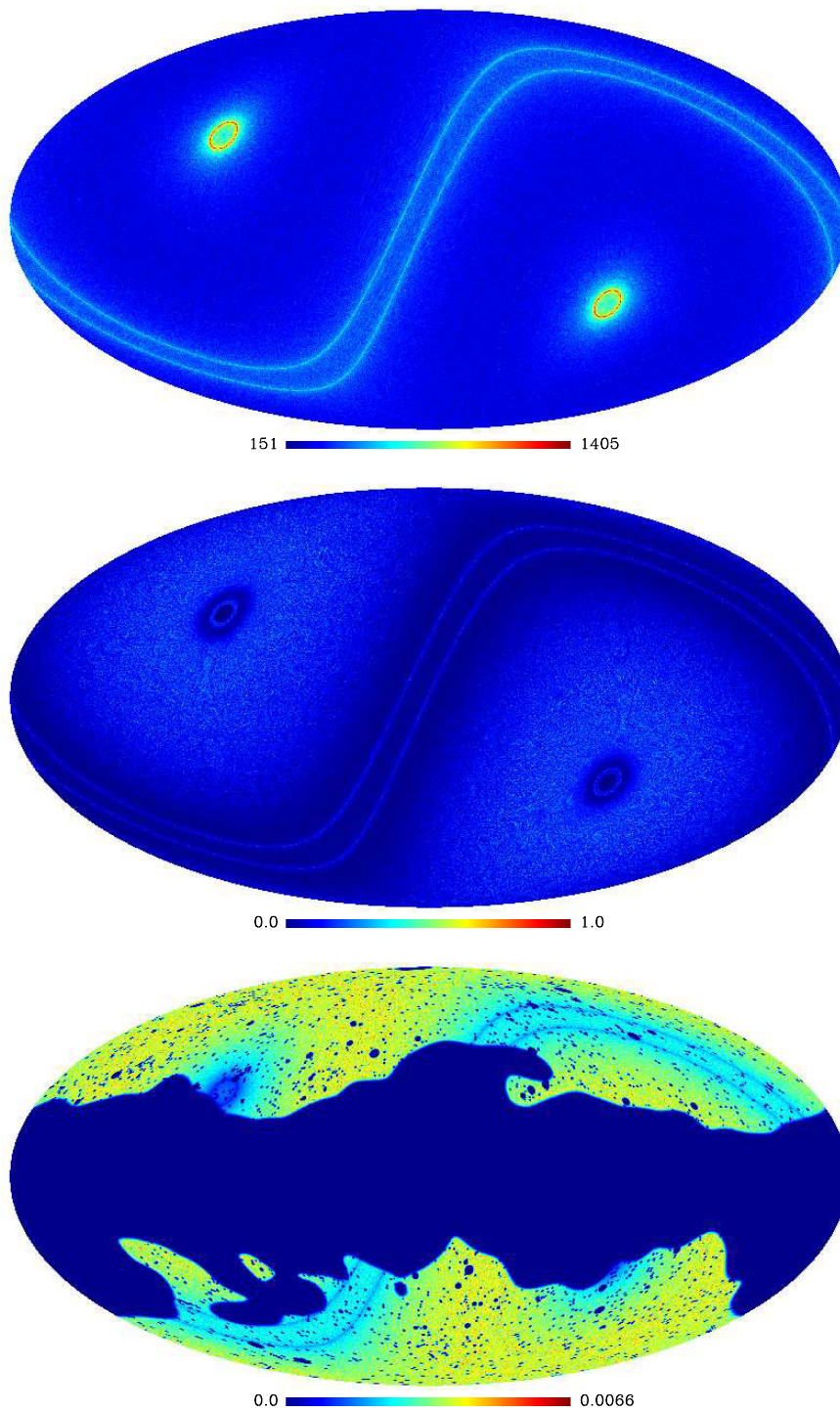


Figure 3.5: *Top panel:* The hit map for one year of observations for our simulated satellite-like experiment. *Middle:* The p_2 quality, defined in equation (3.52), of the scan strategy. *Bottom panel:* The weighting function used to apply a galactic and point source mask and apodise the hit map.

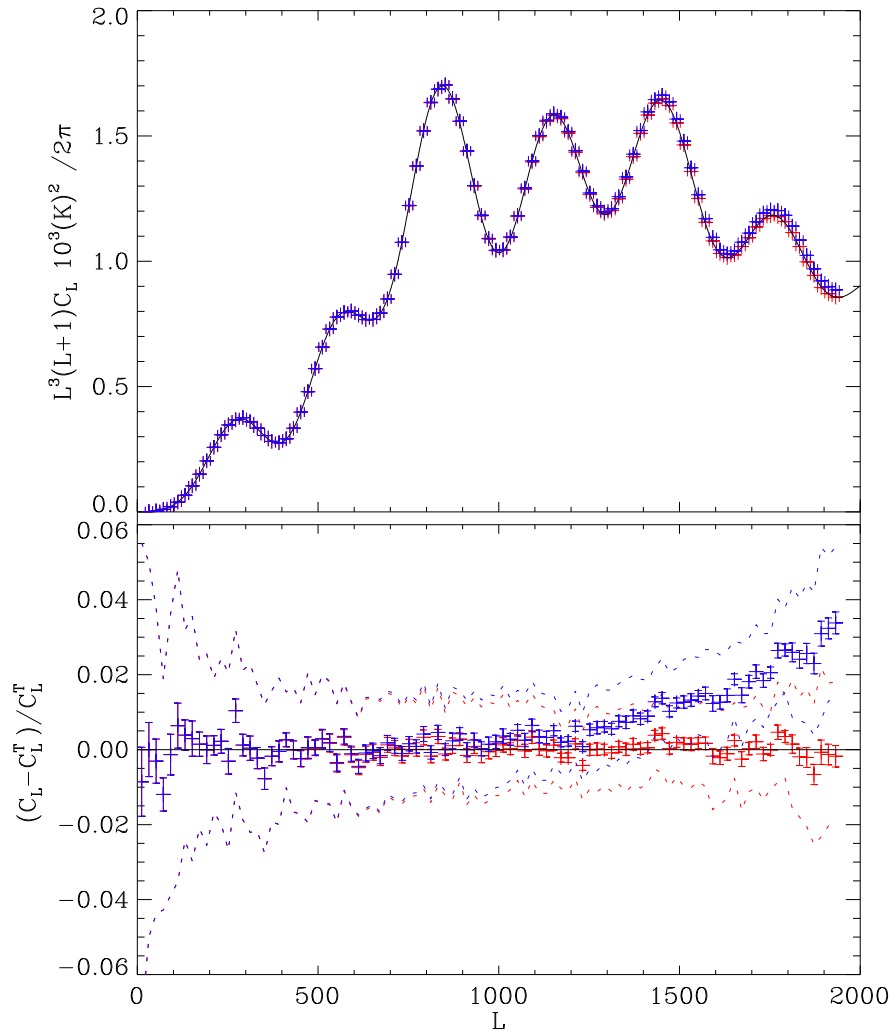


Figure 3.6: Reconstruction of the power spectrum for the satellite-like simulation using the pseudo- C_ℓ method. *Top*: The input theoretical power spectrum is plotted (black) along with the recovered power spectrum for $k_{\max}=0, 2$ (blue and red points respectively) averaged over 48 realisations. *Bottom*: The fractional error between the recovered band powers and the binned input power spectrum. The error bars show the statistical error on the recovered mean, while the dashed lines show the 1σ error that would be seen in a real experiment. One can see that the $k_{\max}=2$ recovery is unbiased to a small fraction of the statistical error caused by noise.

3.8 Testing the map-making algorithm on Simulations

I test the map-making algorithm described in Section 3.5 in two ways. First, I use the algorithm on multiple realisations of the same simulated experiment as described in Section 3.7.2 to show that the algorithm can correctly remove the asymmetry bias on the temperature power spectrum. The second test is performed on a single noise-free full sky simulation of the satellite experiment. I use this latter simulation to test if the algorithm can successfully remove the asymmetry bias directly from the temperature and polarisation maps. I do not include a CMB polarisation signal in our TOD and so a successful asymmetry correction algorithm should recover a zero polarisation signal.

3.8.1 Removing the asymmetry bias on the temperature power spectrum

As in Section 3.7.2, I create 48 TOD realisations using the satellite-like scan strategy, and using an elliptical Gaussian beam with $\theta_{\text{FWHM}}=7$ arcmin and $q=1.5$ (see equation 5.29). As before, the TOD included white noise equivalent to a map noise level of $8.5 \mu\text{K arcmin}$.

From the simulated TOD, I then compute both a simple binned map and a map constructed using the algorithm presented in Section 3.5 with $k_{\text{max}}=2$. I then apply the same galactic and point source mask to these maps as used in Section 3.7.2. A standard pseudo- C_ℓ analysis (Hivon et al. 2002) is then applied in order to recover the power spectrum. Fig. 3.7 shows the recovered power spectrum for the binned map and for the asymmetry cleaned map obtained using the new map-making algorithm of Section 3.5. The asymmetry bias has clearly been removed successfully. Note that the removal of the asymmetry bias comes at the cost of a modest inflation of the power spectrum error-bars which have increased by $\sim 20\%$. This increased error is modest compared to the systematic bias that has been removed.

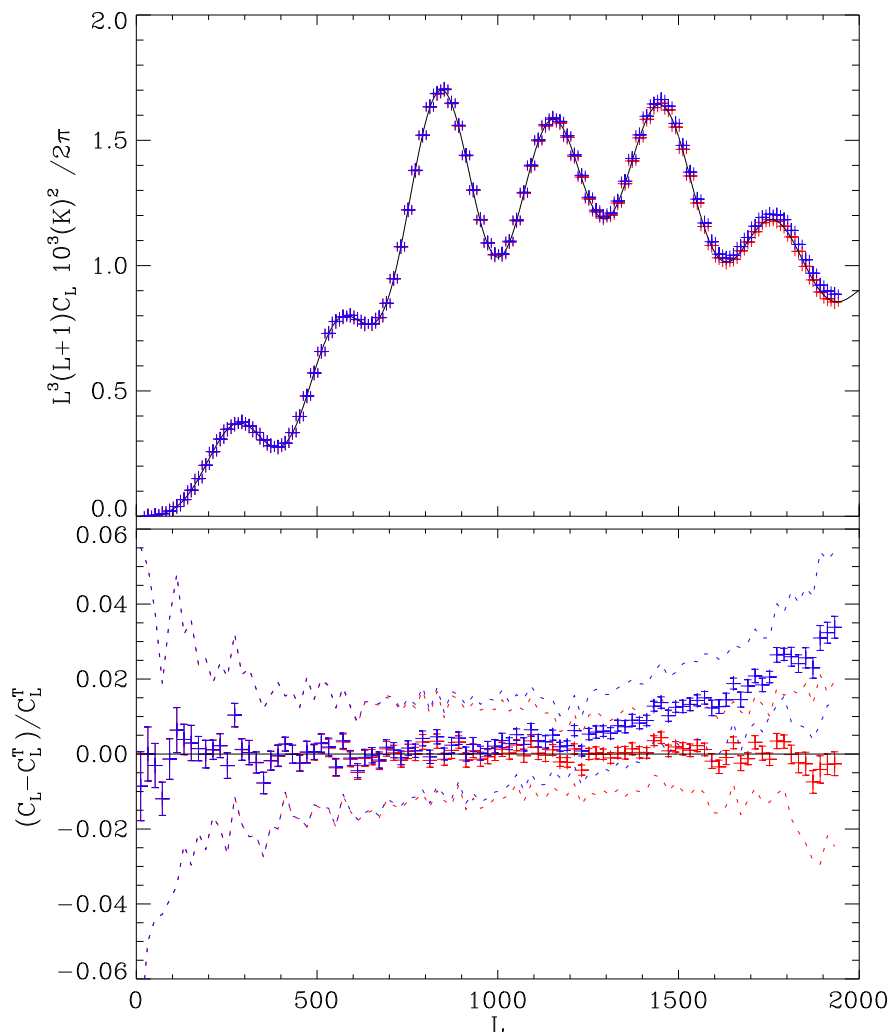


Figure 3.7: Reconstruction of the power spectrum for the satellite-like simulation using the map-making method. This should be compared to Fig. 3.6 which presents the results of the pseudo- C_ℓ method. *Top*: The input theoretical power spectrum is plotted (black) along with the recovered bandpowers for the binned map (blue points), and where the map-making algorithm is used with $k_{\max}=2$ (red points), averaged over 48 realisations. *Bottom*: The fractional error between the recover bandpowers and the binned input power spectrum. The error bars show the statistical error on the recovered mean, while the dashed lines show the 1σ error that would be achieved by a single experiment. One can see that the map-making technique using $k_{\max}=2$ produces power spectrum estimates that are unbiased to a small fraction of the statistical error caused by noise.

3.8.2 Removing the asymmetry bias on the temperature and polarisation maps

Here I present a demonstration of how the map-making algorithm can be used to remove the asymmetry bias on both the temperature and polarisation maps.

To estimate the temperature map, the algorithm of Section 3.5 extracts only the spin-0 components of the TOD. This quantity contains the temperature of the CMB smoothed with the axisymmetric component of the beam. To demonstrate this I simulate a noise free TOD using the elliptical Gaussian and the satellite-like scan strategy. I plot the CMB used in the simulation smoothed with the axisymmetric component of the beam in the top panel of Fig. 3.8. The other three panels in this figure show the absolute error between this isotropically smoothed map and a simple binned map (second panel); and between the isotropically smoothed map and maps produced using the map-making algorithm with $k_{\max}=2$ and $k_{\max}=4$ (lower two panels). The reduction in the bias due to beam asymmetry as k_{\max} is increased is clearly demonstrated by this figure.

I also tested the ability of the map-making algorithm to remove the leakage from temperature to polarisation due to the asymmetry of the beam. I performed this test using the approach described in Section 3.5.2 which makes use of a previously estimated temperature map obtained with the method described in Section 3.5.1 with $k_{\max}=4$. In my simulation I have not included an input polarisation signal so the expected power in the polarisation maps will be zero in the absence of systematics. As described in Section 3.4, the temperature to polarization leakage could contaminate either the E -mode or the B -mode power spectrum depending on the relative orientation between the beam ellipticity and the polarisation response of the detector.

In Fig. 3.9 I plot the power of the leaked temperature to polarisation signal and the power in the polarization maps after this leakage has been removed using the approach described in Section 3.5.2. The power in the cleaned polarisation map has been successfully reduced by ~ 4 orders of magnitude compared to the uncleaned map.

3.8: TESTING THE MAP-MAKING ALGORITHM ON SIMULATIONS

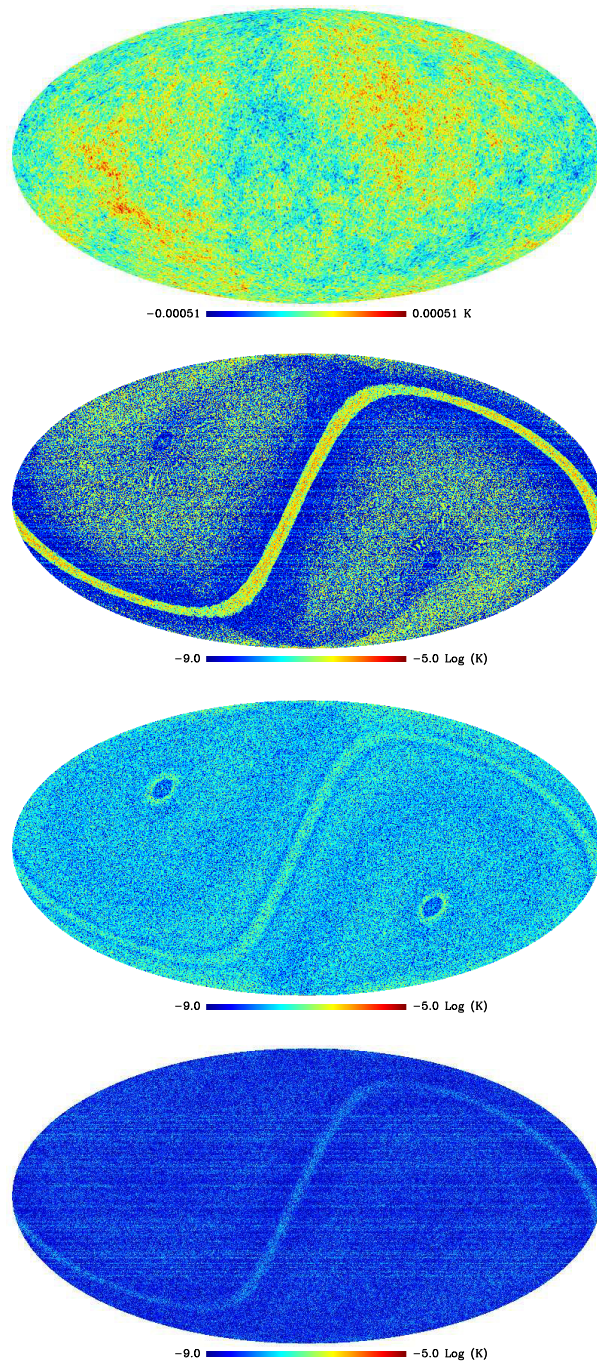


Figure 3.8: *Top panel:* The input CMB realization directly convolved with the axisymmetric component of the elliptical Gaussian beam used for the satellite-like simulation. *Second panel:* The absolute residuals between the isotropically smoothed map shown in the top panel and the simple binned map constructed from the simulated TOD. *Lower two panels:* The absolute residuals between the isotropically smoothed map shown in the top panel and maps made using the algorithm described in Section 3.5 with $k_{\max}=2$ and $k_{\max}=4$. The residuals in the $k_{\max}=4$ case (*bottom panel*) are comparable with the numerical noise of our convolution code.

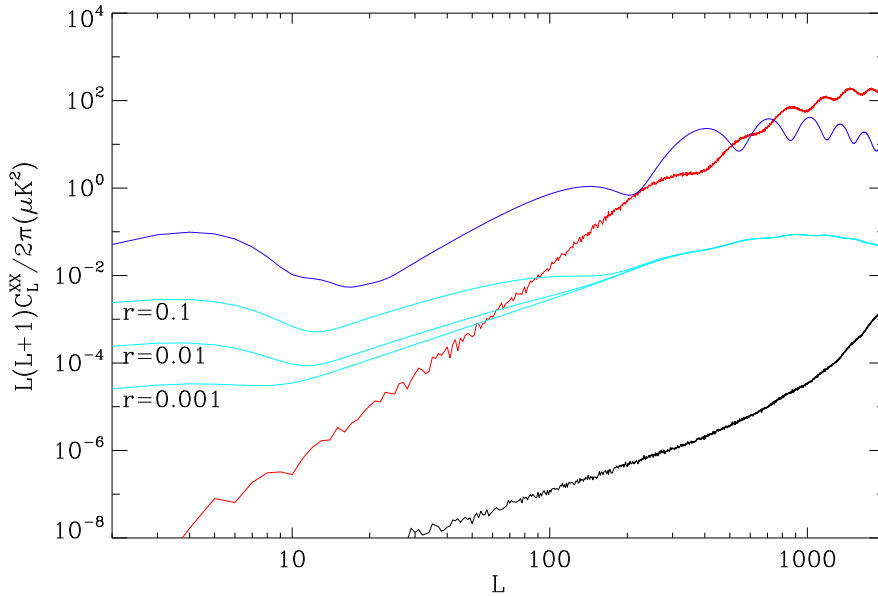


Figure 3.9: The power spectrum of the temperature signal leaked to polarization as a result of beam asymmetries for the simulated satellite-like experiment (red). This power could manifest itself as either an E -mode, a B -mode or a combination of both – see the discussion in Section 3.4. The black line shows the power spectrum of the polarisation leakage after applying the correction algorithm described in Section 3.5.2. For comparison I plot the expected E -mode and B -mode signal in dark and light blue respectively. The expected B -mode signal is plotted for three cases of the tensor-to-scalar ratio: $r=0.001, 0.01, 0.1$.

3.9 Discussion

I have developed two separate techniques to remove asymmetry bias in CMB experiments. The first is a pseudo- C_ℓ method that corrects for the asymmetry bias on the temperature and polarisation power spectra. There is no assumption on the scan strategy and only a modest approximation to the beam is required. The analysis is similar to the MASTER algorithm (Hivon et al. 2002) and its extension to polarisation (Brown et al. 2005). However I include additional contributions to the coupling operator that corrects for the contaminating effects of the beam asymmetry. Note that this algorithm can only be applied to experiments that can directly measure the Q and U Stokes parameters in the timeline, e.g. a differencing experiment with both instrument- Q and instrument- U detectors on its focal plane. This is due to the fact that it makes no at-

tempt to make a map and so it must have measurements of the Stokes parameters in the telescope's frame of reference. At present the formalism assumes the four beams required for such a differencing experiment are the same. A simple extension can relax this assumption.

Using this formalism I also examined the inter-spectra coupling resulting from the beam asymmetry. As an example, I investigated the coupling between temperature and B-mode power in the presence of an ideal scan strategy. In doing so I showed that the temperature power will be coupled to the B-mode power if the beam asymmetry is at an angle to the polarisation sensitivity direction of the detector. This result is in agreement with previous work (Shimon et al. 2008).

The coupling operator in equation (3.24) allows one to calculate the contribution to each pseudo- C_ℓ from the sky power, due to both the mask and beam asymmetry. By inverting this operator one can, therefore, calculate an unbiased estimate for the CMB power spectra. To calculate the operator $\mathbf{O}_{i_1 i_2}$ one must cap the azimuthal dependence of the beam, $k_{\max} \lesssim 10$. I demonstrated in Section 3.6, and in Figs. 3.1 and 3.2, that a simulated beam from a multi-moded horn, and an elliptical Gaussian, equation (5.29), are both well described by only a few azimuthal modes. This property allows one to remove to a high degree of accuracy the bias due to the beam asymmetry for any given scan strategy.

I then went on to implement this algorithm in the temperature only case for two simulated experimental set-ups: a balloon-like experiment and a satellite-like experiment. I showed that I could successfully recover the input power spectrum, when the TOD was created using a highly asymmetric beam in the presence of both a severe sky-cut and instrument noise. These tests showed that the algorithm can deal comfortably with beams that have much higher levels of asymmetry than that typically found in real CMB experiments, and using two completely different and realistic scan strategies. The scan strategies investigated include the proposed scanning mode for the forthcoming balloon-borne LSPE experiment (LSPE Collaboration et al. 2012), and a scan strategy optimized for a possible future CMB polarization satellite mission (Bock

3: REMOVING BEAM ASYMMETRY BIAS IN CMB EXPERIMENTS

et al. 2009).

The second technique that I propose for removing beam asymmetry bias is a new map-making algorithm. The map-making algorithm produces temperature and polarisation maps of the CMB that are smoothed with only the axisymmetric component of the beam. It achieves this by separating out the different spin components of the detected signal using equation (3.42). This allows us to obtain unbiased estimates for the spin-0 and spin-2 components of the signal which correspond to the temperature and polarisation of the pixel. The temperature map estimated using this technique will be clean of systematics due to the asymmetry of the beam. However, the polarisation map will still contain a temperature to polarisation leakage term due to the $k=2$ azimuthal mode of the beam. This contaminating signal can effectively be removed by calculating the leakage from the estimated temperature map and the known beam response as described in Section 3.5.2.

Removing the effects of beam asymmetry at the map level is preferable to removing it using the pseudo- C_ℓ method. There are three main reasons for this. Firstly there will be no aliasing between spectra. By removing the inter-spectra leakage at the power spectrum level one will increase the statistical error on the recovered power spectra by a factor proportional to the amplitude of the leaked spectra. A more optimal estimate of the true power spectrum can therefore be obtained if we can remove the leakage in the map domain. Secondly, the map-making algorithm can be applied before foregrounds are removed, allowing the application of traditional foreground removal techniques on the beam asymmetry-cleaned maps. Thirdly, the cleaned maps can subsequently be used for other science applications beyond the power spectrum such as CMB lensing, non-Gaussianity studies and foreground science.

The map-making algorithm requires a scan strategy to cross a pixel at multiple orientations. If this is not the case, the matrix $H_{kk'}$, defined in equation (3.41), is not invertible. In such cases, the map-making method cannot be applied (although the pseudo- C_ℓ approach could still be used). Note that, as an alternative to a highly redundant scan strategy, the required polarisation angle coverage could also be pro-

vided through the use of an appropriately positioned HWP, as is the case in the LSPE experiment (LSPE Collaboration et al. 2012).

In Section 3.8 I showed that we could use the map-making algorithm to correctly recover an input temperature power spectrum free of asymmetry bias for the same simulated satellite-like experiment as was used to test the pseudo- C_ℓ technique. In doing this I found that the noise level in the recovered power spectrum increased by $\sim 20\%$ compared to that recovered from a simply binned map. I also demonstrated that I could successfully correct the temperature and polarisation signal for the effects of beam asymmetry at the map level. To demonstrate this, I simulated a satellite-like experiment free of noise and we computed the temperature and polarisation maps using the algorithm described in Section 3.5. For the case of $k_{\max}=4$ I showed that the residual error between the resulting estimated temperature map and the input temperature map smoothed with the axisymmetric component of the beam was comparable to the numerical error in the convolution code. Finally, I have also demonstrated that this method could be very powerful for correcting for temperature to polarization leakage due to beam asymmetries. This ability, which is demonstrated in Fig. 3.9, could prove extremely useful for controlling systematics due to beam asymmetries in future precision CMB B -mode polarization experiments.

3: REMOVING BEAM ASYMMETRY BIAS IN CMB EXPERIMENTS

Chapter 4

A new map-making algorithm for CMB polarisation experiments

With the temperature power spectrum of the cosmic microwave background (CMB) at least four orders of magnitude larger than the B -mode polarisation power spectrum, any instrumental imperfections that couple temperature to polarisation must be carefully controlled and/or removed. In this chapter I present two new map-making algorithms that can create polarisation maps that are clean of temperature-to-polarisation leakage systematics due to differential gain and pointing between a detector pair. Where a half wave plate is used, I show that the spin-2 systematic due to differential ellipticity can also be removed using my algorithms. The algorithms require no prior knowledge of the imperfections or temperature sky to remove the temperature leakage. Instead, they calculate the systematic and polarisation maps in one step directly from the time ordered data (TOD). The first algorithm is designed to work with scan strategies that have a good range of crossing angles for each map pixel and the second for scan strategies that have a limited range of crossing angles. The first algorithm can also be used to identify if systematic errors that have a particular spin are present in a TOD. I demonstrate the use of both algorithms and the ability to identify systematics with simulations of TOD with realistic scan strategies and instrumental noise.

4.1 Introduction

In chapter 3 I suggested a map-making algorithm to remove systematics for experiments where there is no half-wave-plate (HWP). The method consists of two stages; first systematics of a different spin to those one wants to measure are removed (spin-0 for temperature and spin-2 for polarisation), then a second cleaning procedure is required to remove systematics of the same spin. Chapter 3 concentrated on beam systematics. Consequently, the potential source of spin-2 systematics that could couple temperature to polarisation that I considered was the second azimuthal mode of the temperature beam. To remove this I required knowledge of the beam to correctly predict this leakage from a temperature map. In this chapter I present a method similar to that used by BICEP2 Collaboration et al. (2014) to remove temperature to polarisation leakage from differential ellipticity.

Here I present novel algorithms to identify and remove some of the systematics that are problematic in CMB polarisation experiments. A key feature of our approach is that it does not require *any* prior knowledge of the telescope or CMB temperature field. In addition, since there is no fitting involved, my techniques do not result in any leakage of E -modes to B -modes. This is not true for the current state of the art technique used in BICEP2 Collaboration et al. (2014). The methods are appropriate for differencing experiments that use a stepped or rotating HWP. One of the algorithms can be used even if a HWP is not present. However, in this case only systematics of a different spin to polarisation can be removed. Where a HWP is present, it can be used to disentangle the spin-2 leakage from temperature to polarisation due the ellipticity of the beam and the spin-2 polarisation signal. The two methods differ in the scan strategies to which they can be applied. One algorithm is suited to scan strategies where each map pixel is seen at a range of telescope orientations, for example the proposed EPIC scan strategy (Bock et al. 2009). The other is suitable for experiments where the range of orientation angles for each pixel is limited, for example the LSPE scan strategy (LSPE Collaboration et al. 2012). There is no reason why the two methods

cannot be used on different portions of the same map. For example the *Planck* scan strategy (Planck Collaboration et al. 2014c) results in good orientation coverage at the ecliptic poles where the first method would be most suited and a limited range at the ecliptic plane where the second method would be more appropriate.

I demonstrate that my techniques can also be used to remove differential gain and pointing even in the absence of a HWP with a suitable scan strategy. This does leave coupling caused by differential ellipticity as without a HWP this coupling is irreducible. In this case we advocate the previous methods of Wallis et al. (2014), described in chapter 3, and BICEP2 Collaboration et al. (2014) to remove this leakage.

My techniques for removing systematic effects involve using a model for the spin of the systematics, which is employed during map-making. In principle the techniques can remove any systematic effect where the spin is known, here we simply use differential gain, pointing and ellipticity as examples of spin-0, spin-1 and spin-2 systematic effects. The algorithm provides one with Q and U maps that are free of the systematic effects included in the model, but also maps of the systematics themselves. I also demonstrate that my approach can be a useful method for identifying if a systematic is present in an experiment, or not.

The chapter is organised as follows. Section 4.2 describes the analytical framework for the algorithms to remove systematic effects. Then in Section 4.3 I demonstrate the use of the algorithms on simulations, using realistic scan strategies and time ordered data (TOD) which include instrumental noise. Section 4.4 explains how the algorithm can be used to find systematic effects and demonstrates the technique on a simulated TOD. Finally in Section 4.5 I summarise my work.

4.2 Map-making algorithms

My objective is to create maps free of systematic errors due to the imperfections in the instrumentation of an experiment. I assume the HWP is ideal and situated at the end of the optical system (in emission). The effect of the HWP is to simply rotate

the angle of the polarisation sensitivity of the beam (see, e.g. Brown et al. 2009), leaving the shape of the polarisation intensity and temperature beams unchanged. The assumption of an ideal HWP is obviously not entirely realistic. However, in practice a HWP would only ever be included in an experiment if the systematic effects that they introduce are smaller than the effects that they are designed to mitigate. Relaxing the assumption of HWP ideality is something I leave to further work. I consider an experiment where a detector pair is used to measure temperature and polarisation. Each detector is sensitive to orthogonal polarisation directions. The two signals d_1 and d_2 are summed and differenced:

$$S^{\text{add}} = \frac{1}{2}(d_1 + d_2), \quad (4.1)$$

$$S^{\text{dif}} = \frac{1}{2}(d_1 - d_2). \quad (4.2)$$

In an ideal experiment S^{add} would correspond to the temperature of the pixel and S^{dif} the rotated polarisation, the only effect of the beam would be to isotropically smooth the temperature and polarisation fields.

I will concentrate on recovering the polarisation of the pixel and therefore, I drop the superscript in equation (4.2) at this stage. Therefore, the differenced signal, S , will be the rotated polarisation of the pixel plus any systematic errors, the most serious of which will couple temperature to polarisation. Some common systematic errors include differential gain, differential pointing and differential ellipticity of the detector pair. These systematics transform as spin-0, spin-1 and spin-2 respectively with telescope orientation ψ_t . For a demonstration of the leakage angular dependence see e.g. fig 2 of Shimon et al. (2008) where the authors depict the monopole, dipole and quadrupole nature of the different systematic errors. The differential gain is spin-0 as it is simply a scaled temperature map. The differential pointing is spin-1 as the signal is a difference of the temperature map at two close points in space. The leakage, to first order, is therefore proportional to the derivative of the beam smoothed temperature field. Differencing two elliptical Gaussians results in a quadrupole pattern. This

quadrupole pattern is then convolved with the sky to create a spin-2 systematic effect. The systematic errors must be constant for this map-making algorithm to be able to remove them. If the systematics change with time, a more adaptive algorithm would need to be developed.

With the HWP at the end of the optical system there is no dependence of these systematics on the orientation of the HWP ψ_h as the effect of the HWP is to simply rotate the polarisation sensitivity by ψ_h . The detected differenced signal S is therefore,

$$S(\psi_h, \psi_t) = \Re [Pe^{i2(\psi_t+2\psi_h)} + G + Me^{i\psi_t} + Ee^{i2\psi_t}], \quad (4.3)$$

$$S(\psi_r, \psi_t) = \Re [Pe^{i2\psi_r} + G + Me^{i\psi_t} + Ee^{i2\psi_t}], \quad (4.4)$$

where P is the complex representation of the polarisation of the pixel in terms of the Stokes parameters, $P = Q + iU$. G, M and E are the temperature to polarisation leakage due to differential gain, differential pointing and differential ellipticity respectively, and \Re is the real part operator. The magnitudes and phases of the systematic errors are dependent on the nature of the imperfections and the underlying temperature field. Note however that the magnitudes and phases are unimportant for this work. Here, only knowledge of the way they transform with the telescope orientation is required in order to remove the systematic errors. In equation (4.4) I have made a coordinate transformation $\psi_r = \psi_t + 2\psi_h$. I do this so that the polarisation and systematics are dependent on different variables in our space.

The aim of this work is, therefore, to obtain an unbiased estimate of P , given that the detected signal depends on the systematic errors as well as polarisation. The two techniques which I present differ only in the scan strategies that they can be applied to. I first present an algorithm suitable for a scan strategy where the ψ_t coverage of a pixel is extensive. For example, the EPIC (Bock et al. 2009) strategy is designed to maximise this coverage. I then present a second method where the ψ_t coverage is limited. Balloon borne experiments such as LSPE (LSPE Collaboration et al. 2012) will have limited ψ_t coverage. Such experiments often include a rotatable HWP in

order to obtain multiple polarisation crossing angles.

When a rotating or stepped HWP is included in an experiment, whatever the scan strategy, the HWP can be used to provide enough polarisation angle coverage such that detector differencing is not required. As the differencing seems to lead to the temperature to polarisation leakage considered in this work, one may ask if other techniques, which do not require differencing, could be used. If the HWP is continually rotating then certain “lock-in” techniques can be used to isolate the polarisation signal from the systematic errors (Wu et al. 2007). However, maintaining continuous rotation of the HWP can cause its own wealth of systematic errors. I therefore focus of the case of a stepped HWP for which “lock-in” techniques are not applicable.

Even with a stepped HWP, the large amount of polarisation angles provided by the HWP in principle allows one to recover maps of the Stokes parameters from just one detector. Such a technique is however more problematic than differencing as the temperature to polarisation leakage could potentially be much worse. A differencing experiment allows two detectors, that are located at exactly the same position in the focal plane (and therefore observe the same point on the sky) to be used to directly remove the temperature signal (see equation 4.2). If a single detector was used to reconstruct Stokes parameter maps, then the absolute pointing error, which is typically larger than the differential pointing considered here, would create different temperature responses between different observations of a pixel and this would leak temperature fluctuations to polarisation.

A similar argument holds for ellipticity; by differencing detector pairs, one is susceptible to the difference in the ellipticity of two beams which often have very similar beam shapes. By creating polarisation maps from one detector the total ellipticity would create different temperature responses when the telescope observes a pixel at different orientations, leading to a much larger temperature to polarisation leakage. One problem that detector differencing can suffer from, and that using one detector avoids, is a constant differential calibration. However, in this case the benefits of differencing often outweigh this particular problem. Another benefit of differencing two

detectors, is that correlated noise between the detectors is removed. Motivated by these considerations I have adopted a map-making scheme that differences two detectors in a detector pair.

4.2.1 Map-making algorithm with extensive ψ_t coverage

My experimental model consists of sampling a pixel at a wide range of orientations of the telescope and HWP. The detected signal, S^d , can be expressed as,

$$S^d(\psi_r, \psi_t) = h(\psi_r, \psi_t)S(\psi_r, \psi_t), \text{ where} \quad (4.5)$$

$$h(\psi_r, \psi_t) \equiv \frac{1}{N_{\text{hits}}} \sum_{i=1}^{N_{\text{hits}}} \delta(\psi_r - \psi_r^i) \delta(\psi_t - \psi_t^i) \quad (4.6)$$

is the window function representing the knowledge that one has of the pixel. One sample, i , will contribute one delta function $\delta(\psi_r - \psi_r^i) \delta(\psi_t - \psi_t^i)$ to this window. Our aim is to obtain an unbiased estimate of the polarisation of the pixel given that the systematic errors are present and have the functional form outlined in equation (4.4). This functional form lends itself to be described well by a Fourier series. I replace each term in equation (4.5) with their Fourier series such that,

$$\sum_{n_1 m_1} \tilde{S}_{n_1, m_1}^d e^{i(n_1 \psi_r + m_1 \psi_t)} = \sum_{\substack{n_2 m_2 \\ n_3 m_3}} \tilde{h}_{n_2, m_2} e^{i(n_2 \psi_r + m_2 \psi_t)} \tilde{S}_{n_3, m_3} e^{i(n_3 \psi_r + m_3 \psi_t)}. \quad (4.7)$$

Multiplying each side by $\frac{1}{8\pi^2} e^{-i(N\psi_r + M\psi_t)}$, integrating over the whole (ψ_r, ψ_t) space and evaluating the resulting Kronecker delta function, we find

$$\begin{aligned} \tilde{S}_{n_1 m_1}^d &= \frac{1}{8\pi^2} \sum_{\substack{n_2 m_2 \\ n_3 m_3}} \tilde{h}_{n_2, m_2} \tilde{S}_{n_3, m_3} \\ &\quad \times \int_0^{4\pi} d\psi_r \int_0^{2\pi} d\psi_t e^{i[(n_2 + n_3 - n_1)\psi_r + (m_2 + m_3 - m_1)\psi_t]}, \end{aligned} \quad (4.8)$$

$$= \sum_{n_3 m_3} \tilde{h}_{n_1 - n_3, m_1 - m_3} \tilde{S}_{n_3, m_3}. \quad (4.9)$$

In principle, an unbiased estimator for the different components of the signal can now be formed by inverting equation (4.9). However, this operation is not yet possible for two reasons. Firstly, we are attempting to invert a matrix infinite in size. Secondly for any realistic window function¹ the matrix will be singular. By understanding the dependence on ψ_r and ψ_t of $S(\psi_r, \psi_t)$, we can ignore terms in equation (4.9) where $\tilde{S}_{n_3, m_3} = 0$, thereby making the operation invertible and obtaining an unbiased estimate of \tilde{S}_{n_3, m_3} from our detected \tilde{S}_{n_3, m_3}^d . If one knows the differenced signal contains temperature to polarisation leakage from differential gain one would include the term $\tilde{S}_{0,0}$. For differential pointing and ellipticity, one includes $\tilde{S}_{0,\pm 1}$ and $\tilde{S}_{0,\pm 2}$ respectively. In principle one could remove systematics of any spin by simply including the correct term. The polarisation of the pixel will be,

$$Q = 2\Re(\tilde{S}_{2,0}), \quad (4.10)$$

$$U = 2\Im(\tilde{S}_{2,0}). \quad (4.11)$$

Equation (4.9) will only be invertible if there are enough hits on the pixel at a sufficient variety of crossing angles ψ_t and HWP angles ψ_h . The more terms one includes in equation (4.9) the more observed orientations will be required.

4.2.2 Map-making algorithm with limited ψ_t coverage

The second class of experiments that we consider has a limited range of crossing angles ψ_t and obtains polarisation angle coverage using a stepped HWP. This is similar to the observation strategy envisaged for the LSPE (LSPE Collaboration et al. 2012). In this case using Fourier terms to describe the systematics is not a good choice. Here I describe a formalism that is specifically designed for a small, but non-zero, range of crossing angles.

I start from the same position as for the case of extensive ψ_t coverage in Section 4.2.1. In an experiment one has a function describing the detected signal given by

¹By realistic I specifically mean any window function where $h(\psi_r, \psi_t) = 1$.

equation (4.5). However the range of angles ψ_t is small. This restricted range of angles means that describing the full Fourier mode of each systematic would be problematic. Instead, I choose to describe the summed effect of the systematics in terms of Legendre polynomials. Let the ψ_t angles range from ψ_t^{\min} to ψ_t^{\max} . I can now define a coordinate that spans this range:

$$x = \frac{2(\psi_t - \psi_t^{\min})}{\psi_t^{\max} - \psi_t^{\min}} - 1, \quad (4.12)$$

where x ranges from -1 to 1 . With this definition I can now rewrite equation (4.4) as

$$S(\psi_r, x) = \Re [Pe^{i2\psi_r}] + f(x), \quad (4.13)$$

where $f(x)$ is a function that describes the combined effects of the systematic leakage from temperature to polarisation. If the ψ_t range is small enough then $f(x)$ will be well described by only a few Legendre polynomials. In Fig. 4.1 I show the effectiveness of the Legendre polynomials to describe a particular section of a function of the form $g(\psi) = \cos(2\psi + \pi/8)$, where the ψ range is ± 0.25 rads. This range is chosen to approximate the range of crossing angles seen in typical balloon experiments. In particular, the maximum ψ_t range in any pixel in the LSPE scan strategy (LSPE Collaboration et al. 2012) is ≈ 0.5 rads. The left panel shows that the amplitudes reduce almost exponentially with the order of the polynomial. In the centre and right panels I demonstrate that using only the first 3 Legendre polynomials, I can reconstruct the systematic to within fractions of a percent.

With this motivation I follow similar steps to those in Section 4.2.1 to create an estimate of the polarisation of a pixel free of systematics. I use the Legendre polynomials to describe the x dependence of the signal and a Fourier series to describe the ψ_r dependence. To begin I write the problem as a multiple of the underlying signal and the window function,

$$S^d(\psi_r, x) = h(\psi_r, x)S(\psi_r, x). \quad (4.14)$$

4: A NEW MAP-MAKING ALGORITHM FOR CMB POLARISATION EXPERIMENTS

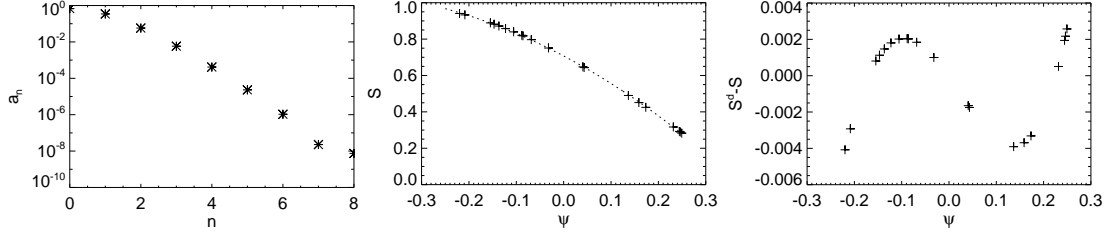


Figure 4.1: *Left panel:* The amplitudes of Legendre polynomials required to describe $g(\psi) = \cos(2\psi + \pi/8)$, where the ψ range is ± 0.25 rads. This range is typical of the ψ_t range of LSPE. *Centre panel:* A demonstration of using the first 3 Legendre polynomials to describe the systematic $g(\psi)$, the crosses are the "hits" which were randomly generated with a uniform distribution over the full range. The dashed line shows the reconstruction of the systematic error. *Right panel:* The error between the reconstruction and the input systematic error. The functional form of the residual looks very similar to that of the next polynomial in the series, $P_3(x)$.

As before I substitute the functions for their decompositions into a set of basis functions, where here I have chosen the Legendre polynomials:

$$\sum_{n_1 m_1} \tilde{S}_{n_1, m_1}^d e^{in_1 \psi_r} P_{m_1}(x) = \sum_{\substack{n_2 m_2 \\ n_3 m_3}} \tilde{h}_{n_2, m_2} e^{in_2 \psi_r} P_{m_2}(x) \tilde{S}_{n_3, m_3} e^{in_3 \psi_r} P_{m_3}(x) \quad (4.15)$$

Taking the scalar product² of both sides with a basis function leaves me with the triple integral,

$$\begin{aligned} \tilde{S}_{n_1, m_1}^d &= \frac{2m_1 + 1}{8\pi} \sum_{\substack{n_2 m_2 \\ n_3 m_3}} \tilde{h}_{n_2, m_2} \tilde{S}_{n_3, m_3} \\ &\times \int_0^{4\pi} d\psi_r \int_{-1}^1 dx e^{i[(n_2+n_3-n_1)\psi_r]} P_{m_1}(x) P_{m_2}(x) P_{m_3}(x), \end{aligned} \quad (4.17)$$

$$\tilde{S}_{n_1, m_1}^d = (2m_1 + 1) \sum_{m_2 n_3 m_3} \tilde{h}_{n_1-n_3, m_2} \tilde{S}_{n_3, m_3} \begin{pmatrix} m_1 & m_2 & m_3 \\ 0 & 0 & 0 \end{pmatrix}^2, \quad (4.18)$$

²The scalar product I use is,

$$\int_0^{4\pi} d\psi_r \int_{-1}^1 dx f(\psi_r, x) g(\psi, x). \quad (4.16)$$

where I have used the Wigner 3j symbol,

$$\begin{pmatrix} m_1 & m_2 & m_3 \\ \ell_1 & \ell_2 & \ell_3 \end{pmatrix}. \quad (4.19)$$

Once again one can obtain an unbiased estimate of the polarisation by calculating this coupling matrix and then inverting it. Explicitly the polarisation will be

$$Q = 2\Re(\tilde{S}_{2,0}), \quad (4.20)$$

$$U = 2\Im(\tilde{S}_{2,0}). \quad (4.21)$$

Just as in Section 4.2.1 where one had to ensure that one included all the Fourier modes of the systematics, here one will have to include all of the Legendre polynomials that describe $f(x)$. This will depend on the underlying systematics and the range of ψ_t angles seen at each pixel. Unlike in Section 4.2.1 where the term chosen is a direct result of the spin of the systematic error required to be removed, here there is no physical motivation for the terms to use. One simply requires that enough terms are used such that one obtains a satisfactory fit for the combined result of the systematic errors, $f(x)$.

4.3 Test on Simulations

To test the map making algorithms described in Section 4.2 I simulate two common types of experiment: one satellite-like experiment, having an extensive range of orientation angles, and one balloon-like experiment where this range is limited. To this end, I use the EPIC (Bock et al. 2009) and the LSPE (LSPE Collaboration et al. 2012) scanning strategies respectively. The hit maps of the two scan strategies are shown in

4: A NEW MAP-MAKING ALGORITHM FOR CMB POLARISATION EXPERIMENTS

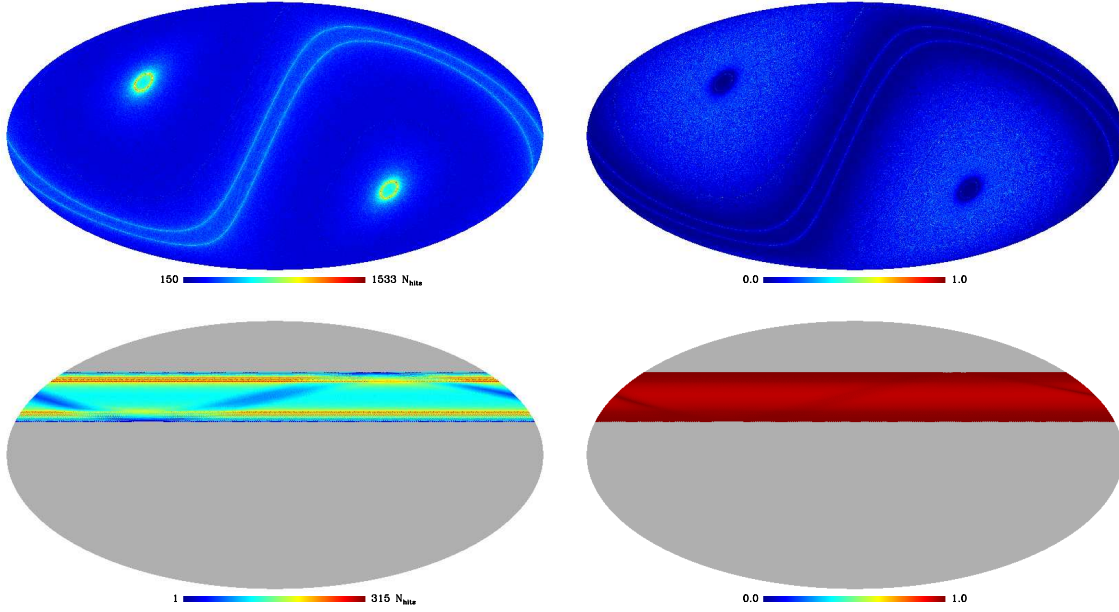


Figure 4.2: The hit maps (*left*) and polarisation coverage (*right*, p_2), see equation (4.22), of the two scan strategies used in the simulations. The plots show a full sky Mollweide projection of the sphere. *Upper panels*: the EPIC scan strategy (Bock et al. 2009) used to demonstrate the “extensive ψ_t ” range algorithm. The EPIC scan strategy is designed to mitigate systematic errors by having many crossing angles for each pixel. This projection is in Galactic coordinates with $N_{\text{side}} = 2048$. *Lower panels*: the LSPE scan strategy (LSPE Collaboration et al. 2012) used to demonstrate the “limited ψ_t ” range algorithm. The LSPE gondola will perform scans of constant azimuth, changing the elevation \sim daily. There is, therefore, a limited range of crossing angles for each pixel. LSPE will obtain good polarisation angle coverage using a stepped HWP. This projection is in Ecliptic coordinates with $N_{\text{side}} = 256$.

Fig. 4.2. In this figure, I also plot the polarisation angle coverage (p_2) for each pixel,

$$p_2 = \frac{1}{N_{\text{hits}}} \sum_{i=1}^{N_{\text{hits}}} [\cos^2(2\psi_t^i) + \sin^2(2\psi_t^i)], \quad (4.22)$$

where N_{hits} is the number of hits that a pixel has received. This quantity demonstrates the range of ψ_t angles provided by the scan strategy. The range of p_2 goes from 0 to 1 and the lower the value, the better the polarisation angle coverage.

In all the simulations I use a fiducial power spectrum with a scalar-to-tensor ratio of 0.1 and lensing B -modes are also present.

4.3.1 Extensive ψ_t coverage algorithm with a satellite-like experiment

I simulate noisy TODs with systematic errors. The main source of systematics I will be considering are leakage from temperature fluctuations to polarisation fluctuations. Therefore it may be sufficient to only simulate the systematics introduced by imperfections that couple temperature to polarisation. A TOD element, t_j , is simply the temperature and polarisation response multiplied by the underlying CMB sky and then integrated,

$$t_j = G \int d\mathbf{u} [B_j^T(\mathbf{u})T(\mathbf{u} + \Delta\mathbf{p}) + B_j^Q(\mathbf{u})Q(\mathbf{u} + \Delta\mathbf{p}) + B_j^U(\mathbf{u})U(\mathbf{u} + \Delta\mathbf{p})], \quad (4.23)$$

where $X(\mathbf{u})$ is the sky emission in the Stokes parameter X from the direction pointed to by the unit vector \mathbf{u} . $B_j^X(\mathbf{u})$ is the beam response in the direction \mathbf{u} for the Stokes parameter X when orientated in the position j . G is the gain of the detector and $\Delta\mathbf{p}$ is the shift in the temperature beam due to the pointing error. The position j describes the orientation of the telescope by the standard Euler angles and the orientation of the HWP. In order to simulate this correctly one would need to convolve the sky over this 4 dimensional space. For a high resolution experiment this would be computationally infeasible, especially when one requires many CMB realisations. I therefore only simulate beam systematics that couple temperature to polarisation due to differential ellipticity. The second and third term of the RHS of equation (4.23) can be calculated simply from a polarisation map of the sky smoothed with the axisymmetric component of the beam. In my current model of the HWP in CMB experiments, the orientation of the HWP (ψ_h) has no effect on the temperature response. Therefore, I only require the convolution of the beam over the 3 dimensional space (θ, ϕ, ψ_t) . This approximation

can be formally written as,

$$t_j = G \int d\mathbf{u} [B_j^T(\mathbf{u})T(\mathbf{u} + \Delta\mathbf{p}) + A_j^Q(\mathbf{u})Q(\mathbf{u} + \Delta\mathbf{p}) + A_j^U(\mathbf{u})U(\mathbf{u} + \Delta\mathbf{p})], \quad (4.24)$$

where $A_j^X(\mathbf{u})$ is the axisymmetric component of the beam response. The first term of equation (4.24) is calculated by a fast pixel space convolution code developed in Wallis et al. (2014) based on the algorithm described in Mitra et al. (2011). The code produces the temperature field convolved with the asymmetric beam as binned in the 3 dimensional space. In the θ and ϕ space I use a HEALPIX pixellation (Górski et al. 2005), and in the ψ_t space I use a linear binning. The convolution code calculates the central values of the pixels for this 3 dimensional grid. I use $N_{\text{side}}=2048$ for the HEALPIX pixelisation and the ψ_t space is separated into 80 bins. The second and third terms of equation (4.24) are calculated using the SYNFAST program part of the HEALPIX package. Each of these codes gives us the central values of the pixelised space. I therefore, use linear interpolation to calculate the TOD element for a particular pointing.

I use this set up to simulate the TODs for one detector pair for a given scan strategy. For the temperature beam, B^T , I use an elliptical Gaussian described by

$$B^T(\theta, \phi) = \frac{1}{2\pi q \sigma^2} e^{-\frac{\theta^2}{2\sigma^2}(\cos^2 \phi + q^{-1} \sin^2 \phi)}. \quad (4.25)$$

Equation (5.29) describes the beam for detector 1. The other detector has a similar profile except it is rotated by $\pi/2$ to create a differential ellipticity between the two detectors. I use $\sigma = 3$ arcmin corresponding to a FWHM of 7 arcmin and the ellipticity parameter $q = 1.2$.

I include a differential gain between the detectors by simply multiplying one detector's response by a constant gain factor. I also simulate a constant differential pointing by simply including an offset, in the direction of the scan, in one of the detector point-

ings in my simulation.

I use the EPIC scan strategy (Bock et al. 2009) in the following simulations with and without a stepped HWP, to simulate one detector pair that suffers from the systematics I consider in this chapter. See Fig. 4.2 for the hit map of the EPIC scan strategy. I step the HWP by $\pi/8$ every 1hr. For these satellite simulations I do not include a Galactic mask. This map-making algorithm works in a very similar way to a binned map and only requires the TOD data from one pixel to create an estimate of the Stokes Q and U of a pixel. It will therefore work equal well regardless of the sky coverage. Here I use the entire sky to make the power spectrum analysis simple.

Simulation 1: No HWP included, no noise

I simulate a noise-free TOD from a detector pair that suffers from a differential gain of the two detectors of 1% and a differential pointing of 0.1 arcmin which is 1.5% of the 7 arcmin (FWHM) beam. I do not include any differential ellipticity because in this simulation I do not have a HWP. Without a HWP the spin-2 systematic created by differential ellipticity cannot be distinguished from the spin-2 polarisation signal. Therefore, the technique I present in this chapter cannot remove the systematic. If an experiment needs to remove this systematic I suggest the methods presented in BICEP2 Collaboration et al. (2014) and Wallis et al. (2014). Fig. 4.3 shows the recovered B -mode power spectrum when a simple binned map is made from this TOD compared to one where the algorithm described in Section 4.2.1 is used. I included the terms $\tilde{S}_{0,0}$ and $\tilde{S}_{0,1}$ in equation (4.9) to account for the differential gain and pointing. In Fig. 4.3 one can clearly see that the algorithm has removed the bias on the recovered B -mode power spectrum as a result of the temperature to polarisation leakage.

Simulation 2: HWP included, no noise

I simulate a noise-free TOD from a detector pair that suffers from a differential gain of the two detectors of 1%, a differential pointing of 0.25 arcmin which is 3.5% of

4: A NEW MAP-MAKING ALGORITHM FOR CMB POLARISATION EXPERIMENTS

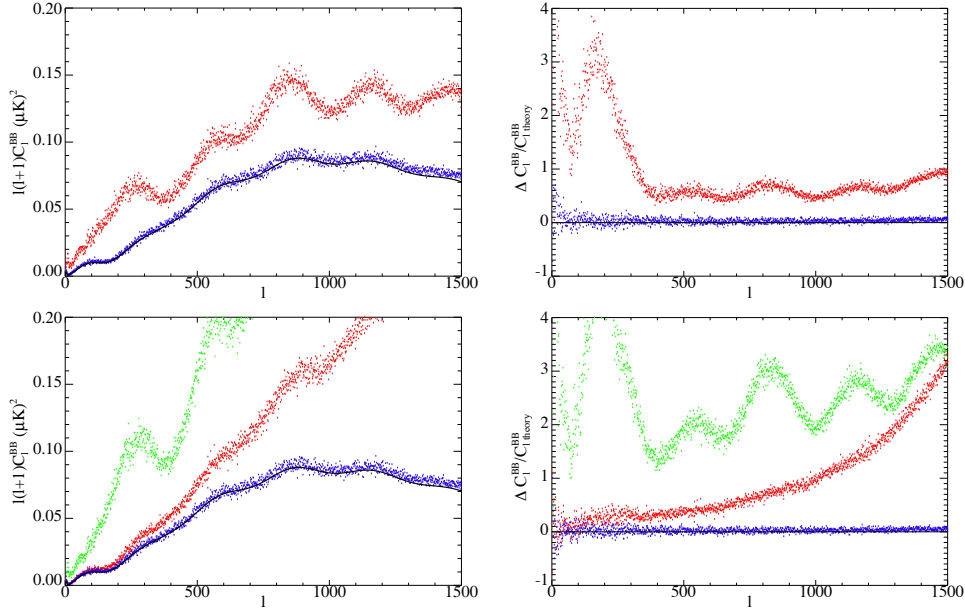


Figure 4.3: I show the recovered B -mode power spectrum for the satellite-like experiment as an example of the map-making algorithm with an extended range of ψ_t angles, see Section 4.2.1. The left column shows the power spectra and the right the fractional error for the simulations. The red dots show the results where a binned map is made and the blue the result when my algorithm is used, the input B -mode power spectra is shown in black. *First row*: the results from simulation 1, see Section 4.3.1, where I consider an experiment without a HWP and include differential gain and pointing systematics in the TOD. As there is no HWP I cannot apply my method to remove differential ellipticity so it is not included here. *Second row*: the results from simulation 2, see Section 4.3.1, where I consider an experiment with a HWP and included differential gain, pointing and ellipticity systematics in the TOD. The green dots show the recovered power spectra where a binned map is made and the TOD was created without considering a HWP to demonstrate the benefit of a HWP at mitigating systematics.

the 7 arcmin beam. The differential ellipticity is created using the beam described by equation (5.29). Figure 4.3 shows the recovered B -mode power spectrum when a simple binned map is made and a map using the algorithm described in Section 4.2.1. I included the terms $\tilde{S}_{0,0}$, $\tilde{S}_{0,1}$ and $\tilde{S}_{0,2}$ in equation (4.9) to account for the differential gain, pointing and ellipticity. Figure 4.3 shows that the bias created from the systematics has been removed. I also present the result when the same experiment is used but with no HWP present and when a binned map is made. This illustrates how a HWP can partially mitigate systematics. It also demonstrates that even with this mitigation, further systematic removal would be required.

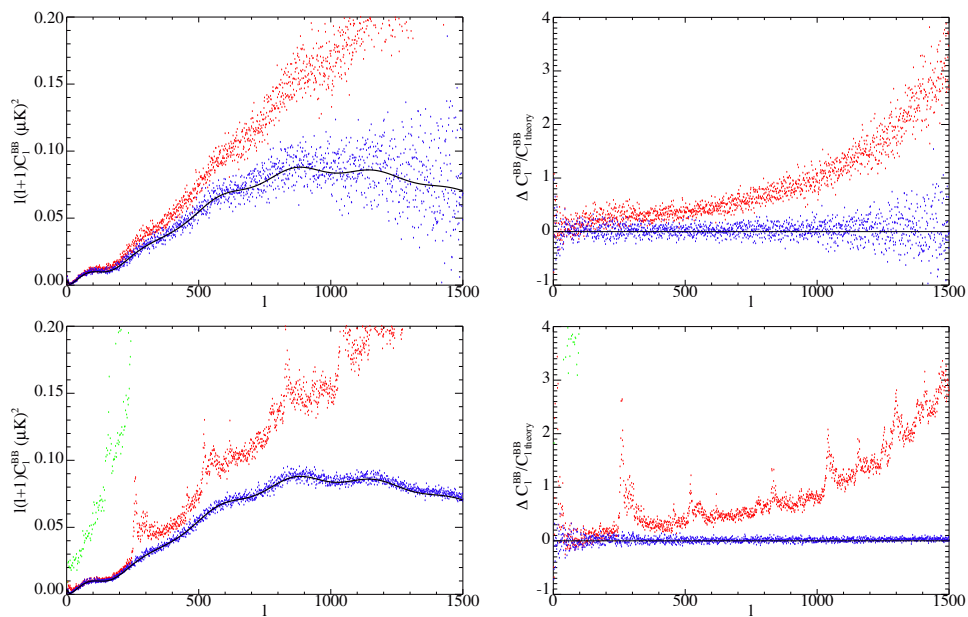


Figure 4.4: Same as figure 4.3 *First row*: the recovered power spectra for simulation 3, see Section 4.3.1. This is similar to simulation 2 but with noise included in the TOD. *Second row*: the recovered power spectra for simulation 4, see Section 4.3.1. This is similar to simulation 2 but with the CMB dipole included in the sky model and a lowered level of differential gain, see Section 4.3.1. The green dots show the recovered power spectra where a binned map is made and the TOD was created without considering a HWP to demonstrate the benefit of a HWP at mitigating systematics.

Simulation 3: HWP included, noise included

I simulate a noisy version of the TOD used in simulation 2 described in 4.3.1. I include noise in the TOD of $1 \mu\text{K}\sqrt{s}$. This is optimistic for a CMB experiment. However it is chosen so that the recovered B -mode power is easily detected with one detector pair. The algorithm can easily deal with noise as the noise simply propagates through the matrix operation to the map in the same way as it does in a binned map-making scheme. The algorithm, however, does increase the noise on the recovered Q and U measurements and it also increases the covariance of the Q and U estimates. This increase depends on the scan strategy: the more crossing angles, the lower the increase in noise. The limiting cases of this are (1) an ideal scan strategy, where the noise increase is zero and (2) where the matrix in equation (4.9) is singular, in which case

the effective increase in the noise is infinite. With noise simulations I have shown that the noise increase for the EPIC scan and this HWP set up is 12%. Fig. 4.4 shows the recovered B -mode power spectrum when a simple binned map is made and a map using the algorithm described in Section 4.2.1 and where I have removed the noise bias in each case. Again I included the terms $\tilde{S}_{0,0}$, $\tilde{S}_{0,1}$ and $\tilde{S}_{0,2}$ in equation (4.9) to account for the differential gain, pointing and ellipticity. Fig. 4.4 shows that the bias created from the systematics has been removed even in the presence of noise.

Simulation 4: HWP included, no noise, CMB dipole included

The CMB dipole can in principle leak to polarisation through the systematics considered in this chapter and this effect can be very large. Here, I test if the map-making algorithm can remove such a level of leakage. For an experiment where the large scale modes are not filtered out at the time stream level, the leakage from the CMB dipole could be problematic. Experiments of this type do have the benefit of being able to calibrate their detectors using the CMB dipole (Planck Collaboration et al. 2015b). With this benefit in mind one would expect the differential gain for such an experiment to be lower than for ground-based experiments. To reflect this effect I lower the level of differential gain in the simulations for this section. I simulate a noise-free TOD from a detector pair that suffers from a differential gain of the two detectors of 0.2%. The other two systematics were kept the same as in simulation 2 in Section 4.3.1. Figure 4.4 shows the recovered B -mode power spectrum when a simple binned map is made and a map using the algorithm described in Section 4.2.1. I included the terms $\tilde{S}_{0,0}$, $\tilde{S}_{0,1}$ and $\tilde{S}_{0,2}$ in equation (4.9) to account for the differential gain, pointing and ellipticity. Figure 4.4 shows that the bias created from the systematics has been removed. I also present the result when the same experiment is used but with no HWP present and when a binned map is made. This illustrates how a HWP can partially mitigate systematics. It also demonstrates that even with this mitigation, further systematic removal would be required.

4.3.2 Limited ψ_t coverage algorithm with a balloon-like experiment

I test the limited ψ_t range form of our map making algorithm on a balloon like experiment. I use the LSPE scan strategy (LSPE Collaboration et al. 2012) — see Fig. 4.2 for the hit map of the LSPE scan strategy. This is a typical balloon-like scan strategy where the gondola rotates rapidly to cover the sky. This provides good sky coverage (25% for LSPE). However, the pixels are always scanned in a similar direction. Although this can make systematic mitigation problematic, I show here that this problem can be avoided with a suitable map-making algorithm. Instead of using the range of crossing angles to accurately characterise the systematic and therefore remove it, here I assume that the systematics are slow enough functions of ψ_t that in the small range of ψ_t probed by the instrument, the combined effect can be described by a few Legendre polynomials. The maximum range of ψ_t for all the pixels in the LSPE scan strategy is ≈ 0.5 rads. Figure 4.1 shows that with this small range the spin-2 systematic (the fastest changing systematic we consider) can be recovered to a fraction of a percent with just the first 3 Legendre polynomials.

In the simulation I use the same beam shape as used in Wallis et al. (2014) — see Figure 1 of that paper, which has a FWHM of 1.5° . This beam is a simulation of the beam planned to be on board LPSE. I simulate TODs from a detector pair — one detector has the same beam as the other but rotated by $\pi/2$ to provide a differential ellipticity. LSPE will achieve the required angle coverage by using a stepped HWP. I simulate this by rotating the polarisation sensitivity of the beam. I step the HWP by $\pi/8$ every hour in the simulation. I simulate the LSPE scan strategy for 15 days, each day the telescope performs scans of constant elevation. I then change the elevation daily.

Unlike in the satellite-like experiment, simulating the asymmetric beam for polarisation is feasible. Even though the asymmetry of the polarised beam will in principle create a bias that our algorithm does not remove, the resulting bias is consider-

ably smaller than the temperature leakage. The simulation performed here is a good demonstration of this as I simulate the systematic errors such as differential pointing completely. However, I only remove the resulting temperature to polarisation leakage and we do not account for the resulting polarisation to polarisation errors.

As the amount of simulated data is much smaller for this low resolution balloon-like experiment, I do not have to make the same approximations as I did in the satellite-like experiment. I perform a pixel based integration of the beam multiplied by the CMB sky for each TOD element in the experiment. I simulate differential gain by multiplying the brightness temperature of one detector of the pair by 1.01 to create a 1% error. Differential pointing is created by changing the pointing position of the second detectors beam by 0.05° , which is 3% of the 1.5° FWHM beam. As described above the differential ellipticity is created using the simulated beam shown in Figure 1 of Wallis et al. (2014). I include noise in the TOD corresponding to a noise level in the map of $0.1 \mu\text{K}$ per 1.5° beam. This level of noise is optimistic for LSPE (which should achieve $\sim 7 \mu\text{K}$ per 1.5° beam (Bersanelli et al. 2012)). However, as an example of the algorithms ability to deal with noise, this level of noise is more than sufficient.

Figure 4.5 shows the recovered E - and B -mode power spectrum for the balloon-like experiment. As the LSPE scan strategy only covers 25% of the sky I use a simple pseudo- C_ℓ estimator (Brown et al. 2005) to recover the polarised power spectra. I show the recovered power spectrum averaged over 100 realisations for maps created in three ways. Unlike in the extensive ψ_t range case there is little physical interpretation of the terms removed in the limited ψ_t range case. I am creating different approximations to the combined effect of the systematic $f(x)$ from equation (4.13). The first map-making algorithm I use assumes $f(x)=0$. This is equivalent to a simple binned map and the recovered power spectra are shown as the diamonds in Figure 4.5. The bias from the binned map is obvious. I can improve this by including the term $\tilde{S}_{0,0}$ in equation (4.18). This makes the approximation $f(x)=\text{const}$ and reduces the bias by an order of magnitude, as shown in Fig. 4.5 as the stars. Finally I improve this further by assuming that $f(x)$ is a linear function. This is done by including both $\tilde{S}_{0,0}$ and $\tilde{S}_{0,1}$

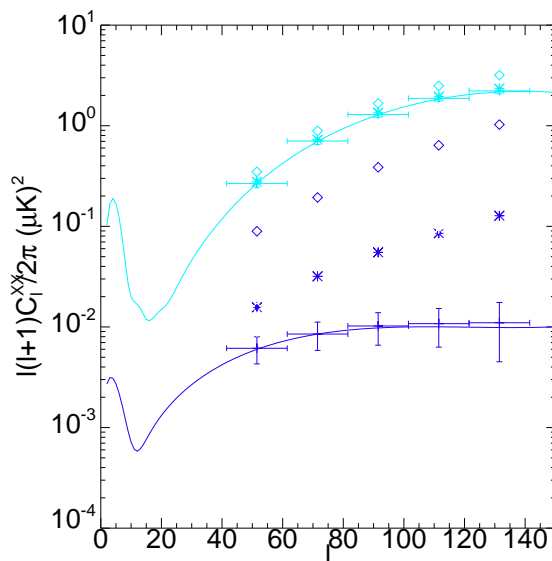


Figure 4.5: I plot the reconstruction of the E -mode and B -mode power spectrum for the balloon-like experiment, see Section 4.3.2, as an example of the map-making algorithm for a scan strategy that has a limited range of ψ_t . I show the recovered power spectrum averaged over 100 realisations for maps created in three ways. The diamonds show the recovered power spectra for a binned map, the stars correspond to including the term $\tilde{S}_{0,0}$ in equation (4.18). Finally I show the power spectra including both $\tilde{S}_{0,0}$ and $\tilde{S}_{0,1}$ in equation (4.13). The resulting recovered power spectra and error bars are shown. The bias in the recovered B -mode has been reduced by 2 orders or magnitude to less than 5% of the error bars, which as described in Section 4.3.2 is for an optimistic LSPE noise.

in equation (4.13). The resulting recovered power spectra and error bars are shown in Fig. 4.5. The bias in the recovered B -mode has been reduced by 2 orders or magnitude to less than 5% of the error bars, which as described above are error bars for an optimistic LSPE noise level.

Figure 4.5 clearly demonstrates that our technique can remove the bias as a result of temperature to polarisation leakage. However, this comes at the cost of a noise penalty in the map. Including the $\tilde{S}_{0,0}$ only and adopting $f(x)=\text{const}$ incurs a 5% increase in the noise power with respect to the binned map. The analysis where $f(x)$ is modelled as a linear function and both $\tilde{S}_{0,0}$ and $\tilde{S}_{0,1}$ terms are included in equation (4.13) creates an increase in the noise power of 12% with respect to a binned map.

4.4 Identifying Systematic Effects

The extensive ψ_t range map-making algorithm relies on being able to remove systematic effects which have different Fourier modes in (ψ_t, ψ_r) space to that of the polarisation signal. As discussed in section 4.2, the map-making algorithm requires us to know that the systematic effects are present in the TOD so that we can choose to include the correct Fourier modes in equation (4.9) and create maps that are clean of those systematic effects. I stress that one does not need to know the exact nature of the systematic effect. For example, if the experiment is suffering from differential pointing of the detector pair, at no point does one need to know by how much or in what orientation the beams are misaligned. Moreover, one does not require a temperature map to remove the signal. This is an improvement over the method used in BICEP2 Collaboration et al. (2014). One only needs to know that the experiment is suffering from differential pointing and therefore one knows to include the $\tilde{S}_{0,1}$ term in the analysis. One down side of using this method to clean systematic effects is the increase in statistical noise. Every term included in the analysis increases the statistical noise of the recovered polarisation maps, and also the cross correlation of Stokes Q and U . The level of the increase is dependent upon the scan strategy — the more extensive (ψ_t, ψ_r) coverage the experiment has, the smaller the increase of noise. I demonstrated this with simulations of the EPIC scan strategy (see Section 4.3). The increase in the noise power spectrum, going from a binned map to our map-making algorithm accounting for all three systematic errors, was 12%. This would be lower if not all systematic effects were considered. With this increase of noise in mind it would be undesirable to include terms needlessly, but one also does not want to create a bias by neglecting a term if the systematic error is present.

I now turn my attention to a practical process to determine whether a potential systematic error should be removed. I start by making a map of the systematic error. This is done in the same way that the Q and U maps are made. The inversion of equation (4.9) will give us an estimate for the $\tilde{S}_{n,m}$ terms we included. By taking the

real and imaginary parts of this one can make a map of our systematic errors. Figure 4.6 shows maps of the systematic errors recovered from simulation 3 described in Section 4.3.1. I also show the predictions for each systematic effect based on prior knowledge, and finally, the difference between the prediction and recovered systematic error maps. This figure demonstrates how one can accurately recover the systematic errors without any prior knowledge of the instrumental imperfections or of the underlying temperature field.

The top row of Figure 4.6 shows the map of differential gain. As this is a spin-0 term there is only one non-trivial map to show. The prediction is created by convolving the temperature field with the beam and multiplying it by the size of the differential gain. The difference is consistent with noise as a result of the noise in the TOD. Rows 2 and 3 show maps of differential pointing. Being spin-1, row 2 shows the error if the instrument was oriented with $\psi_t=0$ and row 3 shows the error if the telescope was orientated with $\psi_t=\pi/2$. The systematic error on a TOD sample is simply a rotation of this spin-1 vector. The prediction is created by using the first differential of the temperature map and multiplying the results by half the angular size of the differential pointing. Rows 4 and 5 are maps of the differential ellipticity. As the differential ellipticity is a spin-2 systematic error I am only able to make the distinction between the systematic error and the polarisation using the HWP. The fields depicted in rows 4 and 5 are similar to the Stokes Q and U fields respectively. The prediction was created by using the underlying temperature field and the beam shape used in the simulation. It was shown in Wallis et al. (2014) that the spin-2 systematic error would have the form,

$$\Delta a_{\ell m}^E = \sqrt{\frac{4\pi}{2\ell+1}} \Re(b_{\ell 2}^{\text{diff}}) a_{\ell m}^T, \quad (4.26)$$

$$\Delta a_{\ell m}^B = i \sqrt{\frac{4\pi}{2\ell+1}} \Im(b_{\ell 2}^{\text{diff}}) a_{\ell m}^T, \quad (4.27)$$

where $\Delta a_{\ell m}^E$ and $\Delta a_{\ell m}^B$ are the E and B -mode of the systematic error, $a_{\ell m}^T$ is the spherical harmonic decomposition of the temperature field and $b_{\ell 2}^{\text{diff}}$ is the second azimuthal

4: A NEW MAP-MAKING ALGORITHM FOR CMB POLARISATION EXPERIMENTS

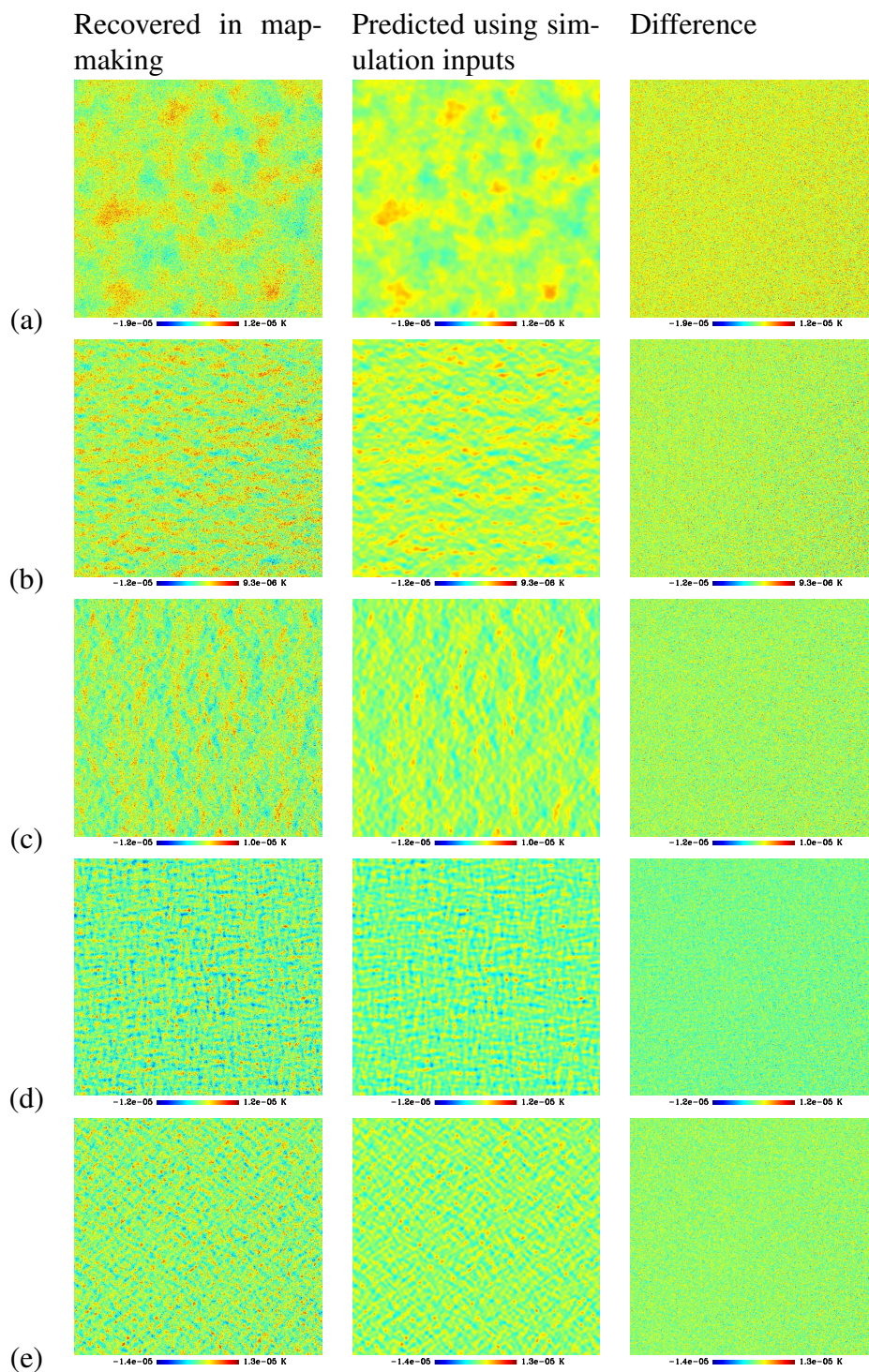


Figure 4.6: Each row shows the systematic error from the noisy TOD in simulation 3 described in Section 4.3.1. Each section of the sky is a gnomonic projection of a 12.5° square patch of sky. I plot the map extracted using the systematic error map making method described in Section 4.2 on the left. The middle column displays a prediction for the systematic error based on prior knowledge. The right column shows the difference which in each case is compatible with noise. Row (a) shows the results for differential gain ($\tilde{S}_{0,0}$), rows (b) and (c), differential pointing ($\Re[\tilde{S}_{0,1}]$ and $\Im[\tilde{S}_{0,1}]$) and rows (d) and (e) show the differential ellipticity systematic error ($\Re[\tilde{S}_{0,2}]$ and $\Im[\tilde{S}_{0,2}]$).

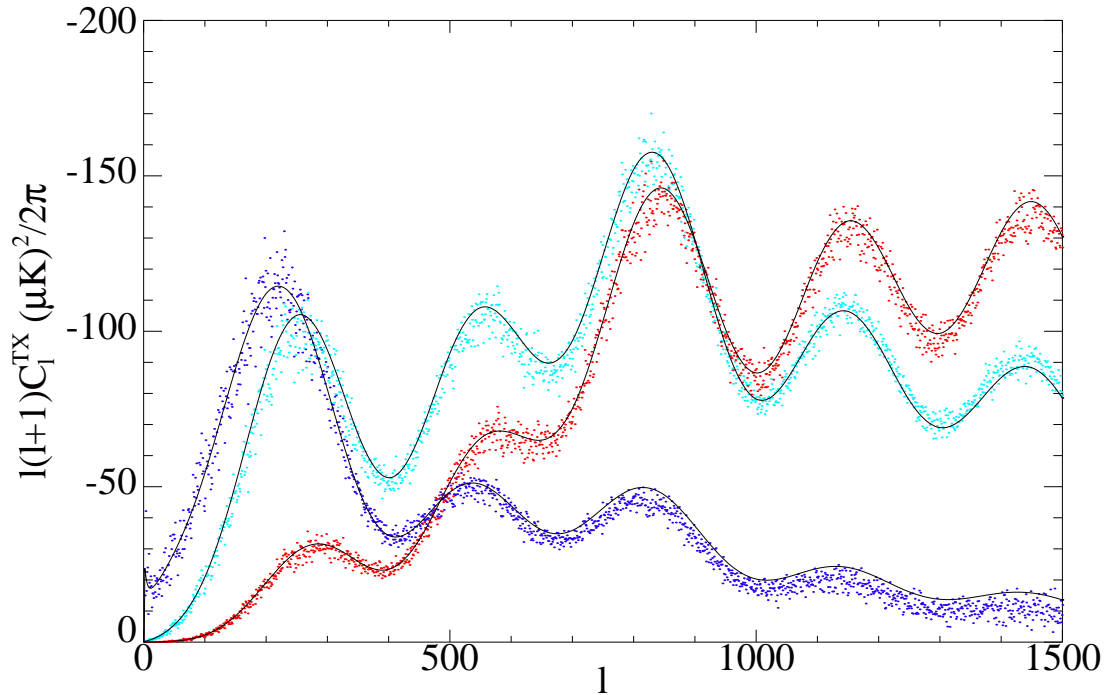


Figure 4.7: We plot the cross-correlation of the systematic maps (see Figure 4.6) with the temperature map created using the TOD in simulation 3 in Section 4.3. The cross-power spectrum is a good method to find systematics that may be below the noise level in the systematic maps. The differential gain systematic error map cross correlated with the temperature map is plotted in dark blue dots. The light blue dots show the differential pointing maps cross correlated with the temperature map. The differential ellipticity map cross correlated with the temperature map is shown as the red dots. Over plotted are $N_0 C_\ell^T$, $N_1 \ell C_\ell^T$, $N_2 \ell^2 C_\ell^T$, where N_i are normalisation factors. This demonstrates that the systematics are simply the temperature field convolved with the beam, or derivatives thereof.

mode of the spherical harmonic decomposition of the difference of the two temperature beams in the detector pair.

Figure 4.6 shows that the map-making algorithm can correctly recover maps of the systematic errors. However, the maps are noisy. One can imagine a situation where the noise level is too large to see the systematic error but there is a non-negligible effect on the recovered B -mode power spectrum. This will be especially true when many detectors are considered as the maps would have to be made for each detector pair. However, since each of the systematic errors couple to the temperature field, the recovered maps of the systematic errors will correlate with the temperature field.

In Fig. 4.7 I plot the cross-power spectrum between systematic error maps and the temperature map created using the TOD used in the simulation, where I have also deconvolved for the beam. I have over plotted $N_0 C_\ell^T$, $N_1 \ell C_\ell^T$, $N_2 \ell^2 C_\ell^T$, where N_i are normalisation factors calculated by minimising the absolute residuals between the model and the cross-power spectrum. This demonstrates the known result that the systematic effects are simply the temperature field, or some derivative of the temperature field. Even in a noisy systematic error map the cross-power spectrum will provide a valuable insight to the size of a systematic effect. I recover a non-zero correlation because the systematic effects are present in the TOD. If this were not the case and the TOD was clean then one would find a cross-power spectrum consistent with zero. This provides us with a recipe to test for the presence or absence of systematic errors: if, in an experiment, this cross-power spectrum is shown to be consistent with zero then the maps can be (re-)made not accounting for this systematic error. The resulting increase of noise in the map, with respect to a binned map, would thus be kept to a minimum.

4.5 Discussion

I have developed two map-making algorithms to remove common systematics that couple temperature to polarisation in differencing CMB polarisation experiments. The result of the map-making algorithms is the polarisation sky smoothed with the axisymmetric part of the beam used. The systematic errors I consider are differential gain, pointing and ellipticity of two detectors in a detector pair, all of which were shown to be an issue in the BICEP2 experiment (BICEP2 Collaboration et al. 2014). The main issue with these systematic errors is the leakage from temperature to polarisation that they create. Shimon et al. (2008) showed that the coupling from temperature to polarisation of these systematic errors have spin-0,1 and 2 properties respectively. I used this understanding to develop the algorithm used here.

The first algorithm, described in Section 4.2.1, removes the systematic errors by separating the Fourier modes of the systematic errors and the Fourier mode of the

polarisation, using equation (4.9). The technique requires a suitable scan strategy. The angle coverage of the orientation of the telescope, ψ_t , must be extensive to allow for the different Fourier modes to be distinguished. I have shown through simulations in Section 4.3.1 that the EPIC (Bock et al. 2009) scan strategy provides the required amount of angle coverage.

In Section 4.3.1 I demonstrated the effectiveness of the algorithm through three simulations. Simulation 1 showed the ability of the technique to remove differential gain and pointing when a HWP is not used. Without a HWP the spin-2 systematic and the polarisation signal are degenerate and, therefore, cannot be separated using this technique. In this case I suggest using the methods proposed in Wallis et al. (2014) and BICEP2 Collaboration et al. (2014). The technique however, can remove differential gain and pointing as they have a different spin to the polarisation signal. In Section 4.3.1 and 4.3.1 I presented simulations including a HWP. In these simulations I showed that the technique can simultaneously remove differential gain, pointing and ellipticity. The CMB dipole can contribute to the leakage from temperature to polarisation. I demonstrated in Section 4.3.1 that the map-making algorithm can deal with this level of leakage.

One draw back to this technique is an increase in the statistical noise in the resultant (cleaned) Q and U maps. The level of the noise increase is dependent on the scan strategy — the more even the ψ_t angle coverage, the lower the increase in noise. An ideal experiment would suffer no increase in noise. At the other extreme where the coverage is not large enough, the matrix in equation (4.9) becomes singular and the effective increase in noise is infinite. Through simulations we have shown that the increase in noise power for simulation 3 is 12% when compared to a binned map.

The second algorithm, described in Section 4.2.2, removes the temperature to polarisation leakage by creating a model for the total leakage as a function of the orientation of the telescope. The combined effect of the systematic error is modelled as a smooth function of the orientation angle. With this assumption I can then describe the combined systematic $f(x)$ by a few Legendre polynomials. Figure 4.1 shows that

a spin-2 systematic can accurately be reconstructed by the first three Legendre polynomials, with a ψ_t range of 0.5 rads. This ψ_t range was chosen to be representative of the LSPE scan strategy (LSPE Collaboration et al. 2012), where the maximum ψ_t range is ≈ 0.5 rads. In Section 4.3.2, I demonstrated that the algorithm can remove the temperature to polarisation leakage from differential gain, pointing and ellipticity in a simulation where the LSPE scan strategy was used with a stepped HWP. As with the extensive ψ_t range technique there is an increase in the statistical noise of the polarisation maps when using this technique. Through simulations I showed that the increase of noise using the LSPE scan strategy was 12%.

In Section 4.4 I have presented a method to identify if systematics are present in a TOD. The extensive ψ_t range algorithm separates the systematic errors into Fourier modes and generates an estimate of the polarisation free of these systematic errors. It also at the same time creates an estimate of the systematic error. We showed in Fig. 4.6 the maps of the systematic errors recovered from simulation 3 (see Section 4.3.1). These maps can be used to identify if a systematic error is present. However, the noise in the TOD and the relative size of the systematic error could render the reconstructed maps too noisy to see the systematic error easily. To increase the signal-to-noise, I suggest calculating the cross-power spectrum of these systematic maps with the temperature map. As the systematic error I am considering are due to temperature to polarisation leakage then, if the systematic is present, one would expect to see a non-zero cross-correlation. I showed the cross-power spectrum between the systematic error maps and the temperature map created using the TOD in Fig. 4.7. This technique can be used to identify if systematics are present. This is crucial to test the validity of an experiment's polarisation maps, but could also be used to identify whether a systematic error must be removed using this technique. Accounting only for those systematic errors that are actually present in the TOD would minimise the increase in noise associated with the correction algorithms developed in this work.

Chapter 5

Optimal scan strategies for the next generation of CMB polarisation satellite experiments

The B -mode polarisation power spectrum in the Cosmic Microwave Background (CMB) is about four orders of magnitude fainter than the CMB temperature power spectrum. Any instrumental imperfections that couple temperature fluctuations to B -mode polarisation must therefore be carefully controlled and/or removed. In the chapter I investigate the role that a scan strategy can have in mitigating certain common systematics by averaging systematic errors down with many crossing angles. I present approximate analytic forms for the error on the recovered B -mode power spectrum that would result from differential gain, differential pointing and differential ellipticity for the case where two detector pairs are used in a polarisation experiment. I use these analytic predictions to search the parameter space of common satellite scan strategies in order to identify those features of a scan strategy that have most impact in mitigating systematic effects. I find that, as long as the satellite spin period is much less than the precession period, and that both are much less than 1 year, the exact values of the timescales are unimportant from the point of view of mitigating systematics. I conclude that the main

parameters of interest are the precession angle and the boresight angle. By reducing the boresight angle and increasing the precession angle, a scan strategy will scan the sky in small circles. These small circles are beneficial for creating a wide range of orientation angles, and are therefore effective in mitigating systematic effects.

5.1 Introduction

Here, I examine how satellite scan strategies can be designed to mitigate various systematic effects that couple temperature to polarisation for satellite-based experiments. In my study, I focus on differencing experiments, consisting of pairs of detectors. Within each pair, one detector is sensitive to the CMB temperature and polarisation signal in a particular direction on the sky, convolved with some detector response function. The other detector is in principle sensitive to the same temperature signal but has a polarisation sensitivity that is rotated by 90 degrees. By differencing the timestreams of these two detectors, the temperature response is removed. However, any differences between the two temperature response functions of the detectors will couple temperature fluctuations to the polarisation map.

In this study, I consider three types of mismatch between the two temperature response functions, all of which were found to be present in the BICEP2 experiment (BICEP2 Collaboration et al. 2015). Firstly, I consider a difference in the gain calibration of the two detectors which I term “differential gain”. I also consider a difference in the pointing direction of the two detector response functions, which I call “differential pointing”. Finally I investigate the impact of a “differential ellipticity” arising from a difference in the beam ellipticities of the two detectors.

The systematics I consider are characteristic of the type of experiment set up I have chosen. By using bolometers, that do not conserve the phase of the incoming radiation, differencing or polarisation angle rotation must be used to disentangle polarisation from the temperature response of the detector. Bolometers have gained near photon noise levels, therefore, are preferred by modern day CMB polarisation experiments.

The South Pole Telescope (Padin et al. 2008), BICEP2 (BICEP2 Collaboration et al. 2014) and the POLARBEAR collaboration (The Polarbear Collaboration: P. A. R. Ade et al. 2014), all use bolometers. Using a half wave plate (HWP) can allow one to make maps of temperature and polarisation without differencing. If the HWP is continually rotating then certain “lock-in” techniques can be used to isolate the polarisation signal from the systematic errors (Wu et al. 2007). However, maintaining continuous rotation of the HWP can cause its own wealth of systematic errors. When a HWP angle is stepped at certain periods they can be used to increase the polarisation coverage and mitigate systematic errors. However, HWP’s can introduce other systematic errors themselves, therefore they are often not used.

A large body of work has been undertaken to identify optimal scan strategies for CMB satellite experiments. Delabrouille et al. (2000) identifies the requirements for the scan strategy for the *Planck* mission. One requirement of which is the need to have multiple crossing angles to mitigate systematic errors that depend on the orientation, or parallactic angle, of the telescope a problem I turn my attention to now. Delabrouille et al. (1998) looked at the increase of noise due to instrumental drift, or $1/f$ noise, and the benefit that a well chosen scan strategy can have on the final power spectrum analysis. The benefits of different scan strategies for *Planck* were described in Dupac & Tauber (2005), where the authors attempt to maximise the uniformity of the integration time over the sky.

The aim of my study is to examine the degree to which a scan strategy can mitigate systematic errors by averaging their effect through multiple observations of the same sky pixel with different instrument orientations. To do this I first derive a set of simple equations that predict the error on the recovered B -mode polarisation power spectrum given a few characteristics of the scan strategy and the amplitude of the systematic effect. I then go on to use these simple equations to predict the error on the B -mode polarisation power spectrum for different satellite scan strategies. This allows us to clearly identify those features of a scan strategy that have the most impact in controlling the level of instrumental B -mode polarisation.

The chapter is organised as follows. In Section 5.2 I derive the equations that predict the temperature-to-polarisation leakage due to these systematic effects. In Section 5.3 I use time order data simulations to demonstrate the validity of the equations derived in Section 5.2. In Section 5.4 I search the main parameter space of satellite scan strategies to identify those key features that have the largest impact in terms of mitigating systematic effects. Finally in Section 5.5 I summarise my results.

5.2 Impact of systematics on the B -mode power spectrum

To assess the impact of the systematic effects on the recovered B -mode power spectrum we begin by considering the detected signal from a single pair of detectors. The detected signal from a single detector pointing at sky position Ω is

$$d_i^X = \int d\Omega [B^T(\Omega)T(\Omega) + B^Q(\Omega)Q(\Omega) + B^U(\Omega)U(\Omega)], \quad (5.1)$$

where i denotes the pair that the detector belongs to and $X = \{A, B\}$ distinguishes between the two detectors within a pair. $B^Y(\Omega)$ is the beam response function of the detector to the Stokes parameters $Y = \{T, Q, U\}$. In this work we focus on the most problematic systematic effects for CMB B -mode experiments – those which couple the temperature signal to polarisation maps. I consider a differencing experiment, one where each detectors come in pairs each sensitive to orthogonal polarisation directions. The timestream from two detectors in a pair can be summed to obtain the temperature of the sky and differenced to obtain a measurement of the polarisation. Therefore any mismatch in the response of the two detectors to the temperature sky will result in this type of leakage. Explicitly the differenced signal is,

$$d_i = \frac{1}{2}(d_i^A - d_i^B). \quad (5.2)$$

I describe the pointing of the telescope using Euler angles, $\omega = (\theta, \phi, \psi)$ defined in 3.2.

One important characteristic of a systematic error, when considering the impact on the recovered polarisation maps and power spectra, is the spin of the systematic error. The spin is defined by how the temperature leakage rotates with the orientation of the telescope for a particular sky pixel. Here I have defined the orientation angle by ψ , which is the angle between the orientation of the focal plane and the direction to the North pole, this is often referred to as the parallactic angle of the telescope. If the systematic error is of a different spin to the spin-2 polarisation signal, then if a sky pixel is observed at many instrument orientations the resulting bias on the measured polarisation is reduced. The primary goal of this study is to examine the effectiveness of different scan strategies to mitigate systematic errors in this way. To do this I derive a simple analytic set of equations to predict the leaked B -mode polarisation power spectrum correct to the lowest order terms in the size of the systematic effect. The first stage of the is to calculate leakage into the polarisation timestream of each systematic error.

5.2.1 Leakage in the differenced timestream

I start by examining the effect of differential gain on the differenced signal from a detector pair. This is simply a mis-calibration between the two detectors of δg_i . The temperature leakage, δd_i^g , due to differential gain (δg_i) in detector pair i is,

$$\delta d_i^g = \frac{1}{2}(T^B(\Omega) - (1 - \delta g_i)T^B(\Omega)) \quad (5.3)$$

$$= \frac{1}{2}\delta g_i T^B(\Omega), \quad (5.4)$$

$$= G^i \quad (5.5)$$

where $T^B(\Omega)$ denotes the CMB temperature sky convolved with the axisymmetric part of the temperature beam and this defines the level of the systematic gain, G^i . This

systematic effect is independent of the orientation of the telescope with respect to the sky coordinates. It depends only on the size of the temperature signal in the direction in which the telescope is pointing at any given time. Differential gain is, therefore, a spin-0 systematic effect.

The second systematic effect I consider is differential pointing. This is a misalignment of the two detector beams by some angle ρ_i in a direction χ_i with respect to the orientation of the telescope from North (ψ), see Fig. 5.1. As the differential pointing will be a small angle, I make the flat sky approximation. Consider a Cartesian coordinate system where the y -axis is aligned with North. The error in the differenced timestream can then be modelled as,

$$\delta d_i^{\text{p}} = \frac{1}{2} [T^{\text{B}}(x, y) - T^{\text{B}}(x - \rho_i \sin(\psi + \chi_i), y - \rho_i \cos(\psi + \chi_i))]. \quad (5.6)$$

If we Taylor expand around (x, y) to first order in ρ_i , we find

$$\delta d_i^{\text{p}} = \frac{1}{2} \left[\frac{\partial T^{\text{B}}}{\partial x} \rho_i \sin(\psi + \chi_i) + \frac{\partial T^{\text{B}}}{\partial y} \rho_i \cos(\psi + \chi_i) \right], \quad (5.7)$$

$$= \frac{1}{4} \left[\left(\frac{\partial T^{\text{B}}}{\partial y} - i \frac{\partial T^{\text{B}}}{\partial x} \right) \rho_i e^{i(\psi + \chi_i)} + \text{c.c.} \right], \quad (5.8)$$

$$= \frac{1}{2} (M^i e^{i\psi} + \text{c.c.}) \quad (5.9)$$

where c.c. denotes the complex conjugate of the first term inside the square bracket and this defines the systematic error due to differential pointing M^i . The $e^{i\psi}$ term signifies the known result that differential pointing is a spin-1 systematic effect.

The final systematic effect I consider is a differential ellipticity between the detector pairs. To treat this, it is convenient to write the integration in equation (5.1) in spherical harmonic space. For simplicity I use a coordinate system with the North pole coincident with the pointing centre. I denote the beam decomposed into spherical harmonics as $b_{\ell k}^{\text{X}}$ and the temperature sky is denoted by $a_{\ell m}^{\text{T}}$. The error on the differenced

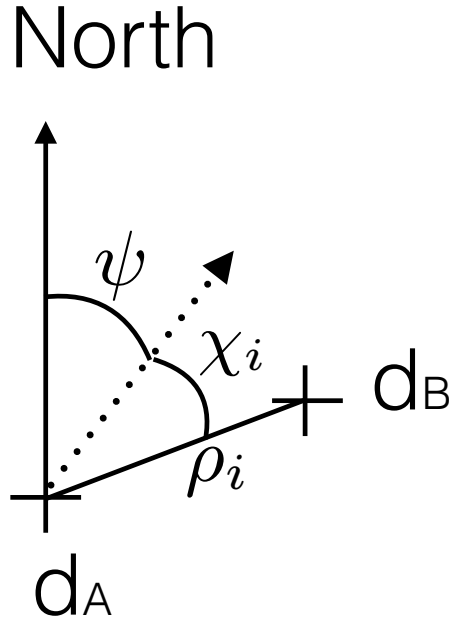


Figure 5.1: Schematic diagram to define the parameters used to define the differential pointing of a detector pair. The detector beams centred at an angle ρ_i with respect to each other, in a direction which is an angle χ_i with respect to the scan direction, which in turn is an angle ψ from North, the parallactic angle.

signal between the two detectors within a pair is then

$$\delta d_i^e = \frac{1}{2} \sum_{\ell m} \sqrt{\frac{4\pi}{2\ell+1}} (b_{\ell m}^A a_{\ell m}^{T*} - b_{\ell m}^B a_{\ell m}^{T*}), \quad (5.10)$$

$$\approx \frac{1}{2} \sum_{\ell} \sqrt{\frac{4\pi}{2\ell+1}} (\delta b_{\ell,2}^i a_{\ell,2}^{T*} + \delta b_{\ell,-2}^i a_{\ell,-2}^{T*}), \quad (5.11)$$

where I have assumed that the axisymmetric components of the two detector beams cancel and that the dominant remaining term is the second azimuthal mode. This is demonstrated to be true for an elliptical Gaussian beam in figure 2 of Wallis et al. (2014). When the telescope orientation is changed, but the same patch of sky is observed, this differential ellipticity will rotate as, $\delta b'_{\ell,2} = e^{i2\psi} \delta b_{\ell,2}$. This rotation makes

the differential ellipticity effect a spin-2 effect. We can, therefore, rewrite the temperature leakage due to differential ellipticity as a function of the orientation of the telescope as

$$\delta d_i^e \approx \frac{1}{2} \sum_{\ell} \sqrt{\frac{4\pi}{2\ell+1}} (\delta b_{\ell,2}^i a_{\ell,2}^{T*} e^{i2\psi} + \delta b_{\ell,-2}^i a_{\ell,-2}^{T*} e^{-i2\psi}), \quad (5.12)$$

$$= \frac{1}{2} (E^i e^{i2\psi} + \text{c.c.}), \quad (5.13)$$

which defines E^i .

5.2.2 Temperature leakage to the polarisation map

I can combine the above understanding of the temperature leakage effects due to the various systematics to create a model for the differenced signal as a function of the orientation of the telescope. The differenced signal from a detector pair i for a single sky pixel is given by

$$S^i(\psi) = G^i + \frac{1}{2} [P e^{i2\psi} + M^i e^{i\psi} + E^i e^{i2\psi} + \text{c.c.}], \quad (5.14)$$

where $P = Q + iU$ is the complex representation of the polarisation signal in the sky pixel. G^i , M^i and E^i are the contributions to the differenced signal from the three systematic effects I am considering — differential gain, pointing and ellipticity respectively. The exact form of G^i , M^i and E^i are defined in equations (5.5,5.9,5.13). To understand the effect that these systematics have on the recovered power spectrum we first examine the effect that they have on the map.

In general, each pixel of a map will be observed at a variety of orientation angles ψ . I define the detected signal as S^d which is the information that we have about the

pixel as a function of the orientation,

$$S^d(\psi) = h(\psi)S(\psi), \text{ where,} \quad (5.15)$$

$$h(\psi) = \frac{2\pi}{N_{\text{hits}}} \sum_j \delta(\psi - \psi_j). \quad (5.16)$$

Here, ψ_j is the orientation of the j th observation (or “hit”) of the pixel and the sum is over all observations “hits” of the pixel, N_{hits} .

Let us now consider the signal seen by two detector pairs. To do this imagine an “instrument- Q ” detector pair whose orientation with respect to the sky coordinates for the j th observation is labelled ψ_j and an “instrument- U ” pair of detectors whose polarization sensitivity directions are rotated by $\pi/4$ with respect to those of the “instrument- Q ” detectors. For every hit, there will then be two orientations, one at ψ_j and the other at $\psi_j + \pi/4$, each with different systematic effects. We can therefore write

$$S_{\text{tot}}^d(\psi) = h(\psi)S^1(\psi) + h(\psi - \pi/4)S^2(\psi), \quad (5.17)$$

which we can write in Fourier space as a convolution:¹

$$\tilde{S}_k^d = \sum_{k'=-\infty}^{\infty} \tilde{h}_{k-k'} \tilde{S}_{k'}^1 + \tilde{h}_{k-k'} e^{i\pi(k'-k)/4} \tilde{S}_{k'}^2. \quad (5.18)$$

From equation (5.14) we can see that $S^i(\psi)$ is made up of only a few Fourier terms. Therefore equation (5.18) can also be limited to just a few terms, explicitly the $k' = -2$

¹The Fourier transform and inverse I use is,

$$\begin{aligned} \tilde{f}_k &= \frac{1}{2\pi} \int_0^{2\pi} d\psi e^{ik\psi} f(\psi), \\ f(\psi) &= \sum_{k=-\infty}^{\infty} \tilde{f}_k e^{-ik\psi}. \end{aligned}$$

to $k'=2$ terms. We can use these simplifications to write out the $k = 2$ row of \tilde{S}_k^d :

$$\begin{aligned}\tilde{S}_2^d &= \tilde{h}_0(\tilde{S}_2^1 + \tilde{S}_2^2) + \tilde{h}_1(\tilde{S}_1^1 + e^{i\pi/4}\tilde{S}_1^2) + \tilde{h}_2(\tilde{S}_0^1 + i\tilde{S}_0^2) \\ &+ \tilde{h}_3(\tilde{S}_{-1}^1 + e^{i3\pi/4}\tilde{S}_{-1}^2) + \tilde{h}_4(\tilde{S}_{-2}^1 - \tilde{S}_{-2}^2).\end{aligned}\quad (5.19)$$

We can see from the definition of $h(\psi)$ in equation (5.16) that $\tilde{h}_0=1$; also from equation (5.14) we can see that $S_2^i=P/2$ and $S_{-2}^i=P^*/2$. Therefore, in the absence of any systematic effects or instrumental noise, $\tilde{S}_2^d=P$. In a simple binning map-making scheme this leads to an estimate of the polarisation in a pixel. We can now deduce the spurious polarisation signal by examining equation (5.19). Any additional terms, beyond the expected P , will be spurious. Performing this analysis for the systematic effects we have considered, and defining the differential operator $\nabla = (\partial/\partial y - i\partial/\partial x)$, we find the following systematic terms in the polarization maps:

$$\Delta P^g = \frac{1}{2}\tilde{h}_2(\delta g_1 + i\delta g_2)T^B, \quad (5.20)$$

$$\begin{aligned}\Delta P^p &= \frac{1}{4}\tilde{h}_1\nabla T^B(\rho_1 e^{i\chi_1} + \rho_2 e^{i(\chi_2+\pi/4)}) \\ &+ \frac{1}{4}\tilde{h}_3\nabla^* T^B(\rho_1 e^{-i\chi_1} + \rho_2 e^{-i(\chi_2-3\pi/4)}),\end{aligned}\quad (5.21)$$

$$\begin{aligned}\Delta P^e &= \frac{1}{2}\sqrt{\frac{4\pi}{2\ell+1}}(\delta b_{\ell,2}^1 + \delta b_{\ell,2}^2)a_{\ell,2}^{T*} \\ &+ \frac{1}{2}\tilde{h}_4\sqrt{\frac{4\pi}{2\ell+1}}(\delta b_{\ell,-2}^1 - \delta b_{\ell,-2}^2)a_{\ell,-2}^{T*}.\end{aligned}\quad (5.22)$$

5.2.3 Temperature leakage to the B -mode power spectrum

I now wish to calculate the error on the B -mode polarisation power spectrum. As the window function, $h(\psi)$, will be different for each pixel, an exact calculation is a difficult computational task. However, we can simplify the problem with a few approximations. Firstly, I assume that the only effect the \tilde{h}_k term of equations (5.20)–(5.22) have on the power spectrum is to damp the resulting bias by a factor of $\langle |\tilde{h}_k|^2 \rangle$, where the average is over all pixels of the sky. The phase of \tilde{h}_k across the sky, and its cou-

5.2: IMPACT OF SYSTEMATICS ON THE B-MODE POWER SPECTRUM

pling to the temperature sky, will dictate whether or not the spurious polarisation is of a E -mode or B -mode form and therefore one expects this approximation to give an indication of the amplitude of the effect. As we do not expect the scan strategy to correlate with the temperature sky, I assume that half the resulting bias power will be of E -mode and half of B -mode form. The temperature terms in the spurious polarisation will result in an error on the B -mode power spectrum whose size is proportional to the temperature power spectrum. In equation (5.20) the temperature field is convolved with the axisymmetric component of the beam. Therefore, the resulting bias will be proportional to $B_\ell^2 C_\ell^T$, where $B_\ell = \sqrt{\frac{4\pi}{2\ell+1}} b_{\ell 0}$ is the smoothing function due to the beam. The differential pointing is dependent on the gradient of the convolved temperature sky and therefore the bias will be proportional to $\ell^2 B_\ell^2 C_\ell^T$. The differential ellipticity is dependent on the temperature field directly and the resulting bias will be proportional to C_ℓ^T . For the systematic error terms, I simply take the modulus squared. I provide justification for, and examine the impact of, these approximations in Appendix B.1. In Section 5.3, I demonstrate with full time-ordered data (TOD) simulations the accuracy of the approximations for a selection of representative scan strategies.

With the approximations described above, we find the following expressions for the bias on the B -mode power spectrum resulting from the systematic effects we have considered:

$$\Delta \tilde{C}_\ell^{BBg} = \frac{1}{8} \langle |\tilde{h}_2|^2 \rangle |\delta g_1 + i\delta g_2|^2 B_\ell^2 C_\ell^{TT}, \quad (5.23)$$

$$\begin{aligned} \Delta \tilde{C}_\ell^{BBp} &= \frac{1}{32} \langle |\tilde{h}_1|^2 \rangle |\rho_1 e^{i\chi_1} + i\rho_2 e^{i(\chi_2 + \pi/4)}|^2 \ell^2 B_\ell^2 C_\ell^{TT}, \quad (5.24) \\ &+ \frac{1}{32} \langle |\tilde{h}_3|^2 \rangle |\rho_1 e^{-i\chi_1} + i\rho_2 e^{-i(\chi_2 - 3\pi/4)}|^2 \ell^2 B_\ell^2 C_\ell^{TT} \end{aligned}$$

$$\begin{aligned} \Delta \tilde{C}_\ell^{BBe} &= \frac{4\pi}{4(2\ell + 1)} |\Im [\delta b_{\ell 2}^1 + \delta b_{\ell 2}^2]|^2 C_\ell^{TT} \quad (5.25) \\ &+ \frac{4\pi}{8(2\ell + 1)} \langle |\tilde{h}_4|^2 \rangle |\delta b_{\ell 2}^1 - \delta b_{\ell 2}^2|^2 C_\ell^{TT}. \end{aligned}$$

Finally we must also consider the beam deconvolution, as the reconstructed polarisation map will be smoothed with the beam. When analysing a real experiment the

recovered B -mode power spectrum will be deconvolved for the beam. To take this into account we divide equations (5.23)–(5.25) by B_ℓ^2 giving us,

$$\Delta C_\ell^{BBg} = \frac{1}{8} \langle |\tilde{h}_2|^2 \rangle |\delta g_1 + i\delta g_2|^2 C_\ell^{TT}, \quad (5.26)$$

$$\begin{aligned} \Delta C_\ell^{BBp} &= \frac{1}{32} \langle |\tilde{h}_1|^2 \rangle |\rho_1 e^{i\chi_1} + i\rho_2 e^{i(\chi_2 + \pi/4)}|^2 \ell^2 C_\ell^{TT}, \\ &+ \frac{1}{32} \langle |\tilde{h}_3|^2 \rangle |\rho_1 e^{-i\chi_1} + i\rho_2 e^{-i(\chi_2 - 3\pi/4)}|^2 \ell^2 C_\ell^{TT} \end{aligned} \quad (5.27)$$

$$\begin{aligned} \Delta C_\ell^{BBe} &= \frac{1}{4} \left| \Im \left[\frac{\delta b_{\ell 2}^1 + \delta b_{\ell 2}^2}{b_{\ell 0}} \right] \right|^2 C_\ell^{TT} \\ &+ \frac{1}{8} \langle |\tilde{h}_4|^2 \rangle \left| \frac{\delta b_{\ell 2}^1 - \delta b_{\ell 2}^2}{b_{\ell 0}} \right|^2 C_\ell^{TT}, \end{aligned} \quad (5.28)$$

where the various terms are described in Table 5.1. One can immediately see the effect that a good scan strategy can have on mitigating systematic effects. By providing us with a range of instrument orientations, $|\tilde{h}_n|$, where $n \neq 0$, will be lowered for each pixel. This in turn reduces the impact of the systematics on the recovered power spectrum.

I note that a differential ellipticity of the beams within a detector pair can couple temperature to polarisation with a spin-2 systematic effect (see equation 5.14). This means that no scan strategy can mitigate the effects of this systematic error. It has been shown previously (O’Dea et al. 2007; Shimon et al. 2008; Wallis et al. 2014) that if the orientation of the ellipticity is in the same direction or perpendicular to the polarisation sensitivity then this systematic effect will only couple temperature fluctuations to E -mode polarisation. Any misalignment however will couple to B -modes. This can be seen in the first term of equation (5.28) as the imaginary part of $\delta b_{\ell 2}$ coupling temperature power to B -mode polarisation. The second term of equation (5.28) does allow coupling between temperature fluctuations and B -mode polarisation regardless of the orientation of the ellipticity as long as the two detector pairs have different differential ellipticity. However, this effect can be mitigated by the scan strategy, as a result of the $\langle |\tilde{h}_4|^2 \rangle$ factor.

Symbol	Description	Value set to in relevant simulation
ψ	The orientation of the scan direction with respect to North	Varies with scan strategy, position and time
\tilde{h}_n	The average of the complex exponential of the orientations for a pixel, $\langle e^{in\psi} \rangle_{\text{hits}}$	Varies with scan and pixel
FWHM	the full width at half the maximum of the beam	7 arcmin for all the simulations
δg_i	The differential gain between the two detectors in pair i	0.01 for both detector pairs
ρ_i	The angle between the two beam centres in pair i	0.1 arcmin for both (1.5% of the FWHM)
χ_i	The orientation of the second beam from the first in a detector pair i relative to the direction of the scan	0 and $\pi/4$
$b_{\ell m}$	The spherical harmonic decomposition of the temperature beam	That of an elliptical Gaussian — see equation (5.29)
$\delta b_{\ell m}^i$	The spherical harmonic decomposition of the difference of the temperature beams of pair i	That of an elliptical Gaussian — see equation (5.29)
q	Ellipticity parameter for the elliptical Gaussian beam, $q = 1$ is axisymmetric, see equation (5.29)	1.05 and 1

Table 5.1: Description of the variables used in the analysis (see Sections 5.2 & 5.3 in the main text) and the values adopted for the simulations.

5.3 Temperature leakage Simulations

Equations (5.26)–(5.28) provide a fast method to predict the contamination in the recovered B -mode power spectrum for a given set of systematics and a specified scan strategy. However in deriving these equations a number of approximations were made. In particular, our derivation assumes that the systematics contribute to the polarisation leakage only to first order in the size of the systematic. I also assumed that the effect of the scan strategy in mitigating the systematic can be modelled as a simple damping of the power spectrum and therefore does not couple multiple temperature ℓ -modes on to a single B -mode scale. In this section, I demonstrate that equations (5.26)–(5.28)

5: OPTIMAL SCAN STRATEGIES FOR THE NEXT GENERATION OF CMB
POLARISATION SATELLITE EXPERIMENTS

Scan	<i>Planck</i>	WMAP	EPIC
Boresight angle (β)	85°	70°	50°
Precession angle (α)	7.5°	22.5°	45°
Spin period (T_{spin})	1 min	129 s	1 min
Precession period (T_{prec})	6 months	1 hr	3 hrs

Table 5.2: Observational parameters used to generate the scan strategies for the simulations described in Section 5.3. See Figure 5.5 for a diagram describing the parameters.

nevertheless provide an accurate prediction for the effect of the systematics on the B -mode power spectrum for a selection of scan strategies.

I create TOD simulations for two detector pairs, one “instrument- Q ” detector and one “instrument- U ” detector with different systematics. I consider the scan strategies adopted for the *Planck* (Planck Collaboration et al. 2011) and WMAP (Bennett et al. 2003) satellites. In addition, I consider the scan strategy suggested for the proposed EPIC satellite (Bock et al. 2009). The parameters used to model these scan strategies are listed in Table 5.2. The input signal for our simulations consists of a fiducial set of CMB power spectra with parameters: $\Omega_b=0.04612$, $\Omega_c = 0.233$, $\Omega_\Lambda=0.721$, $H_0=70$ $\text{kms}^{-1}\text{Mpc}^{-1}$ and $n_s=0.96$. An input tensor-to-scalar ratio of $r = 0.1$ was used for all simulations and a lensing B -mode contribution was included. In this chapter some of the results were obtained using HEALPIX² (Górski et al. 2005) and CAMB (Lewis & Challinor 2011).

In Fig. 5.2 I show the hit maps and maps of $|\tilde{h}_n|$ for $n = \{1, 2, 3, 4\}$ for one year of observations at a data sampling rate of 500 Hz at $N_{\text{side}}=2048$. The lower these h -values are, the better the scan strategy will be at mitigating different systematics. From equations (5.26)–(5.28) we can see that the average value of these maps acts a scaling factor for the leakage from temperature power spectrum to B -mode polarisation power spectrum.

For each scan strategy, I simulated the effects of each systematic (differential gain, pointing and ellipticity) individually assuming the parameters listed in Table 5.1. For all the simulations, except for the differential ellipticity simulations, a Gaussian beam

²See <http://healpix.sourceforge.net>

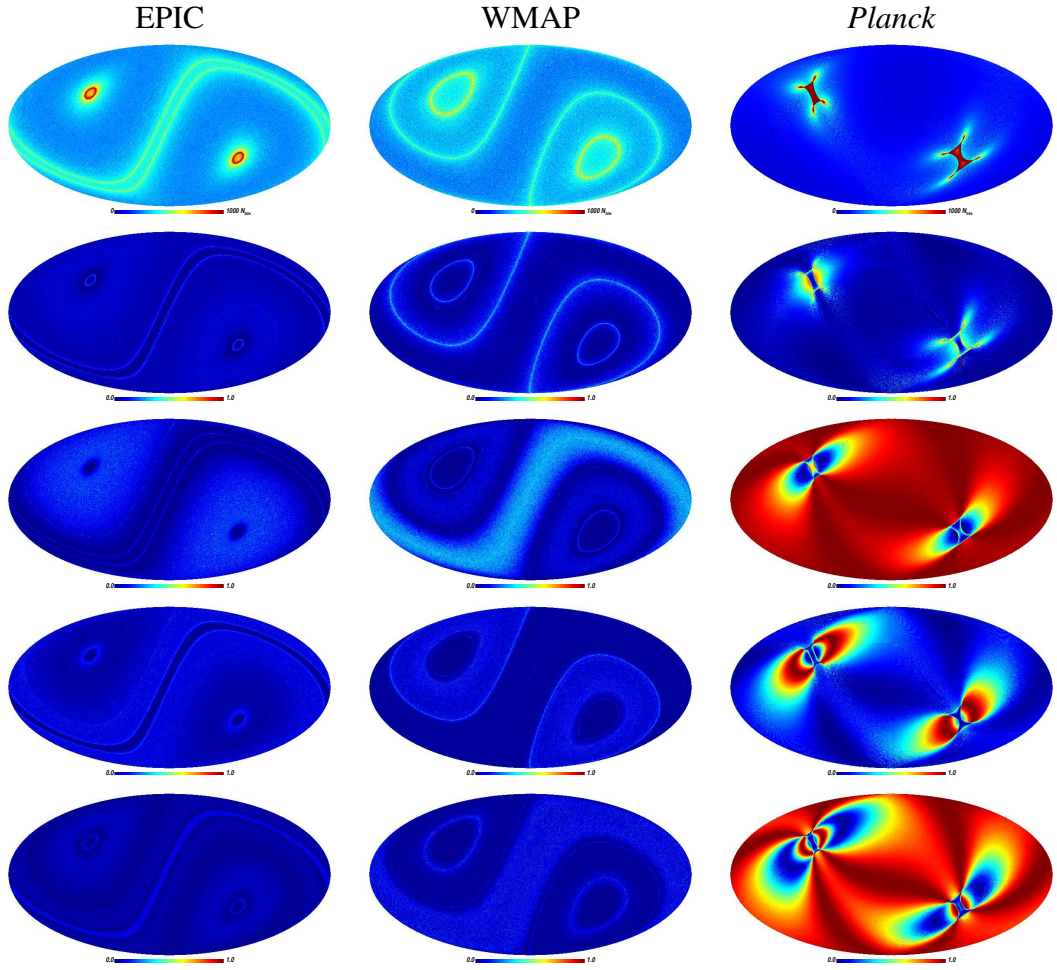


Figure 5.2: *Top row*: The hit maps for the EPIC (*left*), WMAP (*centre*) and Planck (*right*) scan strategies used in the simulations at $N_{\text{side}}=2048$. *Lower rows*: Maps of $|\tilde{h}_n|^2$, defined in Table 5.1, for $n = \{1, 2, 3, 4\}$, for the different scan strategies. The lower the value of $|\tilde{h}_n|^2$ the smaller the temperature to polarisation leakage is. It should be noted that in our formalism $\langle |\tilde{h}_2|^2 \rangle = \langle \cos(2\psi)^2 \rangle + \langle \sin(2\psi)^2 \rangle$ plotted in Bock et al. (2009).

with FWHM of 7 arcmin was used. To assess the differential ellipticity mitigation an elliptical Gaussian beam was used,

$$B(\theta, \phi) = \frac{1}{2\pi q\sigma^2} e^{-\frac{\theta^2}{2\sigma^2}(\cos^2\phi + q^{-1}\sin^2\phi)}. \quad (5.29)$$

In order to separately assess the impact of the two contributions to equation (5.28),

I run two sets of simulations. The effect described by the first term in equation (5.28) is simulated by each of the four detectors having a beam described by equation (5.29) with $q = 1.05$, but with the beam such that the ellipticity is rotated by $\pi/4$ with respect to the polarisation sensitivity direction. A beam of this type has the property that the second azimuthal mode of the spherical harmonic decomposition is imaginary. Such a setup will therefore strongly contribute a systematic of the type corresponding to the first term of equation (5.28). As both the “instrument- Q ” and “instrument- U ” detectors have the same differential ellipticity in this setup, there will be no systematic of the type corresponding to the second term in equation (5.28).

The second term of equation (5.28) is non-zero when the differential ellipticities within the two detector pairs are different. I create this effect by simulating both detectors within one pair to have a symmetric Gaussian beam of $\text{FWHM} = 7$ arcmin, while the detectors of the other pair are modelled as having elliptical beams, aligned with the polarization sensitivity direction, and described by equation (5.29). Both detectors in this latter pair are set up to have $\sigma = 3$ and $q = 1.05$ but for one of these, the beam is rotated by $\pi/2$ in order to create the required differential ellipticity.

The results from these simulations are shown in Fig. 5.3 and 5.4 in terms of the B -mode power spectrum recovered from Q and U maps which are constructed from the TOD using a simple binned map-making algorithm. I plot the recovered power spectrum for each of the systematics considered, and for each of the three scan strategies tested. In these figures, I have also plotted the theoretical predictions for the spurious signal from equations (5.26)–(5.28). We see that the theoretical predictions are accurate for $\ell \lesssim 1000$ which, for a beam of $\text{FWHM} = 7$ arcmin, is approaching the beam scale. The purpose of this plot is to show that the analytical predictions are consistent with the simulations, therefore, justifying their validity.

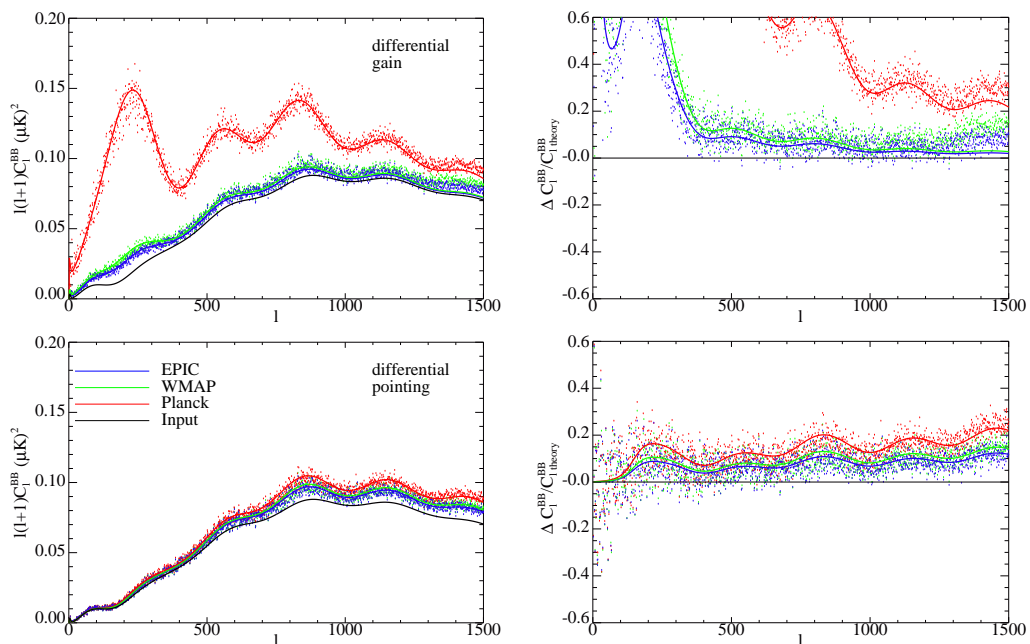


Figure 5.3: The recovered B -mode power spectrum from simulations including systematic effects when using the *Planck*, WMAP and EPIC scan strategies (shown in red, green and blue respectively). The points show the result for one simulation — see Section 5.3 for a full description. The left hand panels show the recovered power spectra and the right hand panels show the fractional bias. The simulations included differential gain of 1% (top row), differential pointing of 1.5% (second row). Also plotted are the predictions from equations (5.26)–(5.27) for the systematic effects showing good agreement with the simulated results. The purpose of this plot is test the validity of the predictions for the systematics, as a result, the in some cases the levels of the systematics were increased to examine the accuracy of the predictions. A tensor to scalar ratio of $r = 0.1$ was used in the simulations along with a fiducial CMB temperature power spectrum.

5.4 Scan Strategy Parameter Space

5.4.1 Scan strategy parameters

Having established the accuracy of equations (5.26)–(5.28) for a representative selection of scans, I now proceed to use these expressions to quantify the effectiveness of the scan strategy to mitigate leakage as a function of the observational parameters that define it.

The model I adopt to describe a satellite scan uses five parameters. Firstly, the

5: OPTIMAL SCAN STRATEGIES FOR THE NEXT GENERATION OF CMB POLARISATION SATELLITE EXPERIMENTS

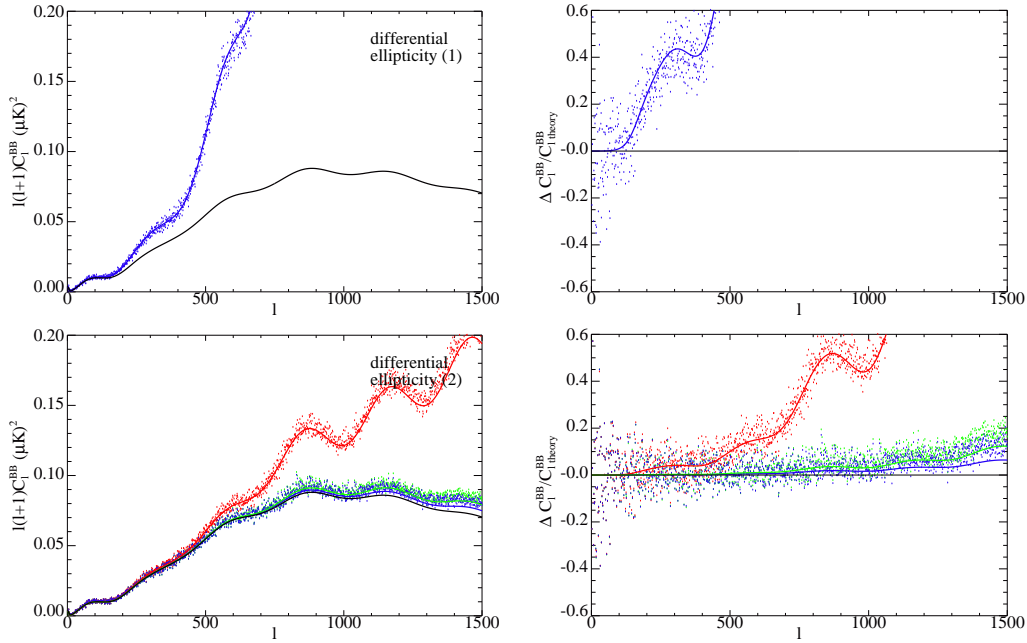


Figure 5.4: The same as for Fig. 5.3, for simulations that include differential ellipticity of 5% in both detector pairs (top row, to test the first term of equation (5.28)), and differential ellipticity in only one detector pair (bottom row, to test the second term in equation (5.28)). Note that the spurious B -mode produced by the effect corresponding to the first term in equation (5.28) is independent of the scan strategy. I, therefore, plot the result from just one simulation in the third row of panels.

telescope will spin about the major axis of the satellite. I denote the time period of this rotation as T_{spin} . The boresight of the telescope will be an angle to the spin axis which I call β . This spin axis is then allowed to precess around an axis. I choose this precession axis to be the extended line passing through the Sun and the Earth, presuming that the satellite is placed at the second Lagrange point (L2) of the Earth-Sun system. This arrangement therefore allows the telescope to be facing away from the Sun as much as possible. The angle between the spin axis and the precession axis is denoted by α , and the time period for the precession is T_{prec} . A schematic diagram of this set up is shown in Fig. 5.5. Finally, the satellite will sample the sky at a frequency of f_{samp} .

At first glance this seems to suggest that there are five free parameters to describe the scan strategy. However there are a number of additional constraints one may wish to enforce. The first and most obvious constraint is that the telescope must observe the

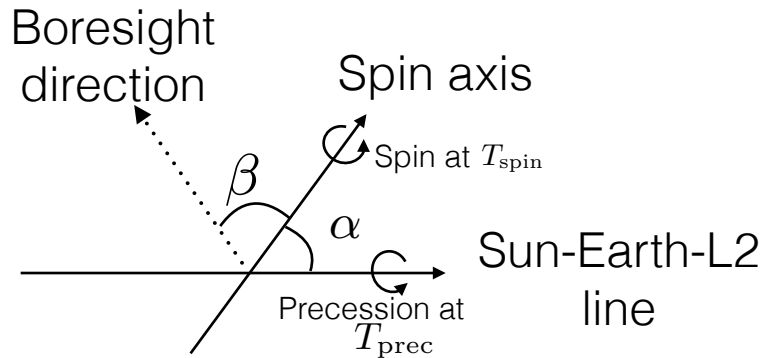


Figure 5.5: Schematic diagram to define the parameters used to define the scan strategies.

entire sky. This requires that

$$\alpha + \beta > 90^\circ. \quad (5.30)$$

Further constraints arise from considering the spin rate of the telescope. One can envisage three potential constraints. Firstly, one may wish to ensure that neighbouring rings on the sky are mapped sequentially. As the telescope spins, it maps out a ring of radius β on the sky. The precession of the telescope means that the next ring will be displaced from the preceding one. One may then wish to ensure that the spatial separation of sequential rings is less than some maximum separation which may be chosen to be e.g. a fraction of the beam width, or a fraction of the field of view. Such a constraint would then allow for continuous mapping of the sky. This requirement places an upper bound on the ratio $T_{\text{spin}}/T_{\text{prec}}$ of

$$\frac{T_{\text{spin}}}{T_{\text{prec}}} < \frac{\theta_{\perp}}{2\pi \sin \alpha}, \quad (5.31)$$

where θ_{\perp} is the desired separation of sequentially mapped rings.

A second consideration that impacts the choice of T_{spin} is the potential requirement

that the scan speed is fast enough such that the large scale modes in the sky are not confused with gain drifts in the detector creating $1/f$ noise. The noise power spectra of detectors are in general not white. They can often be modelled by the sum of a white component and an additional $1/f$ component that becomes important on long time scales. The transition point is often termed the knee frequency of the $1/f$ noise, f_{knee} . Delabrouille et al. (1998) investigated the impact of scan strategies on the resulting noise of a map when considering $1/f$ noise, here I make a simple criteria on T_{spin} . I require that a particular scale of interest on the sky (ℓ_{min}) appears in the timestream at least a factor of F in frequency higher than f_{knee} , this places a upper bound on the value of T_{spin} :

$$T_{\text{spin}} < \frac{2\ell_{\text{min}} \sin \beta}{F f_{\text{knee}}}. \quad (5.32)$$

In this chapter I set $\ell_{\text{min}} = 2$, $f_{\text{knee}} = 0.01$ Hz, consistent with a slight improvement of the *Planck* 143 GHz detector (Planck HFI Core Team et al. 2011) and $F = 2$.

Bolometers, as well as performing poorly on large time scales as described above, also suffer if the signal varies on too small a time scale. Bolometers require a finite amount of time to respond a change incoming radiation. The response of the bolometer, d to a sudden impulse of power as a function of time, t , is,

$$d(t) \propto e^{-t/\tau}, \quad (5.33)$$

where τ is the time constant of the detector (Delabrouille et al. 1998). It is desirable, therefore, to ensure that the telescope scans slow enough such that the telescope pointing only moves a fraction, p , of the beam FWHM, θ_{FWHM} in a time τ . This places a lower bound on the spin period,

$$T_{\text{spin}} > \frac{2\pi\tau \sin \beta}{p\theta_{\text{FWHM}}}. \quad (5.34)$$

If I set $\tau = 1$ ms consistent with the *Planck* CMB channels (Planck HFI Core Team

et al. 2011), $p = 1/4$ and $\theta_{\text{FWHM}} = 5.0$ arcmin then this places lower bound a factor 10 below the upper bound created by avoiding $1/f$ noise.

Finally, I require that the sampling frequency f_{samp} must be fast enough so that the beam width is fully sampled. I quantify this by requiring that the telescope must not move further than some fraction of the beam width, W , between samples. This translates to a lower bound on the sampling frequency of,

$$f_{\text{samp}} > \frac{2\pi \sin \beta}{W\theta_{\text{FWHM}}T_{\text{spin}}}, \quad (5.35)$$

In this chapter I set $W = 1/4$.

5.4.2 Practical constraints on scan strategies

In addition to the science-driven requirements detailed above, one also needs to consider a number of practical constraints which also limit the possible scan strategy parameter values.

Due to computing considerations, large values of T_{spin} are easier to implement in our scan-strategy simulations, as the higher spin periods lead to larger sampling frequencies, this leads to more pointings to calculate. In the following work I therefore choose T_{spin} to be the largest allowed value, given the chosen joint constraints on it and the other parameters. Additionally, given that higher sampling rates are problematic from the point of view of data transfer considerations, in all of our simulations I choose the lowest possible value of f_{samp} given the constraint of equation (5.35).

One practical constraint that must be considered when choosing a scan strategy is the required fuel to maintain the precession. The required torque to maintain a gyroscopic precession is

$$\tau = I_{zz}\omega_{\text{prec}}\omega_{\text{spin}} \sin \alpha, \quad (5.36)$$

where I_{zz} is the moment of inertia of the telescope about the spin axis, $\omega_{\text{prec}} = 2\pi/T_{\text{prec}}$

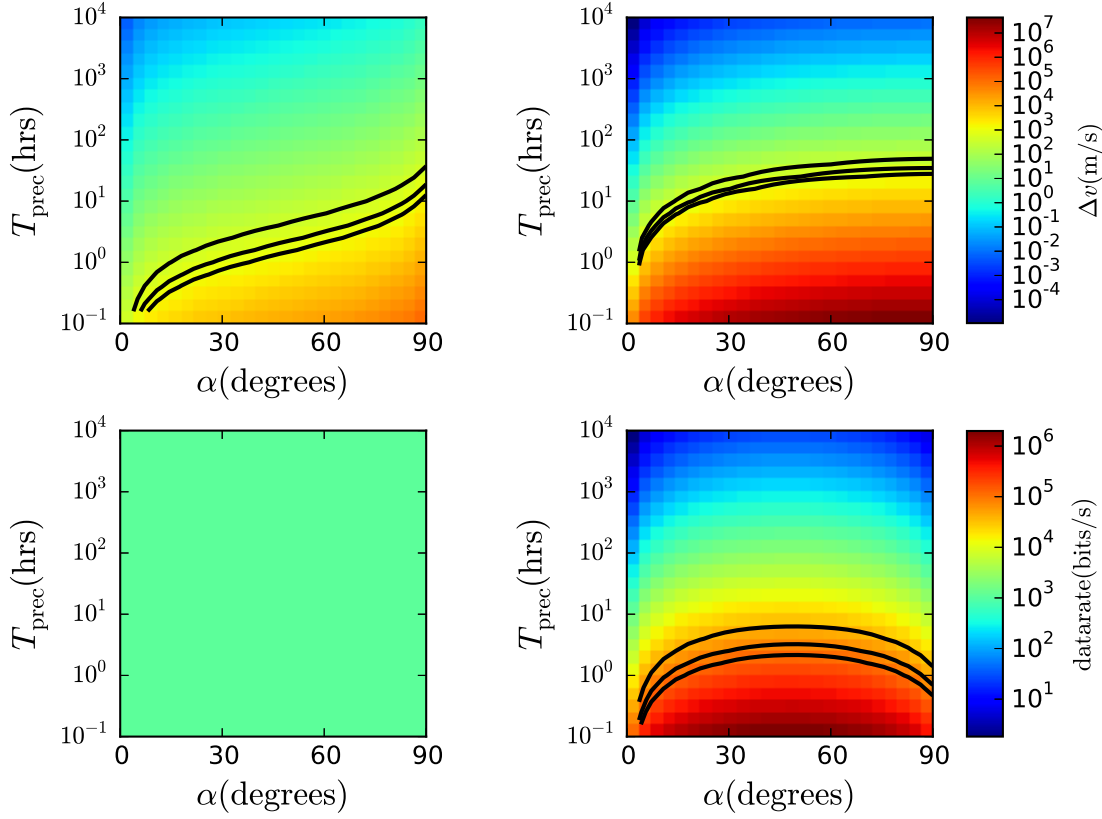


Figure 5.6: *Upper panels:* I plot the required impulse to maintain the scan strategies as a function of the scan parameters. In the left panel, I have used the T_{spin} constraint from equation (5.32). The panel on the right shows the result when the constraint from equation (5.31) is used. Overplotted are contours of $\Delta v = 500, 1000, 1500$ m/s to show reasonable impulse values. *Lower panels:* I plot the data rate per detector requirements given the required sampling frequency. I have used the T_{spin} constraint from equation (5.32) on the left and the constraint from equation (5.31) on the right. See Section 5.4.2 for details. Overplotted are contours of data rate = 50, 100, 150 kbits/s to show reasonable data rate per detector values.

is the angular velocity of the precession and $\omega_{\text{spin}} = 2\pi/T_{\text{spin}}$ is the angular velocity of the telescope spin (Feynman 1977; Markley et al. 2002). This leads to a total velocity impulse of

$$\Delta v = \int dt \frac{\tau}{M_{\text{sat}} R_{\text{lever}}} \quad (5.37)$$

$$= \frac{\tau T_{\text{mission}}}{M_{\text{sat}} R_{\text{lever}}}, \quad (5.38)$$

where M_{sat} is the mass of the satellite, R_{lever} is the distance of the rocket from the spin axis and T_{mission} is the lifetime of the mission. In the upper panels of Fig. 5.6 I plot the required impulsion for a telescope using typical values for an experiment, $I_{zz} = 2000 \text{ kg m}^2$, $M_{\text{sat}} = 2000 \text{ kg}$, $R_{\text{lever}} = 3 \text{ m}$ and $T_{\text{mission}} = 3 \text{ yrs}$. I show the results for a range of T_{prec} and α values and I have set $\alpha + \beta = 95^\circ$ in all cases.

I present results on the required impulsion for two cases. The first is the case where T_{spin} is chosen such that it meets the requirement on contiguous mapping (equation 5.31) where I set $\theta_{\perp} = 3 \text{ arcmin}$. The second is for the case where T_{spin} is chosen according to the requirement to limit the impact of low frequency $1/f$ detector noise (equation 5.32). For this latter case, I set $\ell_{\text{min}} = 2$, $F = 2$ and $f_{\text{knee}} = 0.01 \text{ Hz}$.

The second major practical concern is the implications that different scan strategies have for the required data rate. Higher sampling frequencies obviously require a faster data transfer to the earth. The required data rate per detector is simply dependant on the sampling frequency,

$$\text{datarate} = N_b f_{\text{samp}}, \quad (5.39)$$

where N_b is the assumed number of bits per sample, which I choose to be 8. In the lower panels of Fig. 5.6 I present the required data rate per detector as a function of T_{prec} and α . As for the investigation of the required impulsion discussed above, I present the results for two possible ways of choosing T_{spin} , according to either equation (5.31) or equation (5.32).

For comparison I also plot contours of “reasonable values” of impulsion and data rate. Euclid will require a data rate of 10 Mbits/s (Laureijs 2009), therefore, assuming there are 1000 detectors on board and assuming a factor of 10 increase in a future experiments data rate, a reasonable data rate per detector is 100 kbits/s. I therefore plot contours of data rate = 50, 100, 150 kbits/s.

The telescope pointing with respect to the Sun is also of significant importance. To minimise far sidelobe pick up of the Sun the telescope must never be pointed too

close to the sun. For this reason I have set $\alpha + \beta = 95^\circ$. This means our telescope never points closer than 85° . However, the Sun's influence can also place constraints on α itself. As α is the angle between the spin axis and the Sun-Earth line, large values of α mean the Sun will be shining on the side of the telescope at a more acute angle. Therefore, large values of α must also be accommodated with more effective heat shielding. Solar panels are often placed on the base of the telescope, the large values of α create a less efficient angle for the solar panels with respect to the sun. Therefore, a more sophisticated set up for the solar panels maybe required.

The results from this assessment of practical considerations suggest that a large fraction of parameter space is, in practice, infeasible. The reader should therefore bear in mind Fig. 5.6 when interpreting the results, displayed in Fig. 5.8, regarding the impact of different scan strategies on mitigating systematics which I now go on to discuss.

5.4.3 Error on the B -mode polarisation power spectrum

The analysis of Section 5.2 provides a rapid method to predict the error on the recovered B -mode polarisation power spectrum due to certain systematic errors and given certain features of the scan strategy. I have additionally developed a fast scan strategy simulation code that calculates the pointing and orientation of the telescope with respect to North for a given set of scan strategy parameters over 1 year of observations. This pointing information can then be used to calculate the $\langle |\tilde{h}_n|^2 \rangle$ values for that particular set of scan strategy parameters. The calculated values can then be used to predict the error on the recovered B -mode power spectrum using equations (5.26)–(5.28).

In Fig. 5.7 I plot the $\langle |\tilde{h}_n|^2 \rangle$ values as a function of the scan strategy parameters, α and T_{prec} . In all cases, I have overplotted the positions of the *Planck*, WMAP and EPIC scan strategies on the grid for reference. In implementing the scan strategies for each point in the $\{\alpha-T_{\text{prec}}\}$ parameter space, I have made a number of choices for

the values of the other observational parameters. These choices were motivated by the considerations outlined in Section 5.4.1. Firstly, I have set $\alpha + \beta = 95^\circ$. I have checked that this choice has little impact on the results within $\pm 5^\circ$. It simply translates the shape of the plots. I therefore choose the angle sum to be similar to other scan strategies in the literature. In particular, both the *Planck* and WMAP scan strategies have $\alpha + \beta = 92.5^\circ$ whilst the proposed EPIC scan strategy has the sum equalling 95° .

I chose the value of T_{spin} such that it satisfies the requirement of equation (5.32). As before, I set $\ell_{\text{min}} = 2$, $F = 2$ and $f_{\text{knee}} = 0.01$ Hz. When the constraint of equation (5.31) was used, for $T_{\text{prec}} \lesssim 10^2$ hrs, the $\langle |\tilde{h}_n|^2 \rangle$ values showed no discernible change, applying this constraint to higher values of T_{prec} would be ill-advised due to the low spin periods and the subsequent increase in noise due to $1/f$ noise. The unchanged h -values are expected because in both cases, $T_{\text{spin}} \ll T_{\text{prec}}$ in both cases. Finally, I have chosen f_{samp} such that it fulfils the requirement of equation (5.35), for a $\theta_{\text{FWHM}} = 5$ arcmin beam.

From equations (5.26)–(5.28) one can see that the lower the values of $\langle |\tilde{h}_n|^2 \rangle$ the smaller the temperature to polarisation leakage is for a particular systematic error in the experiment. $\langle |\tilde{h}_2|^2 \rangle$ is important for mitigating differential gain, $\langle |\tilde{h}_1|^2 \rangle$ and $\langle |\tilde{h}_3|^2 \rangle$ are important for mitigating differential pointing, and finally $\langle |\tilde{h}_4|^2 \rangle$ is important for mitigating the difference between the differential ellipticity. The results of Fig. 5.7 show that the choice of T_{prec} has little impact on the $\langle |\tilde{h}_n|^2 \rangle$ values unless $T_{\text{prec}} \gtrsim 20$ hours. This can be understood by considering the other timescales in the problem. With $T_{\text{prec}} \lesssim 20$ hours then $T_{\text{spin}} \ll T_{\text{prec}} \ll 1$ year meaning that this would have little effect on the quality of the scan strategy. If the value of T_{prec} is too large then the scan strategy cannot observe the entire sky in 1 year, shown in white in Fig. 5.7.

Fig. 5.7 does show, however, that the precession angle, α , has a significant impact on the quality of the scan strategy. A smaller boresight angle (β) will result in the satellite scanning in smaller circles. Given the constraint $\alpha + \beta = 95^\circ$, a smaller value of β corresponds to a larger precession angle α . Scanning in smaller circles generally creates a larger range of orientations for each pixel and thus improves the quality of the

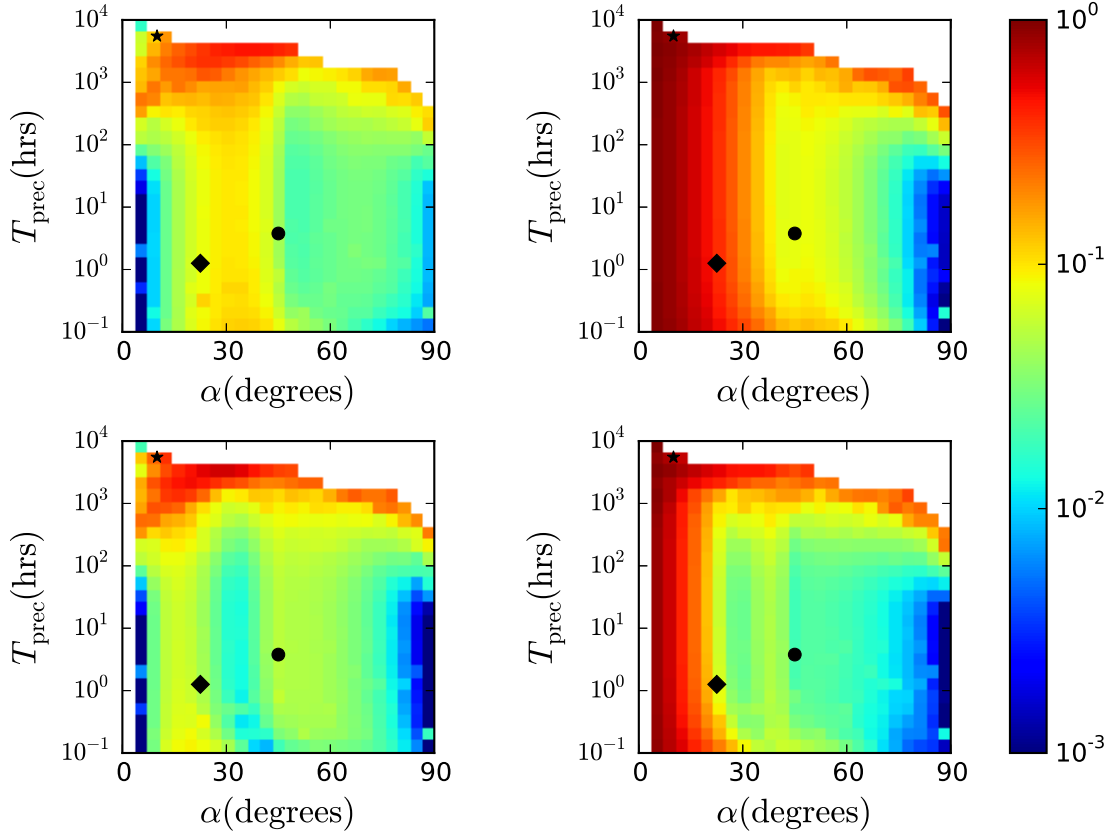


Figure 5.7: I plot the values of $\langle |\tilde{h}_n|^2 \rangle$, used in equations (5.26)–(5.28) as a function of the scan strategy parameters. The $\langle |\tilde{h}_n|^2 \rangle$ values for $n = \{1, 2, 3, 4\}$ are displayed in the top left, top right, lower left and lower right panels respectively. The lower the value of $\langle |\tilde{h}_n|^2 \rangle$ the smaller the temperature to polarisation leakage is for a particular systematic error in the experiment. $\langle |\tilde{h}_2|^2 \rangle$ is important for mitigating differential gain, $\langle |\tilde{h}_1|^2 \rangle$ and $\langle |\tilde{h}_3|^2 \rangle$ are important for mitigating differential pointing, and finally $\langle |\tilde{h}_4|^2 \rangle$ is important for mitigating the difference between the differential ellipticity. White regions show areas where the entire sky is not observed in 1 year. In each panel, I indicate the positions of the *Planck*, WMAP and EPIC scan strategies with a star, diamond and circle, respectively.

scan strategy by lowering the $\langle |\tilde{h}_n|^2 \rangle$ values, where n is even. When n is odd scanning in larger circles results in a small range of orientation angles. However six months later the scan is flipped, creating a symmetry that renders the odd terms close to zero. This symmetry is enhanced when the range of orientation angles is small, creating a deep valley in the $\langle |\tilde{h}_1|^2 \rangle$ and $\langle |\tilde{h}_3|^2 \rangle$ values at $\alpha \approx 5^\circ$.

Using equations (5.26)–(5.28) one can translate the $\langle |\tilde{h}_n|^2 \rangle$ surfaces of Fig. 5.7 into estimates of the resulting error on the recovered B -mode power spectrum. To do this, one must make some assumptions regarding the levels of the systematics to include in the calculations. I use typical values for these types of systematics as found in the BICEP2 experiment instrumental systematics paper (BICEP2 Collaboration et al. 2015) except for differential gain. Satellite-based missions can use the CMB dipole to calibrate the bolometers, therefore, obtaining much lower levels of differential gain, of order 0.2% (Planck Collaboration et al. 2015b). Specifically, I choose a differential gain of 0.2%, a differential pointing of 2% and a differential ellipticity of 5%. To present my results, I calculate the average fractional bias in the recovered B -mode polarisation power spectrum for two wide multipole bins. I choose one bin to cover the range $2 \leq \ell \leq 201$ to assess the ability to recover an inflationary B -mode signal on large scales. The other bin I consider covers the range $801 \leq \ell \leq 1000$ in order to assess the ability to recover the lensing B -mode power spectrum. The results are presented in Fig. 5.8. This figure clearly shows, as described before, that the dominant parameter in mitigating temperature-to- B -mode polarisation leakage is the precession angle α , once $T_{\text{prec}} \ll 1$ year: as α increases the spurious signal induced in the B -mode polarisation power spectrum reduces dramatically.

It should be noted that our method for predicting the temperature-to- B -mode leakage provides one with a worst case scenario as I have only considered an experiment with two pairs of detectors. In a real experiment, the leakage from each detector pair will be different and in certain situations the leakage from different detector pairs could be completely uncorrelated. This would result in the overall leakage averaging to a lower value. The differential gain between detector pairs is unlikely to be correlated. However, the effects of differential pointing and differential ellipticity could conceivably be a function of the position of the detector pair in the focal plane and/or imperfections in the primary lens or mirror of the telescope. Such a scenario would result in the leakage from different detector pairs being correlated and hence not averaging to an overall lower value.

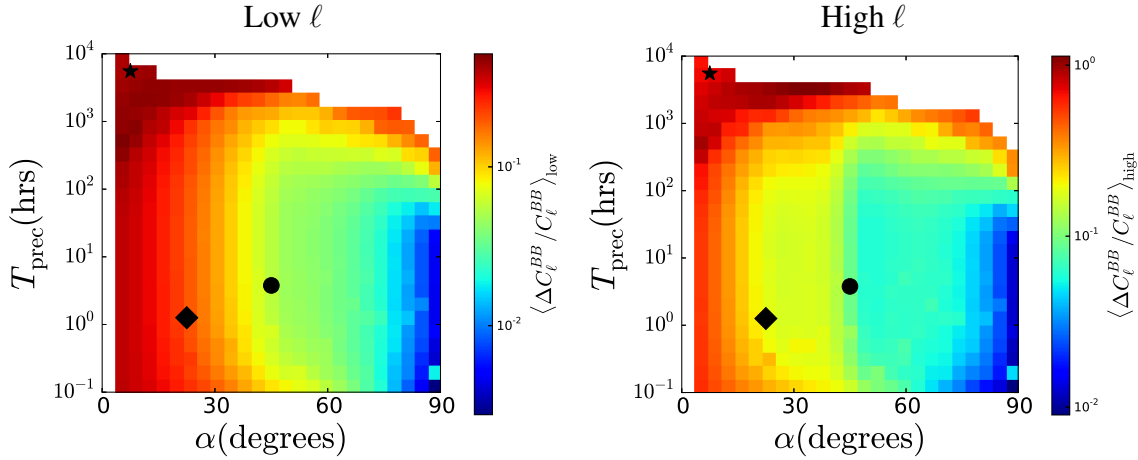


Figure 5.8: *Left panel:* The fractional error on the recovered B -mode polarisation power spectrum, averaged over the range $2 \leq \ell \leq 201$, as a function of the scan strategy parameters. This multipole range corresponds to the scales where an inflationary B -mode signal is most likely to be discovered. The assumed tensor-to-scalar ratio is 0.1. A differential gain of 0.2%, a differential pointing of 2% and a differential ellipticity in one detector of 5% aligned with the polarisation sensitivity was assumed. *Right panel:* The same as the left panel but for a multipole range $801 \leq \ell \leq 1000$ in order to probe the angular scales where the lensing B -mode power spectrum peaks. Note that the morphology of the two plots are the same but the amplitude is different. White regions show areas where the entire sky is not observed in 1 year. In each panel, I indicate the positions of the *Planck*, WMAP and EPIC scan strategies with a star, diamond and circle, respectively.

5.5 Discussion and Conclusions

The CMB B -mode power spectrum is approximately four orders of magnitude fainter than the CMB temperature power spectrum. Any instrumental imperfections that couple temperature fluctuations to B -mode polarisation must therefore be carefully controlled and/or removed. In this chapter I have investigated the role that a scan strategy can have in mitigating certain common systematics by averaging the error down with many crossing angles. In Section 5.2, I presented approximate analytical forms for the error on the recovered B -mode power spectrum that would result from differential gain, pointing and ellipticity if two detector pairs are used in a polarisation experiment. By minimising the h -values (\tilde{h}_n , see Table 5.1), of the scan strategy using mul-

multiple crossing angles, certain types of systematic effects can be averaged down. The different spins of the systematic effects mean that different h -values are relevant for mitigating different types of systematic effects.

By examining equations (5.26)–(5.28) one can see that since differential gain is a spin-0 systematic effect, it is therefore suppressed by a factor $\langle |\tilde{h}_2|^2 \rangle$, where the average is over all the pixels in the scan. Differential pointing is spin-1 and is therefore suppressed by factors involving $\langle |\tilde{h}_1|^2 \rangle$ and $\langle |\tilde{h}_3|^2 \rangle$. Differential ellipticity can couple temperature fluctuations to B -mode polarisation in two ways: the first term in equation (5.28) is independent of the scan strategy and therefore if present, it will always result in spurious B -mode polarisation regardless of the scan strategy. This has been shown a number of times before (O’Dea et al. 2007; Shimon et al. 2008; Wallis et al. 2014). If the orientation of the differential ellipticity is parallel or perpendicular to the polarisation sensitivity direction then the coupling from temperature will be of a pure E -mode form. Any misalignment and there will be also be coupling to B -mode polarisation. The second term of equation (5.28) models the effect due to a difference in the differential ellipticity between two pairs of detectors. This effect couples temperature fluctuations to both E - and B -modes and can be mitigated with an appropriate scan strategy through the $\langle |\tilde{h}_4|^2 \rangle$ term.

In Section 5.3, I used simulations to calculate the error on the B -mode power spectrum, shown in Fig. 5.3 and 5.4, for three example scan strategies. The larger precession angles and smaller boresight angles of the WMAP and EPIC scans reduce the even h -values and are therefore better at mitigating differential gain and differential ellipticity as compared to the *Planck* scan. The faster precession periods of the WMAP and EPIC scans reduce the odd h -values and are therefore better at mitigating differential pointing as well. In terms of future searches for inflationary B -modes, our study suggests that differential gain is potentially the most problematic effect as it affects lower ℓ ranges.

Based on the validation by simulations in Section 5.3 as well as the pseudo- C_ℓ -based argument presented in Appendix B.1, I can be confident in using the analytic

predictions for the error on the B -mode polarisation power spectrum of Section 5.2. In Section 5.4 I combine the analytic analysis with a fast scan strategy simulation code to search the scan strategy parameter space for the optimal scan strategy. A key result is Fig. 5.7 where we have presented the $\langle |\tilde{h}_n|^2 \rangle$ values for a range of satellite scan strategy parameters.

My main conclusions are as follows: (i) as long as $T_{\text{spin}} \ll T_{\text{prec}} \ll 1$ year the exact values of the time scales are unimportant for mitigating systematics by multiple crossing angles. (ii) the main parameters of interest are the precession angle (α) and the boresight angle (β). By lowering β and increasing α the scan strategy will make smaller circles on the sky. These small circles are beneficial for creating a wide range of orientation angles and are therefore effective in mitigating several of the systematic effects that I have considered. This is demonstrated in Fig. 5.8 where I plot the potential impact on the recovered B -mode polarisation power spectrum. For the particular levels of systematic effects that I have assumed, I find little difference in our preferred scan strategy regardless of whether one chooses to target the inflationary B -mode signal on large angular scales or the lensing B -mode signal on smaller scales.

The focus of this work has been to identify the effect the choice of scan strategy parameters has on the mitigation of time independent systematic effects. There are many other requirements that places constraints on the scan strategy, some of which are discussed in Section 5.4.2. One area that has not been considered in this work how quickly the scan maps the sky. By avoiding pointing too close to the Sun, a particular scan strategy cannot map the full sky faster than once every six months. However, different scan strategies can map half the sky at different speeds. Having multiple independent maps of the sky helps greatly with identifying and removing many time dependant systematic effects. With $\alpha, \beta \approx 45^\circ$ half the sky can be mapped without requiring that the Earth rotates around the Sun. Lower values of T_{prec} and T_{spin} will then map the half sky faster, providing more independent maps over the course of the mission. This desire to acquire multiple maps of the same area of sky, therefore, leads to faster spinning and precession then this study into time independent systematic

effects suggests is necessary. Furthermore, larger values of β allows the telescope to observe variation due to the CMB dipole over the course of one spin period. This known signal allows one to constantly calibrate the bolometers resulting in much more accurate maps. This technique was used extensively by the *Planck* experiment (Planck Collaboration et al. 2015b).

*5: OPTIMAL SCAN STRATEGIES FOR THE NEXT GENERATION OF CMB
POLARISATION SATELLITE EXPERIMENTS*

Chapter 6

Conclusions and Future Work

The CMB B -mode polarisation contains key information about the origin and evolution of the universe. The very earliest times can be probed using the large scale B -mode polarisation power spectrum. No other probe can concretely measure the energy scale of inflation. This large scale B -mode polarisation, if detected, will not only confirm and constrain inflation models, but will also be a direct detection of gravitational waves.

The small scale B -mode polarisation also tells us about the large scale structure of the universe. E -mode polarisation is shifted on the sky but not rotated by gravitational potentials between us and the surface of last scattering. This shifting of the E -mode polarisation breaks the even parity relation it normally has creating B -mode polarisation. By measuring the small B -mode polarisation we can probe the evolution of large scale structure of the universe.

It is needless to say, but there has therefore, been a large international effort to detect this powerful cosmological signal. The practical challenges in making this vital detection are major obstacle to overcome. The small scale B -mode polarisation power spectrum is only just becoming detectable using thousands of near photon-noise limited detectors. The large scale B -mode polarisation remains elusive. With that said, the sheer sensitivity required to make these detections only scratches the surface, Galactic foreground emission from synchrotron radiation and hot spinning dust confuses the

matter further. Not only will we need many detectors but we will also need many frequency bands to disentangle the CMB from Galactic foregrounds. Further to this we need the detectors and telescope in general to be almost perfect in design. The B -mode polarisation sits side-by-side with temperature fluctuations, whose power spectra differ by four orders of magnitude or greater. This means that any coupling between the two must be greatly controlled and/or removed. This thesis has attempted to make significant steps in the control and removal of systematic effects.

6.1 Pseudo- C_ℓ estimator

Pseudo- C_ℓ techniques have been used to remove the mode-mode coupling when making measurements of the CMB power spectra with limited sky coverage. Hanson et al. (2010) looked at using a pseudo- C_ℓ technique to remove any bias generated by using an asymmetric beam when estimating the temperature power spectrum. Chapter 3 extended this work to polarisation, allowing one to make unbiased estimates of the CMB polarisation power spectrum for a general scan strategy and a general beam shape.

The pseudo- C_ℓ removes any temperature to polarisation leakage as a result of the asymmetry, as well as polarisation to polarisation coupling. This method, like most pseudo- C_ℓ techniques, removes the mean over many CMB realisations of the leakage. Therefore, the error bars on the recovered B -mode power spectrum will have increased by an amount proportional to the leakage, due to cosmic variance. The technique also requires the beam shape as an input. Measuring beam shapes is problematic and itself suffers from measurement error.

6.2 Map-making algorithms

Given the limitations of using a pseudo- C_ℓ method to remove systematic errors in CMB power spectrum estimation, I set about investigating map-making algorithms to achieve the same result. Chapter 3 presents a map-making algorithm capable of making maps

free of beam asymmetry bias from a single detector. For a temperature experiment the algorithm is simple. Using many crossing angles one can separate out the different spin components that make up the signal gathered on one pixel. The spin-0 component will be the temperature field convolved with the axisymmetric component of the beam. The other spin components will be the temperature field convolved with the high azimuthal modes of the beam spherical harmonic decomposition. This technique could be applied to the summed timestream in a differencing experiment.

One can also apply this technique to make maps of temperature and polarisation from a single detector. This follows the same pattern: one must separate out the different spin components of the detected signal, the spin-0 being temperature and the spin-2 being polarisation. In doing this though we have left the temperature to polarisation leakage that comes about because of the asymmetry of the temperature beam. Therefore, Chapter 3 requires a second stage where one must calculate the temperature to polarisation leakage using the temperature map and the beam shape and then remove it from the polarisation maps.

In Chapter 4 I extend this map making algorithm further. I apply the ideas of separating out the different spins of the detected signal of a pixel to a differencing experiment. In this type of experiment two detectors, sensitive to orthogonal polarisation directions, are used to make polarisation maps by differencing the timestreams to remove the temperature response of the two detectors. If there are any differences in the temperature responses of the two detectors then temperature fluctuations will leak in to the polarisation maps. The map making algorithm separates out the systematic errors that could cause such a leakage and the polarisation by separating the spins of the systematic effects and that of polarisation.

Chapter 4 also crucially looks at the benefit of using a HWP to increase polarisation angle coverage. If a HWP is placed at the end of the optical chain in emission, then the HWP will simply rotate the polarisation sensitivity of the detectors, keeping the systematic errors constant. This can be used to disentangle the spin-2 leakage from temperature to polarisation due differential ellipticity of the two detectors and the spin-

2 polarisation signal.

Using a HWP to create polarisation angle coverage can allow one to separate the systematic errors and the polarisation signal, even if the angle coverage of each pixel is small. By modelling the summed effect of the systematic errors with Legendre polynomials, I show in Chapter 4 one can also make maps free of temperature to polarisation leakage.

Having developed these algorithms and shown their effectiveness on simulated data I would like to apply them to real data. At the time of writing a proposal is being made to the European Space Agency (ESA) for a future CMB polarisation space mission. Controlling systematic errors will be a crucial part of the data analysis. These techniques could be useful in that endeavour. In the immediate future, the WMAP scan strategy should provide enough orientation angles of each pixel suitable for the algorithms presented here to be useful. It would be interesting to see how the algorithms developed in this thesis stand up to WMAP data.

6.3 Scan strategy investigation

Chapters 3 and 4 concentrated on developing techniques to remove systematic effects. Ultimately it would be beneficial to be able to design an experiment that was free of such systematic errors. Chapter 5 is a step in that direction. By designing a scan strategy that observes each sky pixel at many orientation angles systematic effects that vary with a different spin to that of polarisation can be mitigated. I derive approximate equations capable of predicting the temperature to polarisation leakage for a number of systematic effects, given knowledge of the orientation angle coverage of the scan strategy.

Using a fast scan strategy simulation code I developed, along with the analytic equations I was able to calculate the error on the recovered B -mode power spectrum for a range of scan strategies caused by a number of time independent systematic effects. This work allows one to very easily assess the relative importance of each scan strategy

parameter on systematic effect mitigation.

In order to make the scan strategies under consideration close to reasonable some simple constraints were placed on the parameters that define the scan. These made simple cut offs to avoid unwanted degradation of the resulting data. For example bolometers become unstable over long time scales, this instability creates increased noise on large scales in the resulting map. To avoid this problem fast scanning across the sky is required. In this analysis we placed a simple lower bound on scan speed to attempt to avoid this problem, however, a more detailed analysis would be beneficial. In future work I hope to extend and improve this analysis with respect to time dependent experiment imperfections.

ESA is currently calling for mission proposals. The CMB community is currently writing a range of papers in preparation for this proposal. The work presented in Chapter 5 is currently being extended to aid the choice the scan strategy for CORe+.

6: CONCLUSIONS AND FUTURE WORK

Appendix A

Pseudo- C_ℓ estimator

A.1 Relationship between our pseudo- C_ℓ and the standard pseudo- C_ℓ

Here I show that the pseudo- C_ℓ expression derived in Section 3.3 reduces to a rewriting of the standard polarised pseudo- C_ℓ presented in Brown et al. (2005), in the case where the beam is axisymmetric and where the experiment has both instrument- Q and instrument- U detectors. I begin by looking at the coupling kernel,

$$K_{m_1 k_1 m_2 k_2}^{\ell_1 \ell_2} \equiv \int d^3\omega D_{m_1 k_1}^{\ell_1}(\omega) D_{m_2 k_2}^{\ell_2*}(\omega) W(\omega) n(\omega). \quad (\text{A.1})$$

I use the weighting function $n(\omega)$ to apodise the hit map and apply a galactic mask. While, in general, it can be a function of θ , ϕ and ψ , in practice, it is sufficient for it to be a function of just θ and ϕ . It should be chosen such that $\int d\psi W(\omega) n(\theta, \phi)$ ranges from 0 to 1 and acts as the standard window function in the pseudo- C_ℓ . The requirement that the experiment has both an instrument- Q and - U detector means that for every orientation of the telescope ω we have 4 detections of the sky each at $[\theta, \phi, \psi + j\pi/4]$, where $j=0, 1, 2, 3$. A consequence of this arrangement of detectors is that

A: PSEUDO- C_ℓ ESTIMATOR

$$\int d\psi W(\omega) e^{ik\psi} = 0 \quad \text{for } k = \pm 2, \pm 4. \quad (\text{A.2})$$

Therefore $K_{m_1 k_1 m_2 k_2}^{\ell_1 \ell_2} = 0$ if $k_1 - k_2 = \pm 2, \pm 4$. I can now examine the Wigner decomposition of the time stream, in particular the $k=0, \pm 2$ components, as these will contain information on the temperature and polarisation of the CMB. I also assume the beam to be axisymmetric and have a zero cross polar response, so that $b_{s\ell k} = 0$ for $s \neq -k$. I make this assumption in order to make the connection with the standard pseudo- C_ℓ approach. Applying these constraints to equation (3.18) we get,

$$T_{m_1 0}^{\ell_1 *} = \sum_{\ell_2 m_2} b_{0\ell_2 0}^* a_{0\ell_2 m_2} K_{m_1 0 m_2 0}^{\ell_1 \ell_2} \quad (\text{A.3})$$

$$T_{m_1 \pm 2}^{\ell_1 *} = \sum_{\ell_2 m_2} b_{\mp 2\ell_2 \pm 2}^* a_{\mp 2\ell_2 m_2} K_{m_1 \pm 2 m_2 \pm 2}^{\ell_1 \ell_2}. \quad (\text{A.4})$$

Using these expressions, one can show that E - and B -mode-like decompositions (equations 3.33 & 3.34) of the TOD in this experiment will be,

$$\begin{aligned} T_{m_1 E}^{\ell_1 *} &= \sum_{\ell_2 m_2} b_{-2\ell_2 2}^* \left(a_{\ell_2 m_2}^E K_{\ell_1 \ell_2 m_1 m_2}^+ + a_{\ell_2 m_2}^B K_{\ell_1 \ell_2 m_1 m_2}^- \right) \\ T_{m_1 B}^{\ell_1 *} &= \sum_{\ell_2 m_2} b_{-2\ell_2 2}^* \left(a_{\ell_2 m_2}^B K_{\ell_1 \ell_2 m_1 m_2}^+ - a_{\ell_2 m_2}^E K_{\ell_1 \ell_2 m_1 m_2}^- \right), \end{aligned} \quad (\text{A.5})$$

where I have defined,

$$K_{\ell_1 \ell_2 m_1 m_2}^+ \equiv -\frac{1}{2} \left(K_{m_1 2 m_2 2}^{\ell_1 \ell_2} + K_{m_1 -2 m_2 -2}^{\ell_1 \ell_2} \right) \quad (\text{A.6})$$

$$K_{\ell_1 \ell_2 m_1 m_2}^- \equiv \frac{i}{2} \left(K_{m_1 2 m_2 2}^{\ell_1 \ell_2} - K_{m_1 -2 m_2 -2}^{\ell_1 \ell_2} \right). \quad (\text{A.7})$$

Comparing the expressions of equation (A.5) with equation (10) of Brown et al. (2005) shows that the E - and B -mode-like decompositions of the TOD defined in equations (3.33) & (3.34) have a similar form to the E - and B -mode decompositions of a polarisation map used in the standard pseudo- C_ℓ technique. They are similar in the sense that they are both the sky polarisation smoothed with the beam, and then convolved with a window function. They differ only in normalisation factors. As the decompositions are similar, the pseudo- C_ℓ constructed from them will also be similar.

A.2 Product of two coupling kernels

I require the product of two coupling kernels. In order to calculate this, we start from the definition of the Kernel

$$K_{m_1 k_1 m_2 k_2}^{\ell_1 \ell_2} \equiv \int d^3 \omega D_{m_1 k_1}^{\ell_1}(\omega) D_{m_2 k_2}^{\ell_2*}(\omega) W(\omega) n(\omega) \quad (\text{A.8})$$

$$= \sum_{\ell_3 m_3 k_3} w_{m_3 k_3}^{\ell_3} \int d^3 \omega D_{m_1 k_1}^{\ell_1}(\omega) D_{m_2 k_2}^{\ell_2*}(\omega) D_{m_3 k_3}^{\ell_3}(\omega) \quad (\text{A.9})$$

$$= 8\pi^2 (-1)^{m_2+k_2} \sum_{\ell_3 m_3 k_3} w_{m_3 k_3}^{\ell_3} \begin{pmatrix} \ell_1 & \ell_2 & \ell_3 \\ m_1 & -m_2 & m_3 \end{pmatrix} \begin{pmatrix} \ell_1 & \ell_2 & \ell_3 \\ k_1 & -k_2 & k_3 \end{pmatrix}, \quad (\text{A.10})$$

where the second equality comes from an identity found in Varshalovich et al. (1988).

I can now evaluate the product summed over certain indices m_1 , and m_2

A: PSEUDO- C_ℓ ESTIMATOR

$$M_{k_1 k'_1 k_2 k_3}^{\ell_1 \ell_2} \equiv \sum_{m_1 m_2} K_{m_1 k_1 m_2 k_2}^{\ell_1 \ell_2} K_{m_1 k'_1 m_2 k_3}^{\ell_1 \ell_2^*} \quad (\text{A.11})$$

$$\begin{aligned} &= 64\pi^4 (-1)^{k_2+k_3} \sum_{\substack{m_1 m_2 \\ \ell_4 m_4 k_4 \\ \ell_5 m_5 k_5}} w_{m_4 k_4}^{\ell_4} w_{m_5 k_5}^{\ell_5^*} \begin{pmatrix} \ell_1 & \ell_2 & \ell_4 \\ m_1 & -m_2 & m_4 \end{pmatrix} \begin{pmatrix} \ell_1 & \ell_2 & \ell_4 \\ k_1 & -k_2 & k_4 \end{pmatrix} \\ &\quad \times \begin{pmatrix} \ell_1 & \ell_2 & \ell_5 \\ m_1 & -m_2 & m_5 \end{pmatrix} \begin{pmatrix} \ell_1 & \ell_2 & \ell_5 \\ k'_1 & -k_3 & k_5 \end{pmatrix}. \quad (\text{A.12}) \end{aligned}$$

The Wigner $3j$ orthogonality relation is

$$\sum_{m_1 m_2} \begin{pmatrix} \ell_1 & \ell_2 & \ell_4 \\ m_1 & m_2 & m_4 \end{pmatrix} \begin{pmatrix} \ell_1 & \ell_2 & \ell_5 \\ m_1 & m_2 & m_5 \end{pmatrix} = \frac{1}{2\ell_4 + 1} \delta_{\ell_4, \ell_5} \delta_{m_4, m_5}, \quad (\text{A.13})$$

which enables the sum over m_1 and m_2 to be performed and evaluating the Kronecker δ gives

$$M_{k_1 k'_1 k_2 k_3}^{\ell_1 \ell_2} = 64\pi^4 (-1)^{k_2+k_3} \sum_{\ell_4 m_4 k_4 k_5} w_{m_4 k_4}^{\ell_4} w_{m_4 k_5}^{\ell_4^*} \frac{1}{2\ell_4 + 1} \begin{pmatrix} \ell_1 & \ell_2 & \ell_4 \\ k_1 & -k_2 & k_4 \end{pmatrix} \begin{pmatrix} \ell_1 & \ell_2 & \ell_4 \\ k'_1 & -k_3 & k_5 \end{pmatrix}. \quad (\text{A.14})$$

One can simplify this further by defining the window correlation matrix $\mathcal{W}_{k_1, k_2}^\ell \equiv \frac{1}{2\ell+1} \sum_m w_{mk_1}^\ell w_{mk_2}^{\ell^*}$. Also one can use the selection rule in the $3j$ symbols that states that the sum of the bottom row must be equal to zero for the symbol to be non-zero. This gives us

$$\begin{aligned}
M_{k_1 k'_1 k_2 k_3}^{\ell_1 \ell_2} &= 64\pi^4 (-1)^{k_2+k_3} \sum_{\ell_4 k_4 k_5} \mathcal{W}_{k_4, k_5}^{\ell_4} \begin{pmatrix} \ell_1 & \ell_2 & \ell_4 \\ k_1 & -k_2 & k_4 \end{pmatrix} \\
&\quad \times \begin{pmatrix} \ell_1 & \ell_2 & \ell_4 \\ k'_1 & -k_3 & k_5 \end{pmatrix} \delta_{k_4, k_2-k_1} \delta_{k_5, k_3-k'_1} \\
&= 64\pi^4 (-1)^{k_2+k_3} \sum_{\ell_4} \mathcal{W}_{k_2-k_1, k_3-k'_1}^{\ell_4} \begin{pmatrix} \ell_1 & \ell_2 & \ell_4 \\ k_1 & -k_2 & k_2-k_1 \end{pmatrix} \\
&\quad \times \begin{pmatrix} \ell_1 & \ell_2 & \ell_4 \\ k'_1 & -k_3 & k_3-k'_1 \end{pmatrix}.
\end{aligned} \tag{A.15}$$

A.3 Symmetries in $M_{k_1 k'_1 k_2 k_3}^{\ell_1 \ell_2}$

The symmetries in the matrix $M_{k_1 k'_1 k_2 k_3}^{\ell_1 \ell_2}$ are important to reduce the computation time. First I look at swapping the indices k_2 and k_3 along with k_1 and k'_1 :

$$\begin{aligned}
M_{k'_1 k_1 k_3 k_2}^{\ell_1 \ell_2} &= 64\pi^4 (-1)^{k_2+k_3} \sum_{\ell_4} \mathcal{W}_{k_3-k'_1, k_2-k_1}^{\ell_4} \begin{pmatrix} \ell_1 & \ell_2 & \ell_4 \\ k'_1 & -k_3 & k_3-k'_1 \end{pmatrix} \\
&\quad \times \begin{pmatrix} \ell_1 & \ell_2 & \ell_4 \\ k_1 & -k_2 & k_2-k_1 \end{pmatrix} \\
&= 64\pi^4 (-1)^{k_2+k_3} \sum_{\ell_4} \mathcal{W}_{k_2-k_1, k_3-k'_1}^{\ell_4*} \begin{pmatrix} \ell_1 & \ell_2 & \ell_4 \\ k_1 & -k_2 & k_2-k_1 \end{pmatrix} \\
&\quad \times \begin{pmatrix} \ell_1 & \ell_2 & \ell_4 \\ k_1 & -k_3 & k_3-k'_1 \end{pmatrix} \\
&= M_{k_1 k'_1 k_2 k_3}^{\ell_1 \ell_2*},
\end{aligned} \tag{A.16}$$

A: PSEUDO- C_ℓ ESTIMATOR

where I have used the definition of window correlation matrix to say that $\mathcal{W}_{k_2, k_1}^\ell = \mathcal{W}_{k_1, k_2}^{\ell*}$. Now I look at the reversing the sign of all k_i . This implies that

$$\begin{aligned}\mathcal{W}_{-k_1, -k_2}^\ell &= \frac{1}{2\ell + 1} \sum_m w_{m-k_1}^\ell w_{m-k_2}^{\ell*} \\ &= \frac{1}{2\ell + 1} \sum_m (-1)^{m+k_1} w_{-m-k_1}^{\ell*} (-1)^{m+k_1} w_{-m-k_2}^\ell \\ &= (-1)^{k_1+k_2} \mathcal{W}_{k_1, k_2}^{\ell*}.\end{aligned}\tag{A.17}$$

Now I can show symmetry in the matrix M is given by

$$\begin{aligned}M_{-k_1-k'_1, -k_2-k'_2}^{\ell_1 \ell_2} &= 64\pi^2 (-1)^{k_2+k_3} \sum_{\ell_4} \mathcal{W}_{-k_2+k_1, -k_3+k'_1}^{\ell_4} \begin{pmatrix} \ell_1 & \ell_2 & \ell_4 \\ -k_1 & +k_2 & -k_2+k_1 \end{pmatrix} \\ &\quad \times \begin{pmatrix} \ell_1 & \ell_2 & \ell_4 \\ -k'_1 & +k_3 & -k_3+k'_1 \end{pmatrix} \\ &= 64\pi^4 (-1)^{k_2+k_3} \sum_{\ell_4} (-1)^{k_2-k_1+k_3-k'_1} \mathcal{W}_{k_2-k_1, k_3-k'_1}^{\ell_4*} \begin{pmatrix} \ell_1 & \ell_2 & \ell_4 \\ k_1 & -k_2 & k_2-k_1 \end{pmatrix} \\ &\quad \times \begin{pmatrix} \ell_1 & \ell_2 & \ell_4 \\ k'_1 & -k_3 & k_3-k'_1 \end{pmatrix} \\ &= (-1)^{k_2-k_1+k_3-k'_1} M_{k_1 k'_1 k_2 k_3}^{\ell_1 \ell_2*},\end{aligned}\tag{A.18}$$

where in the second equality I have used the relation

$$\begin{pmatrix} \ell_1 & \ell_2 & \ell_3 \\ m_1 & m_2 & m_3 \end{pmatrix} \begin{pmatrix} \ell_1 & \ell_2 & \ell_3 \\ m'_1 & m'_2 & m'_3 \end{pmatrix} = \begin{pmatrix} \ell_1 & \ell_2 & \ell_3 \\ -m_1 & -m_2 & -m_3 \end{pmatrix} \begin{pmatrix} \ell_1 & \ell_2 & \ell_3 \\ -m'_1 & -m'_2 & -m'_3 \end{pmatrix}.\tag{A.19}$$

A.4 Explicit form of the coupling operator

In section 3.3.3 I use the coupling operator $O_{i_1 i_2}$. Here we explicitly write it in terms of the sub operators $O_{\ell_1 \ell_2}^{k_1 k'_1 s_1 s_2}$

$$\mathbf{O}_{ij} = \begin{pmatrix} O_{\ell_1 \ell_2}^{0000} & O_{\ell_1 \ell_2}^{0002} & O_{\ell_1 \ell_2}^{000-2} & O_{\ell_1 \ell_2}^{0022} & O_{\ell_1 \ell_2}^{002-2} & O_{\ell_1 \ell_2}^{00-2-2} \\ O_{\ell_1 \ell_2}^{0200} & O_{\ell_1 \ell_2}^{0202} & O_{\ell_1 \ell_2}^{020-2} & O_{\ell_1 \ell_2}^{0222} & O_{\ell_1 \ell_2}^{022-2} & O_{\ell_1 \ell_2}^{00-2-2} \\ O_{\ell_1 \ell_2}^{0-200} & O_{\ell_1 \ell_2}^{0-202} & O_{\ell_1 \ell_2}^{0-20-2} & O_{\ell_1 \ell_2}^{0-222} & O_{\ell_1 \ell_2}^{0-22-2} & O_{\ell_1 \ell_2}^{0-2-2-2} \\ O_{\ell_1 \ell_2}^{2200} & O_{\ell_1 \ell_2}^{2202} & O_{\ell_1 \ell_2}^{220-2} & O_{\ell_1 \ell_2}^{2222} & O_{\ell_1 \ell_2}^{222-2} & O_{\ell_1 \ell_2}^{22-2-2} \\ O_{\ell_1 \ell_2}^{2-200} & O_{\ell_1 \ell_2}^{2-202} & O_{\ell_1 \ell_2}^{2-20-2} & O_{\ell_1 \ell_2}^{2-222} & O_{\ell_1 \ell_2}^{2-22-2} & O_{\ell_1 \ell_2}^{2-2-2-2} \\ O_{\ell_1 \ell_2}^{-2-200} & O_{\ell_1 \ell_2}^{-2-202} & O_{\ell_1 \ell_2}^{-2-20-2} & O_{\ell_1 \ell_2}^{-2-222} & O_{\ell_1 \ell_2}^{-2-22-2} & O_{\ell_1 \ell_2}^{-2-2-2-2} \end{pmatrix} \quad (\text{A.20})$$

A.5 Relations between $C_{\ell}^{ss'}$ and C_{ℓ}^{XY}

The following matrix operation allows conversion from $C_{\ell}^{ss'}$ to C_{ℓ}^{XY} ,

$$\begin{pmatrix} C_{\ell}^{TT} \\ C_{\ell}^{TE} \\ C_{\ell}^{TB} \\ C_{\ell}^{EE} \\ C_{\ell}^{EB} \\ C_{\ell}^{BB} \end{pmatrix} = \begin{pmatrix} 1 & 0 & 0 & 0 & 0 & 0 & 0 \\ 0 & -1/2 & -1/2 & 0 & 0 & 0 & 0 \\ 0 & i/2 & -i/2 & 0 & 0 & 0 & 0 \\ 0 & 0 & 0 & 1/4 & 1/4 & 1/4 & 1/4 \\ 0 & 0 & 0 & -i/4 & i/4 & -i/4 & i/4 \\ 0 & 0 & 0 & -1/4 & -1/4 & 1/4 & 1/4 \end{pmatrix} \begin{pmatrix} C_{\ell}^{00} \\ C_{\ell}^{02} \\ C_{\ell}^{0-2} \\ C_{\ell}^{22} \\ C_{\ell}^{2-2} \\ C_{\ell}^{-22} \\ C_{\ell}^{-2-2} \end{pmatrix} \quad (\text{A.21})$$

The matrix is not square, this does not imply that there is more information in the right than the left. There are the same number of degrees of freedom on both sides because $C_{\ell}^{2-2} = C_{\ell}^{-22}$.

A: PSEUDO- C_ℓ ESTIMATOR

Appendix B

Pseudo- C_ℓ approach to calculating the temperature leakage

B.1 Error on the B -mode polarisation power spectrum

In Section 5.2 I have made an assumption about the way in which the scan strategy impacts on the leaked B -mode power spectrum. Specifically, I assumed that the effect of mitigation by the scan strategy can be approximated as a simple suppression of the leaked signal by the relevant $\langle |\tilde{h}_n| \rangle$ value (see Section 5.2) and that the direction of the leaked polarisation would mean half of the power is of an E -mode form and the other half is B -mode form. This approximation allowed us to derive a relatively simple set of equations to describe the temperature-to- B -mode polarisation power spectrum leakage. This simple set of equations was essential to quickly predict the leaked B -mode power spectrum for any given scan strategy as I did in Section 5.4. Here I examine this approximation further and derive an exact analytical form for the leaked B -mode power spectrum for the case of differential gain. With this exact equation I can examine the approximation further.

I start from equation (5.20) which describes the leakage in the polarisation map due to differential gain. I begin by defining the spherical harmonic modes of the CMB

temperature field and of the differential gain as suppressed by the scan strategy:

$$\tilde{a}_{\ell m}^T = \int d\Omega {}_0Y_{\ell m}^*(\Omega) T^B(\Omega), \quad (\text{B.1})$$

$$H_{\ell m}^{\pm 2} = \int d\Omega {}_{\pm 2}Y_{\ell m}^*(\Omega) \frac{1}{2}(\delta g_1 \pm i\delta g_2)\tilde{h}_{\pm 2}(\Omega). \quad (\text{B.2})$$

I am interested in working out the error on the B -mode power spectrum. I, therefore, calculate the decomposition of the leaked polarisation in terms of spin weighted spherical harmonics,

$${}_2\tilde{a}_{\ell_1 m_1} = \int d\Omega {}_2Y_{\ell_1 m_1}^*(\Omega) \Delta P^g(\Omega), \quad (\text{B.3})$$

$${}_{-2}\tilde{a}_{\ell_1 m_1} = \int d\Omega {}_{-2}Y_{\ell_1 m_1}^*(\Omega) \Delta P^{g*}(\Omega). \quad (\text{B.4})$$

Substituting these into our expression for ΔP^g , we find

$${}_{\pm 2}\tilde{a}_{\ell_1 m_1} = \int d\Omega {}_{\pm 2}Y_{\ell_1 m_1}^*(\Omega) \frac{1}{2}(\delta g_1 \pm i\delta g_2)\tilde{h}_{\pm 2}(\Omega)T^B(\Omega). \quad (\text{B.5})$$

I now substitute the spherical harmonic decomposition of the smoothed temperature field to find

$${}_{\pm 2}\tilde{a}_{\ell_1 m_1} = \int d\Omega {}_{\pm 2}Y_{\ell_1 m_1}^*(\Omega) \frac{1}{2}(\delta g_1 \pm i\delta g_2)\tilde{h}_{\pm 2}(\Omega) \sum_{\ell_2 m_2} \tilde{a}_{\ell_2 m_2}^T {}_0Y_{\ell_2 m_2}(\Omega) \quad (\text{B.6})$$

$$= \sum_{\ell_2 m_2} K_{m_1 m_2}^{\pm \ell_1 \ell_2} \tilde{a}_{\ell_2 m_2}^T, \quad (\text{B.7})$$

where I have defined the coupling kernel,

$$K_{m_1 m_2}^{\pm \ell_1 \ell_2} = \int d\Omega {}_{\pm 2}Y_{\ell_1 m_1}^*(\Omega) \frac{1}{2}(\delta g_1 \pm i\delta g_2)\tilde{h}_{\pm 2}(\Omega) {}_0Y_{\ell_2 m_2}(\Omega). \quad (\text{B.8})$$

We can now calculate the error on the recovered B -mode power spectrum. I start with

the error on the measured B -mode power spectrum,

$$\Delta\tilde{C}_{\ell_1}^{BB} = \frac{1}{2\ell_1 + 1} \sum_{m_1} \tilde{a}_{\ell_1 m_1}^B \tilde{a}_{\ell_1 m_1}^{B*} \quad (\text{B.9})$$

$$= \frac{1}{4(2\ell_1 + 1)} \sum_{m_1} (\tilde{a}_{\ell_1 m_1}^2 - \tilde{a}_{\ell_1 m_1}^{-2}) (\tilde{a}_{\ell_1 m_1}^2 - \tilde{a}_{\ell_1 m_1}^{-2})^* \quad (\text{B.10})$$

$$= \frac{1}{4(2\ell_1 + 1)} \sum_{\substack{m_1 \\ \ell_2 m_2 \\ \ell_2' m_2'}} [K_{m_1 m_2}^{+ \ell_1 \ell_2} \tilde{a}_{\ell_2 m_2}^T K_{m_1 m_2'}^{+ \ell_1 \ell_2'} \tilde{a}_{\ell_2' m_2'}^{T*} \\ + K_{m_1 m_2}^{- \ell_1 \ell_2} \tilde{a}_{\ell_2 m_2}^T K_{m_1 m_2'}^{- \ell_1 \ell_2'} \tilde{a}_{\ell_2' m_2'}^{T*} + (K_{m_1 m_2}^{+ \ell_1 \ell_2} \tilde{a}_{\ell_2 m_2}^T K_{m_1 m_2'}^{- \ell_1 \ell_2'} \tilde{a}_{\ell_2' m_2'}^{T*} + \text{c.c.})], \quad (\text{B.11})$$

where the brackets denote the term to which the c.c. applies to. We can simplify this equation by requiring statistical isotropy of the CMB temperature field. This allows us to write $\tilde{a}_{\ell_1 m_1}^T \tilde{a}_{\ell_2 m_2}^{T*} = \delta_{\ell_1 \ell_2} \delta_{m_1 m_2} B_{\ell_1}^2 \langle C_{\ell_1}^T \rangle$, where B_ℓ is the temperature beam window function and $\langle \rangle$ denotes averaging over CMB realisations. Substituting this result into equation (B.11) and evaluating the Kronecker delta functions gives us

$$\langle \Delta\tilde{C}_{\ell_1}^{BB} \rangle = \frac{1}{4(2\ell_1 + 1)} \sum_{\substack{m_1 \\ \ell_2 m_2}} [K_{m_1 m_2}^{+ \ell_1 \ell_2} K_{m_1 m_2}^{+ \ell_1 \ell_2} + K_{m_1 m_2}^{- \ell_1 \ell_2} K_{m_1 m_2}^{- \ell_1 \ell_2} \quad (\text{B.12})$$

$$+ (K_{m_1 m_2}^{+ \ell_1 \ell_2} K_{m_1 m_2}^{- \ell_1 \ell_2} + \text{c.c.})] B_{\ell_2}^2 \langle C_{\ell_2}^{TT} \rangle \\ = \sum_{\ell_2} M_{\ell_1 \ell_2} B_{\ell_2}^2 \langle C_{\ell_2}^{TT} \rangle. \quad (\text{B.13})$$

To calculate the coupling operator we must first calculate a product of two coupling kernels. I do this in Section B.2. To calculate the error on the recovered B -mode power spectrum one must then deconvolve for the polarisation power spectrum. I assume that the temperature and polarisation beam window functions are the same. This gives us,

$$\langle \Delta C_{\ell_1}^{BB} \rangle = \frac{1}{B_{\ell_1}^2} \sum_{\ell_2} M_{\ell_1 \ell_2} B_{\ell_2}^2 \langle C_{\ell_2}^{TT} \rangle. \quad (\text{B.14})$$

As with all pseudo- C_ℓ coupling operators this matrix can be approximated by a diagonal matrix with values equal to the fraction of sky covered in the experiment. This

approximation best when the CMB power spectrum is close to constant. Here the equivalent to the sky fraction is simply the average of the modulus squared of the window function $\frac{1}{2}(\delta g_1 + i\delta g_2)\tilde{h}_2$. There is one difference in that half of the spurious polarisation power will be in a E -mode form and the other half in a B -mode form. Therefore we have that

$$M_{\ell_1\ell_2} \approx \frac{1}{8}|\delta g_1 + i\delta g_2|^2\langle|\tilde{h}_2|^2\rangle\delta_{\ell_1\ell_2}, \quad (\text{B.15})$$

With this approximation, equation (B.14) reduces to equation (5.26). In Fig. B.1 I show how well this approximation holds for realistic scan strategies. I plot the recovered B -mode power spectrum from simulations (as described in Section 5.3) assuming the *Planck*, WMAP and EPIC scan strategies and including a differential gain systematic error in each detector pair. I also plot the predictions for the biased B -mode power,

$$C_\ell^{BB \text{ rec}} = C_\ell^{BB \text{ true}} + \Delta C_\ell^{BB}. \quad (\text{B.16})$$

I plot two predictions for the biased power: one where the predicted error is of the simplified form of equation (5.26) and a second where the full coupling operator of equation (B.14) is used. The coupling operator based prediction is in excellent agreement with the simulations. However, it is also clear that the simplified formulae of Section 5.2 also provide a very good approximation over the multipole range of interest.

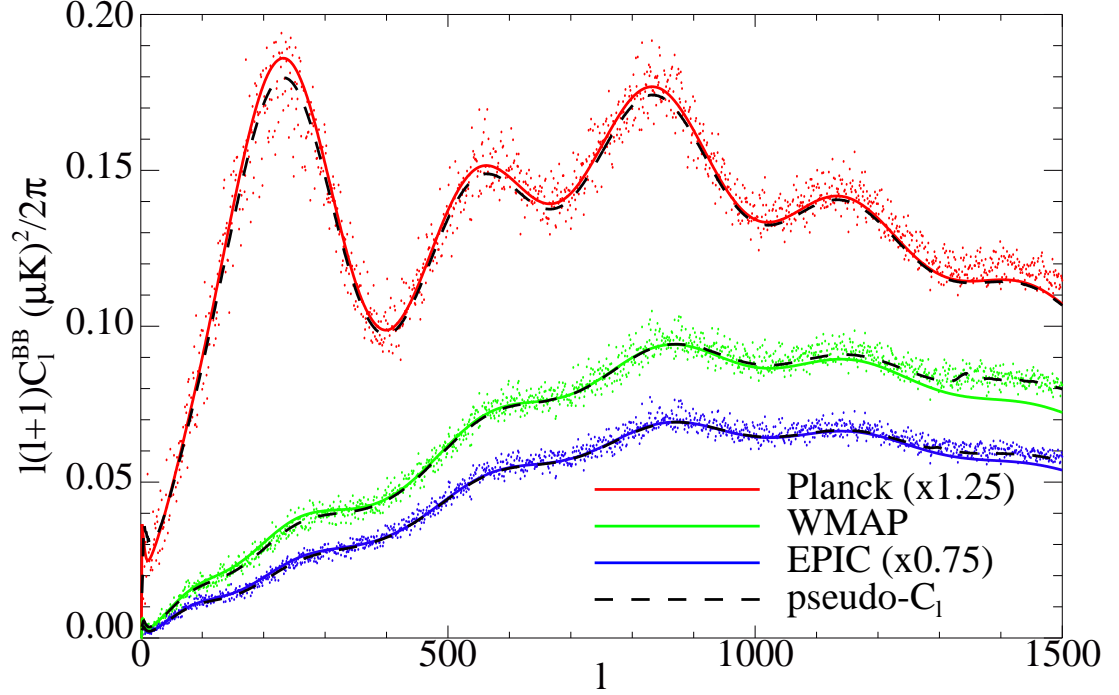


Figure B.1: The recovered B -mode power spectrum when a differential gain systematic error is present assuming the *Planck*, WMAP and EPIC scan strategies (shown in red, green and blue respectively). The points show the result for one simulation. The solid lines shows the predictions for the recovered power spectrum using the approximate model of equation (5.26). The black dashed line shows the predictions using the full coupling operator of equation (B.14). There is good agreement between the two predictions for $\ell \lesssim 1000$. This provides strong justification for using the simple equations of Section 5.2 to predict the error on the B -mode power spectrum in Section 5.4. The small disagreement between the pseudo- C_ℓ prediction for the systematic error high ℓ for the *Planck* simulation is a numerical artefact due to the simulation software.

B.2 Product of two coupling kernels

In Section B.1 we use the product of two coupling kernels. Here I calculate this product. The definition of the coupling kernel gives us,

$$K_{m_1 m_2}^{\pm \ell_1 \ell_2} = \int d\Omega \, {}_{\pm 2}Y_{\ell_1 m_1}^*(\Omega) \frac{1}{2}(\delta g_1 \pm i\delta g_2) \tilde{h}_{\pm 2}(\Omega) Y_{\ell_2 m_2}(\Omega), \quad (\text{B.17})$$

$$= \sum_{\ell_3 m_3} H_{\ell_3 m_3}^{\pm 2} \int d\Omega \, {}_{\pm 2}Y_{\ell_1 m_1}^*(\Omega) Y_{\ell_2 m_2}(\Omega) {}_{\pm 2}Y_{\ell_3 m_3}(\Omega), \quad (\text{B.18})$$

$$= \sum_{\ell_3 m_3} (-1)^{m_1} H_{\ell_3 m_3}^{\pm 2} \quad (\text{B.19})$$

$$\times \sqrt{F_{\ell_1 \ell_2 \ell_3}} \begin{pmatrix} \ell_1 & \ell_2 & \ell_3 \\ -m_1 & m_2 & m_3 \end{pmatrix} \begin{pmatrix} \ell_1 & \ell_2 & \ell_3 \\ \mp 2 & 0 & \pm 2 \end{pmatrix},$$

where the second equality comes from an identity found in Varshalovich et al. (1988), and I have defined,

$$F_{\ell_1 \ell_2 \ell_3} = \frac{(2\ell_1 + 1)(2\ell_2 + 1)(2\ell_3 + 1)}{4\pi}. \quad (\text{B.20})$$

We are now in a position to calculate the product of two coupling kernels,

$$\begin{aligned} \sum_{m_1 m_2} K_{m_1 m_2}^{\pm \ell_1 \ell_2} K_{m_1 m_2}^{\pm \ell_1 \ell_2 *} &= \sum_{\substack{m_1 m_2 \\ \ell_3 m_3 \\ \ell'_3 m'_3}} H_{\ell_3 m_3}^{\pm 2} H_{\ell'_3 m'_3}^{\pm 2*} \sqrt{F_{\ell_1 \ell_2 \ell_3}} \begin{pmatrix} \ell_1 & \ell_2 & \ell_3 \\ -m_1 & m_2 & m_3 \end{pmatrix} \begin{pmatrix} \ell_1 & \ell_2 & \ell_3 \\ \mp 2 & 0 & \pm 2 \end{pmatrix} \\ &\quad \times \sqrt{F_{\ell_1 \ell_2 \ell'_3}} \begin{pmatrix} \ell_1 & \ell_2 & \ell'_3 \\ -m_1 & m_2 & m'_3 \end{pmatrix} \begin{pmatrix} \ell_1 & \ell_2 & \ell'_3 \\ \mp 2 & 0 & \pm 2 \end{pmatrix}. \end{aligned} \quad (\text{B.21})$$

To simplify this result, we can use the orthogonality relation,

$$\sum_{m_1 m_2} \begin{pmatrix} \ell_1 & \ell_2 & \ell_3 \\ m_1 & m_2 & m_3 \end{pmatrix} \begin{pmatrix} \ell_1 & \ell_2 & \ell'_3 \\ m_1 & m_2 & m'_3 \end{pmatrix} = \frac{1}{2\ell_3 + 1} \delta_{\ell_3, \ell'_3} \delta_{m_3, m'_3}. \quad (\text{B.22})$$

Evaluating the Kronecker delta function leads to

$$\begin{aligned} \sum_{m_1 m_2} K_{m_1 m_2}^{\pm \ell_1 \ell_2} K_{m_1 m_2}^{\pm \ell_1 \ell_2 *} &= \sum_{\ell_3} F_{\ell_1 \ell_2 \ell_3} \mathcal{H}_{\ell_3}^{\pm \pm} \\ &\quad \times \begin{pmatrix} \ell_1 & \ell_2 & \ell_3 \\ \mp 2 & 0 & \pm 2 \end{pmatrix} \begin{pmatrix} \ell_1 & \ell_2 & \ell_3 \\ \mp 2 & 0 & \pm 2 \end{pmatrix}, \end{aligned} \quad (\text{B.23})$$

where I have defined the spin power spectrum of the window function,

$$\mathcal{H}_{\ell_3}^{\pm \pm} = \frac{1}{2\ell_3 + 1} \sum_{m_3} H_{\ell_3 m_3}^{\pm 2} H_{\ell_3 m_3}^{\pm 2*}. \quad (\text{B.24})$$

References

- Baumann, D., Jackson, M. G., Adshead, P., et al., 2009, in American Institute of Physics Conference Series, edited by Dodelson, S., Baumann, D., Cooray, A., et al., vol. 1141 of *American Institute of Physics Conference Series*, 10–120, arXiv:0811.3919
- Bennett, C. L., Halpern, M., Hinshaw, G., et al., 2003, *APJS*, 148, 1, astro-ph/0302207
- Bersanelli, M., Mennella, A., Morgante, G., et al., 2012, in Society of Photo-Optical Instrumentation Engineers (SPIE) Conference Series, vol. 8446 of *Society of Photo-Optical Instrumentation Engineers (SPIE) Conference Series*, 7, arXiv:1208.0164
- BICEP2 and Keck Array Collaborations, Ade, P. A. R., Ahmed, Z., et al., 2015, *ApJ*, 811, 126, arXiv:1502.00643
- BICEP2 Collaboration, Ade, P. A. R., Aikin, R. W., et al., 2014, *Physical Review Letters*, 112, 24, 241101, arXiv:1403.3985
- BICEP2 Collaboration, Ade, P. A. R., Aikin, R. W., et al., 2015, *ApJ*, 814, 110, arXiv:1502.00608
- BICEP2/Keck and Planck Collaborations, Ade, P. A. R., Aghanim, N., et al., 2015, *Physical Review Letters*, 114, 10, 101301, arXiv:1502.00612
- Bock, J., Aljabri, A., Amblard, A., et al., 2009, Study of the Experimental Probe of Inflationary Cosmology, arXiv:0906.1188
- Brown, M. L., Castro, P. G., Taylor, A. N., 2005, *MNRAS*, 360, 1262, astro-ph/0410394
- Brown, M. L., Challinor, A., North, C. E., Johnson, B. R., O’Dea, D., Sutton, D., 2009, *MNRAS*, 397, 634, arXiv:0809.4032
- Challinor, A., 2013, in *IAU Symposium*, edited by Burton, M. G., Cui, X., Tothill, N. F. H., vol. 288 of *IAU Symposium*, 42–52, arXiv:1210.6008

REFERENCES

- Challinor, A., Fosalba, P., Mortlock, D., Ashdown, M., Wandelt, B., Górski, K., 2000, *Phys. Rev. D*, 62, 12, 123002, astro-ph/0008228
- Challinor, A., Peiris, H., 2009, in *American Institute of Physics Conference Series*, edited by Novello, M., Perez, S., vol. 1132 of *American Institute of Physics Conference Series*, 86–140, arXiv:0903.5158
- Chandrasekhar, S., 1960, *Radiative transfer*
- Delabrouille, J., Gorski, K. M., Hivon, E., 1998, *MNRAS*, 298, 445, astro-ph/9710349
- Delabrouille, J., Puget, J.-L., Lamarre, J.-M., Gispert, R., 2000, *Astrophysical Letters and Communications*, 37, 259, astro-ph/9810478
- Dupac, X., Tauber, J., 2005, *A&A*, 430, 363, astro-ph/0409405
- Feynman, R., 1977, *Lectures on Physics Vol 1*, California Institute of Technology
- Goldberg, J. N., Macfarlane, A. J., Newman, E. T., Rohrlich, F., Sudarshan, E. C. G., 1967, *Journal of Mathematical Physics*, 8, 2155
- Górski, K. M., Hivon, E., Banday, A. J., et al., 2005, *ApJ*, 622, 759, astro-ph/0409513
- Hanson, D., Lewis, A., Challinor, A., 2010, *Phys. Rev. D*, 81, 10, 103003, arXiv:1003.0198
- Hivon, E., Górski, K. M., Netterfield, C. B., Crill, B. P., Prunet, S., Hansen, F., 2002, *ApJ*, 567, 2, astro-ph/0105302
- Hu, W., Hedman, M. M., Zaldarriaga, M., 2003, *Phys. Rev. D*, 67, 4, 043004, astro-ph/0210096
- Hu, W., White, M., 1997, *New Astronomy*, 2, 323, astro-ph/9706147
- Keihänen, E., Reinecke, M., 2012, *A&A*, 548, A110, arXiv:1208.1399
- Keisler, R., Hoover, S., Harrington, N., et al., 2015, *ApJ*, 807, 151, arXiv:1503.02315
- Laureijs, R., 2009, *Euclid Assessment Study Report for the ESA Cosmic Visions*, arXiv:0912.0914
- Lewis, A., Challinor, A., 2011, *CAMB: Code for Anisotropies in the Microwave Background*, *Astrophysics Source Code Library*, ascl:1102.026
- Liddle, A. R., 1999, *Proceedings of ICTP summer school in high-energy physics*, 1998, arXiv:9901124
- Liddle, A. R., Parsons, P., Barrow, J. D., 1994, *Phys. Rev. D*, 50, 7222, astro-ph/9408015
- LSPE Collaboration, Aiola, S., Amico, G., et al., 2012, in *Society of Photo-Optical*

- Instrumentation Engineers (SPIE) Conference Series, vol. 8446 of *Society of Photo-Optical Instrumentation Engineers (SPIE) Conference Series*, arXiv:1208.0281
- Ludwig, A. C., 1973, *IEEE Transactions on Antennas and Propagation*, 21, 116
- Markley, F. L., Andrews, S. F., O'Donnell, J. R., Ward, D. K., Ericsson, A. J., 2002, 5th International Conference on Dynamics and Control of Systems and Structures in Space
- Mitra, S., Rocha, G., Górski, K. M., et al., 2011, *APJS*, 193, 5, arXiv:1005.1929
- Naess, S., Hasselfield, M., McMahan, J., et al., 2014, *JCAP*, 10, 007, arXiv:1405.5524
- O'Dea, D., Challinor, A., Johnson, B. R., 2007, *MNRAS*, 376, 1767, astro-ph/0610361
- Oliver, A. D., Clarricoats, P. J. B., Kishk, A. A., Shafai, L., 1994, *Microwave Horns and Feeds*
- Padin, S., Staniszewski, Z., Keisler, R., et al., 2008, *Applied Optics*, 47, 4418
- Planck Collaboration, Adam, R., Ade, P. A. R., et al., 2014a, accepted by *A&A*, arXiv:1409.5738
- Planck Collaboration, Adam, R., Ade, P. A. R., et al., 2015a, submitted to *A&A*, arXiv:1502.01582
- Planck Collaboration, Adam, R., Ade, P. A. R., et al., 2015b, accepted by *A&A*, arXiv:1502.01587
- Planck Collaboration, Ade, P. A. R., Aghanim, N., et al., 2011, *A&A*, 536, A1, arXiv:1101.2022
- Planck Collaboration, Ade, P. A. R., Aghanim, N., et al., 2014b, *A&A*, 571, A1, arXiv:1303.5062
- Planck Collaboration, Ade, P. A. R., Aghanim, N., et al., 2014c, *A&A*, 571, A1, arXiv:1303.5062
- Planck Collaboration, Ade, P. A. R., Aghanim, N., et al., 2014d, *A&A*, 571, A7, arXiv:1303.5068
- Planck Collaboration, Ade, P. A. R., Aghanim, N., et al., 2015c, accepted by *A&A*, arXiv:1506.07135
- Planck Collaboration, Ade, P. A. R., Aghanim, N., et al., 2015d, accepted by *A&A*, arXiv:1502.02114
- Planck Collaboration, Aghanim, N., Arnaud, M., et al., 2015e, submitted to *A&A*, arXiv:1507.02704

REFERENCES

- Planck HFI Core Team, Ade, P. A. R., Aghanim, N., et al., 2011, *A&A*, 536, A6, arXiv:1101.2048
- Ramamonjisoa, F. A., Ray, S., Mitra, S., Souradeep, T., 2013, ArXiv e-prints, arXiv:1309.4784
- Shimon, M., Keating, B., Ponthieu, N., Hivon, E., 2008, *Phys. Rev. D*, 77, 8, 083003, arXiv:0709.1513
- Souradeep, T., Mitra, S., Sengupta, A., Ray, S., Saha, R., 2006, *New Astronomy Reviews*, 50, 1030, astro-ph/0608505
- The Polarbear Collaboration: P. A. R. Ade, Akiba, Y., Anthony, A. E., et al., 2014, *ApJ*, 794, 171, arXiv:1403.2369
- Varshalovich, D., Moskalev, A., Khersonskii, V., 1988, *Quantum theory of angular momentum.*, World Scientific Publishing Co. Inc.
- Wallis, C. G. R., Brown, M. L., Battye, R. A., Pisano, G., Lamagna, L., 2014, *MNRAS*, 442, 1963, arXiv:1401.2075
- Wandelt, B. D., Górski, K. M., 2001, *Phys. Rev. D*, 63, 12, 123002, astro-ph/0008227
- Wu, J. H. P., Zuntz, J., Abroe, M. E., et al., 2007, *ApJ*, 665, 55, astro-ph/0611392